Focusing and Vertical Mode Scattering of the First Mode Internal Tide via Mesoscale Eddy Interactions

by

Michael Dunphy

A thesis
presented to the University of Waterloo
in fulfillment of the
thesis requirement for the degree of
Doctor of Philosophy
in
Applied Mathematics

Waterloo, Ontario, Canada, 2014

Author's Declaration

I hereby declare that I am the sole author of this thesis. This is a true copy of the thesis, including any required final revisions, as accepted by my examiners.

I understand that my thesis may be made electronically available to the public.

Abstract

In this work we perform numerical experiments using the MITgcm to simulate the interaction of a mode-one internal tide with barotropic and baroclinic mode-one mesoscale eddies. We also employ the ray tracing equations to track mode-one and mode-two internal tides through barotropic eddies.

Results show that barotropic eddies interact with a mode-one internal tide to produce beam-like regions of increased/decreased energy flux which we term hot/cold spots. The energy flux magnitude in the hot spots can reach twice that of the incident energy flux, while in the cold spots it can reach nearly zero.

The interaction between a mode-one internal tide and mode-one baroclinic eddies results in the production of internal tides at modes two and higher. The generated waves emanate from the eddy in beam-like patterns. A novel energy budget technique is developed to measure the generation rate at each mode, finding that the energy supplied to the higher modes is extracted from the incident mode-one wave, and that the eddy does not exchange net energy with the waves. For the parameter regime explored here, up to 13 percent of the incident energy is scattered to the higher modes for eddies of diameter 120 km.

The implication for the open ocean is an increase in vertical mixing local to mesoscale eddies, at the expense of reduced vertical mixing at remote coastlines. The vortex Rossby numbers are order one, corresponding to energetic mesoscale eddies found primarily in western boundary current extensions and in the southern ocean. We expect that these interactions will frequently form in locations where these phenomena coexist.

Ray tracing mode-one and two internal tides through barotropic eddies yielded four classes of ray paths, two of which are bounded by caustics. We use a wave field reconstruction technique to synthesise MITgcm outputs for a suite of eddies ranging from mesoscale to basin scale, demonstrating the improvement of the synthesis as eddy size increases. While the results are poor for low-mode waves interacting with a mesoscale eddy, the technique is viable for higher mode waves or larger scale eddies.

Acknowledgements

I would like to thank everyone who has helped make this work possible. First, many thanks are owed to Kevin Lamb for being an excellent supervisor and for his patience during this multi-year process. I'd like to thank Michael Waite and Francis Poulin for serving as my committee members, and also thank Marie-Pascale Lelong and Chris Fletcher for serving on my examining committee. Marek Stastna also deserves copious amounts of thanks for his guidance and advice despite not being part of my committee.

I'd also like to express appreciation for the support of my family. To my parents Paul and Heather, my brother Kevin, my sister Kathryn and her husband John: thank you.

Further thanks is extended to my friends and colleagues who have helped in many ways throughout my journey. I'd like to thank Aaron Coutino, Alex Shum, Amenda Chow, Andrew Beltaos, Anton Baglaenko, Antonio Sanchez, Ben Turnbull, Christopher Subich, Clinton Loo, Derek Steinmoeller, Dhanaraja Kasinathan, Jared Penney, Jason Olsthoorn, Killian Miller, Kris Rowe, Matthew Johnston, Nancy Soontiens, Robert Irwin, Sina Khani, Tim Rees, Wentao Liu, and Wilten Nicola.

Last but not least, I would like to thank my lovely wife Golnaz who has been at my side at all times. You are my partner in everything and deserve more thanks than it is possible to express here.

Dedication

This thesis is dedicated to my wonderful wife Golnaz.

Table of Contents

List of Tables

List of Figures

Nomenclature

α	Thermal expansion coefficient
α_0	Relaxation strength map input to the relaxation scheme
β	Haline contraction coefficient
Δt	Time step
δ	Ratio of peak eddy velocity to internal wave group velocity
ϵ	Ratio of wave packet wavelength to eddy length scale
ϵ_{nh}	Switch to enable/disable the hydrostatic approximation
∇	Gradient operator
∇^2	Laplacian operator
∇_h	Horizontal gradient operator
$\hat{\alpha}$	Relaxation strength map used during time stepping
$\hat{\phi}$	Latitude
$\hat{A}$	Wave action density of a wave packet
κ_Θ	Temperature diffusion coefficient
κ_n	Horizontal wavenumber
κ_S	Salt diffusion coefficient
$\frac{D}{Dt}$	Material derivative

μ	Coefficient of dynamic viscosity
Ω	Earth's rotation frequency
ω_0	M_2 tidal frequency
ω_r	Relative frequency
ϕ	Wave packet's central phase
$\Phi(z)$	Vertical structure of eddy
$\Phi_n(z)$	Vertical structure of an eddy with mode-n
$\phi_n(z)$	Vertical structure of internal tide mode-n
$\psi(r)$	Horizontal structure of eddy
$\Psi(r, z)$	Eddy streamfunction
ρ	Total Density
ρ'	Density perturbation ($= \rho_0 + \rho_1 + \rho'$)
$\rho(S, \Theta)$	Equation of state (linear)
$\rho(S, \Theta, p)$	Equation of state (general)
ρ_0	Constant reference density
ρ_1	Background stratification density profile
ρ_a	Density anomaly ($= \rho - \rho_0$)
τ_r	Timescale for relaxation scheme
Θ	Temperature
θ	Angle (0 is due east)
$\vec{\Omega}$	Earth's rotation vector
$\vec{c}_{g_0}$	Internal tide group velocity
$\vec{c}_g$	Total group velocity of a wave packet

$\vec{F}$	Forcing term in the momentum equation
$\vec{F}_h$	Forcing term in the horizontal momentum equation
$\vec{g}$	Gravitational acceleration vector
$\vec{k}$	Wave vector
$\vec{k}_h$	Horizontal wave vector
$\vec{M}_0$	Horizontal momentum equation for the barotropic mode
$\vec{M}_n$	Horizontal momentum equation for mode-n
$\vec{u}$	Velocity vector
$\vec{u}_h$	Horizontal velocity vector
A	Total available potential energy in volume V
A_f	Nonlinear flux of available potential energy leaving through the boundaries of volume V
A_n	Total baroclinic available potential energy at mode-n in area A
C	Available potential-kinetic energy conversion term in volume V
C_n	Available potential-kinetic energy conversion term at mode-n in area A
c_p	Internal tide phase speed
D_E	Eddy diameter
D_n	Continuity equation for mode-n
E	Energy density of a wave packet
F	Total sink of pseudo-energy in volume V $(= F_A + F_K)$
f	Coriolis parameter
F_ρ	Forcing term in the continuity equation
F_Θ	Forcing term in the temperature tracer equation

F_A	Energy sink due to forcing in the available potential energy budget
F_K	Energy sink due to forcing in the kinetic energy budget
F_S	Forcing term in the salinity tracer equation
F_u	Forcing term in the zonal momentum equation
F_v	Forcing term in the meridional momentum equation
F_w	Forcing term in the vertical momentum equation
F_{A_n}	Baroclinic available potential energy sink at mode-n due to forcing in area A
F_{K_0}	Barotropic kinetic energy sink due to forcing in area A
F_{K_n}	Baroclinic kinetic energy sink at mode-n due to forcing in area A
F_n	Total pseudo-energy sink due to forcing at mode-n in area A $(= F_{K_n} + F_{A_n})$
g	Gravitational acceleration constant
H	Model domain depth
K	Total kinetic energy in volume V
k	Zonal wavenumber
K_0	Total barotropic kinetic energy in area A
K_f	Nonlinear flux of kinetic energy leaving through the boundaries of volume V
K_n	Total baroclinic kinetic energy at mode-n in area A
l	Meridional wavenumber
L_E	Eddy length scale
L_x	Model domain length
L_y	Model domain width
m_n	Vertical wavenumber for internal tide mode-n
$N(z)$	Buoyancy frequency (vertical profile)

N_0	Buoyancy frequency (constant value)
N_0^u	Nonlinear term in the barotropic momentum equation
N_n^ρ	Nonlinear term in the n^{th} baroclinic continuity equation
N_n^u	Nonlinear term in the n^{th} baroclinic momentum equation
P	Total pseudo-energy in volume V $(= A + K)$
p	Total Pressure $(= p_0 + p_1 + p')$
p'	Pressure perturbation
p_0	Hydrostatic pressure associated with constant reference density
p_1	Hydrostatic pressure associated with background stratification
p_a	Pressure anomaly $(= p - p_0)$
P_n	Total pseudo-energy at mode-n in area A $(= A_n + K_n)$
Pe	Péclet number
$R(\tau)$	Ramp-up function for internal tide forcing
$R_{d,n}$	Baroclinic radius of deformation for mode-n
Re	Reynolds number
Ro	Vortex Rossby number
S	Salinity
S_0	Sink of barotropic kinetic energy in area A
S_n	Total pseudo-energy sink at mode-n in area A $(= S_n^u + S_n^\rho)$
S_n^ρ	Sink of baroclinic available potential energy at mode-n in area A
S_n^u	Sink of baroclinic kinetic energy at mode-n in area A
T	M_2 tidal period
T_0	Time when forcing is switched on

u	Zonal velocity
u_θ	Azimuthal velocity in polar coordinates
U_E	Eddy peak azimuthal velocity
U_t	Internal tide magnitude (u-component)
v	Meridional velocity
W	Work done at the boundaries of volume V
w	Vertical velocity
W_0	Barotropic work done at the boundaries of area A
W_n	Baroclinic work done at mode-n at the boundaries of area A

Chapter 1

Introduction

The world's oceans are richly populated with dynamical features with spatial and temporal scales spanning several decades. Among these are oceanic internal waves and these ubiquitous waves have received much attention in recent years as they have many roles in ocean dynamics. Contributions to oceanic vertical mixing (Polzin et al., 1997; Ledwell et al., 2000; Wunsch and Ferrari, 2004) are believed to be among the most important effects, but they also contribute to the upwelling of nutrients (Sharples et al., 2007; Schafstall et al., 2010) and to the transport of energy (Alford, 2003; Simmons and Alford, 2012). Shaping of the continental shelves has also been ascribed in part to internal waves (Cacchione et al., 2002; Puig et al., 2004; Klymak et al., 2011).

Internal tides (internal waves of tidal frequency) are an energetic subset of oceanic internal waves and the generation of internal tides has been studied by many authors. Understanding the fate of the internal tide once generated—where it propagates, with which oceanic features it interacts, and where it dissipates energy—is an active area of research. There has been an increasing awareness in recent years that the internal wave field is difficult to predict away from generation sites. Low-mode waves that leave generation sites propagate large distances, and are subject to various mesoscale currents and eddies which adjust propagation speeds and directions (Alford et al., 2012; Nash et al., 2012a,b; Kerry et al., 2013). Analysis of satellite altimetry data reveals that mode-one internal tides can propagate thousands of kilometers from their generation site (Zhao et al., 2012). A recent survey of ARGO profiler data by Whalen et al. (2012) found intensified mixing occurring in regions where mesoscale eddy kinetic energy is high, and proposed that internal waves interacting with these high energy eddies are responsible. Polzin (2010) revisited current meter data collected during the POLYMODE Local Dynamics Experiment in 1978–79 looking for evidence of internal wave-mesoscale interactions, and concluded that such

interactions play a first order role in the internal wave field's energy budget.

In this work we contribute to this understanding by investigating the effects that mesoscale eddies have on an internal tide field. We restrict attention to low mode internal tides of the M_2 frequency, and study the interaction with both isolated barotropic and baroclinic eddies. The tools used include a fully nonlinear numerical model to directly simulate the interaction and a novel modal energy budget technique that helps in interpreting the results. The numerical simulations and energy budgets are reported on in Dunphy and Lamb (2014). Lastly, under the Wentzel-Kramers-Brillouin-Jeffreys (WKBJ) approximation, we use the ray tracing equations to explain some of the model results.

By studying the impact of mesoscale eddies on the internal tide, we increase our understanding of how and where internal tide energy is dissipated and where vertical mixing is enhanced. Improved knowledge of the distribution of vertical mixing in the ocean is a key ingredient in improving ocean model forecasts, which in turn contribute to better atmosphere and climate predictions.

The thesis is organised in the following manner. Background material and previous work appears in Chapter 2 and the numerical methods are described in Chapter 3. In Chapter 4 we describe the methods used to analyse energy exchange between internal tide modes. Chapter 5 benchmarks the numerical methods, while Chapters 6 and 7 report on the interaction of a mode-one internal tide with barotropic and baroclinic eddies, respectively. Ray tracing is addressed in Chapter 8. Finally, conclusions and a discussion reside in Chapter 9.

Chapter 2

Background

This chapter discusses the background material relevant to the thesis. We first discuss the governing equations and the relevant approximations that lead to the Boussinesq equations. A section on both internal waves and mesoscale eddies follows. Lastly, we have a section summarising previous work relating to wave-eddy interactions.

2.1 Equations of Motion

We begin with the incompressible rotating Navier-Stokes equations, the incompressible continuity equation, temperature and salinity tracer equations and an equation of state, each in Cartesian coordinates:

$$\rho\frac{D\vec{u}}{Dt} + \rho 2\vec{\Omega}\times\vec{u} + \nabla p - \rho\vec{g} - \mu\nabla^2\vec{u} = \rho\vec{F}, \tag{2.1a}$$

$$\nabla\cdot\vec{u} = 0, \tag{2.1b}$$

$$\frac{D\Theta}{Dt} - \kappa_\Theta\nabla^2\Theta = F_\Theta, \tag{2.1c}$$

$$\frac{DS}{Dt} - \kappa_S\nabla^2 S = F_S, \tag{2.1d}$$

$$\rho = \rho(S,\Theta,p), \tag{2.1e}$$

where ρ is the density, $\frac{D}{Dt} = \frac{\partial}{\partial t} + \vec{u}\cdot\nabla$ is the material derivative, $\vec{u} = (u,v,w)$ is the velocity vector, $\vec{\Omega}$ is the angular velocity of the rotating frame, ∇ is the gradient operator, p is the pressure, $\vec{g} = (0,0,-g)$ is the gravitational attraction vector, μ is the dynamic

viscosity coefficient, ∇^2 is the Laplacian operator, $\vec{F} = (F_u, F_v, F_w)$ is the momentum forcing vector, Θ and S are the temperature and salinity, κ_Θ and κ_S are the temperature and salinity diffusivity coefficients, F_Θ and F_S are the temperature and salinity forcing terms, and $\rho(S, \Theta, p)$ is the equation of state.

These equations are a simplified form of the complete Navier-Stokes equations, however we make additional approximations and describe them in the following subsections. In this work, the forcing terms are zero except in relaxation regions (see Section 3.5).

2.1.1 Scales of Motion

The scales of interest are those of mesoscale eddies and the most energetic internal tides which happen to be the lowest modes. The horizontal eddy scales are order 50–200 km, and the low mode waves are order 25–100 km. Eddies evolve on the time scale of weeks to months, and internal tides on time scales of hours. A focus on these scales will help guide the approximation of the governing equations.

2.1.2 Inviscid Approximation

The Reynolds number,

$$Re = \frac{\rho U L}{\mu}, \tag{2.2}$$

is a measure of how important the inertial forces are as compared to the viscous forces. For water, $\mu \approx 1 \times 10^{-3}$ kg (ms)$^{-1}$ and $\rho \approx 1 \times 10^3$ kg m^{-3}. The smallest length scale here is $L \approx 1 \times 10^4$ m and smallest velocity scale $U \approx 1 \times 10^{-2}$ m/s. The corresponding Reynolds number is $\approx 10^8$, which means that the inertial forces dominate for these flows, so we neglect viscous effects by setting $\mu = 0$. This approximation breaks down in viscous boundary layers where velocity gradients may become large. However, for this thesis we do not resolve boundary layers and are not concerned with boundary layer effects.

2.1.3 Nondiffusive Approximation

The Péclet number,

$$Pe = \frac{UL}{\kappa}, \tag{2.3}$$

is a measure of the importance of the advective term as compared to the diffusive term. For water, the thermal diffusivity is $\kappa_\Theta \approx 1 \times 10^{-7}$ m s^{-2} and molecular diffusivity of salt is $\kappa_S \approx 1 \times 10^{-9}$ m s^{-2}. Using the same U and L scales as for the Reynolds number, we find Péclet numbers of $\approx 10^9$ and $\approx 10^{11}$ for heat and salt, and neglect the diffusion of each by setting $\kappa_\Theta = \kappa_S = 0$. Much like in the inviscid approximation, we can justify neglecting these diffusive terms everywhere except in areas where the temperature/salinity gradients become large.

2.1.4 Equation of State

Having neglected the diffusivity of temperature and salinity, we can combine (2.1c) and (2.1d) with an appropriate choice of (2.1e). We choose the linear equation of state,

$$\rho(S, \Theta) = \rho_0(1 - \alpha(\Theta - \Theta_0) + \beta(S - S_0)), \tag{2.4}$$

where $\rho_0 = 1028$ kg m^{-3}, $\Theta_0 = 10\,^o$C and $S_0 = 35$ psu are values for reference density, temperature, and salinity; and $\alpha = 1.7 \times 10^{-4}\,^o$C^{-1} is the thermal expansion coefficient and $\beta = 7.6 \times 10^{-4}$ psu^{-1} is the haline contraction coefficient. The combined equation reads

$$\frac{D\rho}{Dt} = F_\rho, \tag{2.5}$$

where F_ρ is the density forcing term, which reads

$$F_\rho = \rho_0(-\alpha F_\Theta + \beta F_S). \tag{2.6}$$

Nonzero density forcing arises via nonzero temperature or salinity forcing, occurring through addition or removal of heat or salt.

2.1.5 f-plane

The f-plane approximation is a simplification of the second term in the Navier-Stokes equations, $2\vec{\Omega} \times \vec{u}$, also known as the Coriolis term. On Earth, the angular velocity $\vec{\Omega}$ takes the form

$$\vec{\Omega} = (0, \cos\hat{\phi}, \sin\hat{\phi})\,\Omega \tag{2.7}$$

where $\hat{\phi}$ is the latitude and

$$\Omega = \frac{2\pi}{24 \times 60 \times 60\ \text{s}} \approx 0.727 \times 10^{-4}\,\text{rad}\,\text{s}^{-1}. \tag{2.8}$$

Substituting this into the Coriolis term reveals the three component vector,

$$2\vec{\Omega} \times \vec{u} = 2\Omega(w\cos\hat{\phi} - v\sin\hat{\phi}, u\sin\hat{\phi}, u\cos\hat{\phi}). \tag{2.9}$$

The f-plane approximation uses a constant latitude and amounts to two adjustments to the full Coriolis term. First, we assume $w \ll v$ and drop the $w\cos\hat{\phi}$ part from the first component. Next, we drop the third component $u\cos\hat{\phi}$ as it is very small when compared to the gravitational term $\vec{g}$ in the vertical momentum equation. These two adjustments are equivalent to dropping the second component of the angular velocity, leaving only

$$\vec{\Omega} = (0, 0, \sin\hat{\phi})\,\Omega, \tag{2.10}$$

which is the traditional component. By defining

$$f = 2\Omega\sin\hat{\phi} \tag{2.11}$$

as the Coriolis parameter and $\vec{f} = (0, 0, f)$, we can simplify the Coriolis term to

$$2\vec{\Omega} \times \vec{u} = (-fv, fu, 0) = \vec{f} \times \vec{u}. \tag{2.12}$$

2.1.6 Boussinesq Approximation

The Boussinesq approximation (Cushman-Roisin and Beckers, 2011) makes simplifications concerning the density anomaly. We write the total density as the sum of a constant reference density plus the space and time varying density anomaly,

$$\rho = \rho_0 + \rho_a(x, y, z, t). \tag{2.13}$$

When $\rho_a \ll \rho_0$, we neglect ρ_a in the Navier-Stokes equations everywhere except in the gravitational acceleration term (also known as the buoyancy term), yielding

$$\rho_0\frac{D\vec{u}}{Dt} + \rho_0\vec{f} \times \vec{u} + \nabla p - (\rho_0 + \rho_a)\vec{g} = \rho_0\vec{F}. \tag{2.14}$$

$$\tag{2.15}$$

The hydrostatic pressure is that associated with the weight of the fluid above it, or

$$p = g\int_z^0 \rho\,\mathrm{d}z, \tag{2.16}$$

and that associated with the constant reference density is

$$p_0(z) = g \int_z^0 \rho_0 \, \mathrm{d}z. \tag{2.17}$$

By writing the pressure as

$$p = p_0(z) + p_a(x, y, z, t), \tag{2.18}$$

we can remove it from (2.14), yielding

$$\rho_0 \frac{D\vec{u}}{Dt} + \rho_0 \vec{f} \times \vec{u} + \nabla p_a - \rho_a \vec{g} = \rho_0 \vec{F}. \tag{2.19}$$

$$\tag{2.20}$$

2.1.7 Hydrostatic Approximation

The hydrostatic approximation (Cushman-Roisin and Beckers, 2011) is a simplification of the vertical momentum equation,

$$\rho_0 \frac{Dw}{Dt} + \frac{\partial p_a}{\partial z} + \rho_a g = \rho_0 F_w, \tag{2.21}$$

where F_w is the vertical momentum forcing. A scaling analysis finds that when the aspect ratio of the flow is small ($H/L \ll 1$), the dominant balance involves the pressure gradient and buoyancy terms,

$$\frac{\partial p_a}{\partial z} \approx -\rho_a g, \tag{2.22}$$

amounting to dropping the material derivative and forcing terms.

2.1.8 Boussinesq Equations

Applying these approximations and dividing the momentum equations by ρ_0 leaves us with the inviscid incompressible Boussinesq equations, which read

$$\frac{D\vec{u}_h}{Dt} + f\hat{k} \times \vec{u}_h + \frac{1}{\rho_0}\nabla_h p_a = \vec{F}_h, \tag{2.23a}$$

$$\epsilon_{nh}\frac{Dw}{Dt} + \frac{g\rho_a}{\rho_0} + \frac{1}{\rho_0}\frac{\partial p_a}{\partial z} = \epsilon_{nh}F_w, \tag{2.23b}$$

$$\nabla_h \cdot \vec{u}_h + \frac{\partial w}{\partial z} = 0, \tag{2.23c}$$

$$\frac{D\rho_a}{Dt} = F_\rho, \tag{2.23d}$$

where $\vec{u_h} = (u, v)$ is the horizontal velocity vector, $\hat{k}$ is the unit vector pointing in the positive z direction, ∇_h is the horizontal gradient operator, $\vec{F_h} = (F_u, F_v)$ is the horizontal momentum forcing vector, and ϵ_{nh} is a switch, equal to 0 or 1, to control whether the hydrostatic approximation is active.

2.1.9 Perturbation Boussinesq Equations

We can further decompose the density anomaly into a background stratification part and a perturbation part (Gill, 1982),

$$\rho_a(x, y, z, t) = \rho_1(z) + \rho'(x, y, z, t). \tag{2.24}$$

We can find the hydrostatic pressure associated with the background stratification,

$$p_1(z) = g\int_z^0 \rho_1(z)\,\mathrm{d}z, \tag{2.25}$$

and subtract it from the vertical momentum equation. We also substitute (2.24) into the density equation, and make use of the buoyancy frequency

$$N^2(z) = -\frac{g}{\rho_0}\frac{\mathrm{d}\rho_1(z)}{\mathrm{d}z}, \tag{2.26}$$

which yields the perturbation Boussinesq equations

$$\frac{D\vec{u}_h}{Dt} + f\hat{k} \times \vec{u}_h + \frac{1}{\rho_0}\nabla_h p' = \vec{F}_h, \tag{2.27a}$$

$$\epsilon_{nh}\frac{Dw}{Dt} + \frac{g\rho'}{\rho_0} + \frac{1}{\rho_0}\frac{\partial p'}{\partial z} = \epsilon_{nh}F_w, \tag{2.27b}$$

$$\nabla_h \cdot \vec{u}_h + \frac{\partial w}{\partial z} = 0, \tag{2.27c}$$

$$\frac{D\rho'}{Dt} - \frac{\rho_0 N^2(z)}{g}w = F_\rho. \tag{2.27d}$$

2.2 Internal Gravity Waves

Gravity waves are waves that require both gravity and inertia. A well known example of a gravity wave is the surface wave found at air-water boundaries such as the surface of lakes and oceans. Internal gravity waves are a subclass of gravity waves found in stratified fluids. The ocean and atmosphere are such fluids and are well known to contain internal waves of various forms. For example, lee waves are a form of internal gravity wave formed primarily by steady flow over topography such as mountains or submarine topography, and solitary waves are a class of nonlinear internal gravity waves that maintain their shape as they propagate. Internal gravity waves may also be oscillatory with a characteristic frequency. In the ocean, when the characteristic frequency is a tidal frequency then they are often called internal tides, and are the internal gravity waves of interest in this work. This section will briefly discuss the generation of the oceanic internal tide, summarise linear, vertically trapped internal tide solutions, and present the ray tracing equations for tracing internal tides through a barotropic background flow.

2.2.1 Generation

A variety of mechanisms are responsible for generating internal gravity waves, among which are surface forcing, flow-topography interactions, and numerous types of instability. However, the primary generation mechanism for internal tides is tidal flow interacting with submarine topography. As a barotropic (surface) tide oscillates across topography, it sheds energy to baroclinic (internal) tide modes which then propagate away. Globally, an estimated 2.5 TW of power is input to the barotropic mode at the principle lunar tide M_2 (3.7 TW across all constituents), and 25–30% of that barotropic tidal power is converted to

internal tide modes (Egbert and Ray, 2001). The Hawaiian ridge is a well known example that converts 15 GW from the barotropic tide and injects it into the first mode internal tide (Ray, 1997). The review article by Garrett and Kunze (2007) discusses more details of the theoretical and numerical work concerning the generation processes.

Once generated, the internal tide interacts with numerous oceanic features, such as eddies, currents, and other waves. Many of these interactions will transfer energy between spatial and temporal scales via the quadratic nonlinearity in the advective term of the governing equations. Consequently, the ocean is a "noisy" place filled with waves of a variety of frequencies and wavenumbers, and attempts have been made to describe a universal oceanic internal wave spectrum from observations. A well known example is the Garrett-Munk spectrum (Garrett and Munk, 1979) but other work indicates that the spectrum is not universal, and deviates spatially and temporally.

2.2.2 Linearised Equations

Internal wave solutions may be found through the linearised governing equations (Cushman-Roisin and Beckers, 2011). We linearise the perturbation equations (2.27) by dropping the forcing and quadratic terms in the material derivative. The remaining terms form governing equations for small amplitude signals, and read

$$\frac{\partial u}{\partial t} - fv = -\frac{1}{\rho_0}\frac{\partial p'}{\partial x}, \tag{2.28a}$$

$$\frac{\partial v}{\partial t} + fu = -\frac{1}{\rho_0}\frac{\partial p'}{\partial y}, \tag{2.28b}$$

$$\epsilon_{nh}\frac{\partial w}{\partial t} = -\frac{1}{\rho_0}\frac{\partial p'}{\partial z} - \frac{g}{\rho_0}\rho', \tag{2.28c}$$

$$\frac{\partial u}{\partial x} + \frac{\partial v}{\partial y} + \frac{\partial w}{\partial z} = 0, \tag{2.28d}$$

$$\frac{\partial \rho'}{\partial t} - \frac{\rho_0 N^2(z)}{g}w = 0. \tag{2.28e}$$

Combining these equations yields a wave equation for the vertical velocity,

$$\frac{\partial^2}{\partial t^2}\left(\epsilon_{nh}\left(\frac{\partial^2}{\partial x^2} + \frac{\partial^2}{\partial y^2}\right) + \frac{\partial^2}{\partial z^2}\right)w + N^2(z)\left(\frac{\partial^2}{\partial x^2} + \frac{\partial^2}{\partial y^2}\right)w + f^2\frac{\partial^2}{\partial z^2}w = 0. \tag{2.29}$$

2.2.3 Vertically Trapped Solutions

We consider here a horizontally unbounded ocean of constant depth with a rigid lid, within which internal waves will be vertically trapped and can only propagate horizontally. Thus we substitute the horizontal plane wave ansatz with a general vertical structure

$$w = \phi_n(z)e^{i(kx+ly-\omega t)}, \tag{2.30}$$

into the wave equation (2.29) and obtain a Sturm-Liouville problem,

$$\frac{\mathrm{d}\phi_n(z)}{\mathrm{d}z^2} + \kappa_n^2 \left(\frac{N^2(z) - \epsilon_{nh}\omega^2}{\omega^2 - f^2} \right) \phi_n(z) = 0, \tag{2.31}$$

subject to the no-normal flow boundary conditions at the top and bottom

$$\phi_n(0) = \phi_n(-H) = 0,$$

where $\kappa_n = \sqrt{k^2 + l^2}$ is the horizontal wavenumber, $\phi_n(z)$ is the vertical structure function, H is the water depth, $N(z)$ is the buoyancy frequency, ω is the frequency and f is the Coriolis parameter. In general finding solutions requires a numerical method (Dunphy (2009) shows one such approach) but with a constant buoyancy frequency $N(z) = N_0$, analytic solutions are available and have the form

$$\phi_n = \sin(m_n z), \tag{2.32}$$

where

$$m_n = \frac{n\pi}{H}, \tag{2.33}$$

and

$$\kappa_n = m_n \left(\frac{\omega^2 - f^2}{N_0^2 - \epsilon_{nh}\omega^2} \right)^{1/2}. \tag{2.34}$$

We assume here that the wave frequency ω is a fixed parameter such that the eigenvalue is the horizontal wavenumber κ_n and the eigenfunction $\phi_n(z)$ is the associated vertical structure. It is possible to take κ_n as the parameter and ω as the eigenvalue, although we

do not do it here. Substituting the vertical structure function (2.32) into (2.31) yields the dispersion relation for the vertically trapped waves

$$\omega^2 = \frac{N_0^2\kappa_n^2 + f^2 m_n^2}{\epsilon_{nh}\kappa_n^2 + m_n^2}. \tag{2.35}$$

The frequency divided by the horizontal wavenumber yields the phase speed,

$$c_p = \frac{\omega}{\kappa_n} = \frac{1}{\kappa_n}\sqrt{\frac{N_0^2\kappa_n^2 + f^2 m_n^2}{\epsilon_{nh}\kappa_n^2 + m_n^2}}, \tag{2.36}$$

and the wavenumber gradient of the frequency gives the group velocity,

$$\vec{c}_{g_0} = \nabla_{\vec{k}}\,\omega = \frac{m_n^2(N_0^2 - \epsilon_{nh}f^2)}{\omega(\epsilon_{nh}\kappa_n^2 + m_n^2)^2}(k, l), \tag{2.37}$$

which simplifies under the hydrostatic approximation to

$$\vec{c}_{g_0} = \frac{N_0^2}{\omega m_n^2}(k, l).$$

Polarisation Relations

We take the real part of (2.30) with amplitude w_0 as the vertical velocity

$$w = w_0 \sin(m_n z)\cos(kx + ly - \omega t), \tag{2.38a}$$

and substitute it into the linearised equations (2.28), to obtain the polarisation relations

$$u = w_0\left(-\frac{m_n}{\kappa_n^2\omega}\right)\cos(m_n z)\Big(k\omega\sin(kx + ly - \omega t) + lf\cos(kx + ly - \omega t)\Big), \tag{2.38b}$$

$$v = w_0\left(-\frac{m_n}{\kappa_n^2\omega}\right)\cos(m_n z)\Big(l\omega\sin(kx + ly - \omega t) - kf\cos(kx + ly - \omega t)\Big), \tag{2.38c}$$

$$p' = w_0\left(-\frac{\rho_0(N_0^2 - \epsilon_{nh}\omega^2)}{\omega m_n}\right)\cos(m_n z)\sin(kx + ly - \omega t), \tag{2.38d}$$

$$\rho' = w_0\left(-\frac{\rho_0 N_0^2}{\omega g}\right)\sin(m_n z)\sin(kx + ly - \omega t). \tag{2.38e}$$

The vertically integrated kinetic energy density, averaged over one horizontal wavelength, is

$$\overline{KE} = \frac{\rho_0 w_0^2 H}{8} \frac{m_n^2}{\kappa_n^2} \left(1 + \frac{f^2}{\omega^2} + \epsilon_{nh} \frac{\kappa_n^2}{m_n^2}\right), \tag{2.39}$$

and the corresponding available potential energy density is

$$\overline{APE} = \frac{\rho_0 w_0^2 H}{8} \frac{N_0^2}{\omega^2}, \tag{2.40}$$

which sum to give the pseudo-energy density

$$\overline{E} = \overline{KE} + \overline{APE}. \tag{2.41}$$

2.2.4 Ray Tracing

Rays are the paths followed by wave packets and the ray tracing technique relies on the WKBJ approximation. The approximation states that the wavelength of the wave packet is short compared to the length scales over which the background flow varies. The parameter ϵ is the ratio of the wave packet's wavelength to the background flow lengthscale and we require $\epsilon \ll 1$ for the ray tracing method to be valid. This subsection summarises the ray tracing equations by following Chavanne et al. (2010) while simplifying for vertically trapped internal waves propagating through a barotropic background flow.

Background State

The background flow field is barotropic, steady, divergence free, and varies only in the horizontal, taking the form $\vec{U}_h(x, y) = (U(x, y), V(x, y))$. A surface pressure gradient drives the barotropic flow, so the corresponding background density is horizontally uniform with a constant buoyancy frequency N_0.

Governing Equations

We use the perturbation Boussinesq equations (2.27) with the hydrostatic approximation applied via $\epsilon_{nh} = 0$. We drop the forcing terms and substitute the horizontal velocity

$$\vec{u}_h = \vec{U}_h + \vec{u}'_h. \tag{2.42}$$

The equations are linearised by dropping terms quadratic in the perturbation quantities, and gradients of the background flow $\vec{U}_h$ are also neglected, reflecting the slowly varying nature of the background field. The resulting set of governing equations is

$$\frac{\partial u'}{\partial t} + U\frac{\partial u'}{\partial x} + V\frac{\partial u'}{\partial y} - fv' = -\frac{1}{\rho_0}\frac{\partial p'}{\partial x}, \tag{2.43a}$$

$$\frac{\partial v'}{\partial t} + U\frac{\partial v'}{\partial x} + V\frac{\partial v'}{\partial y} + fu' = -\frac{1}{\rho_0}\frac{\partial p'}{\partial y}, \tag{2.43b}$$

$$0 = -\frac{1}{\rho_0}\frac{\partial p'}{\partial z} - \frac{g}{\rho_0}\rho', \tag{2.43c}$$

$$\frac{\partial u'}{\partial x} + \frac{\partial v'}{\partial y} + \frac{\partial w'}{\partial z} = 0, \tag{2.43d}$$

$$\frac{\partial \rho'}{\partial t} - \frac{\rho_0 N_0^2}{g}w' = 0. \tag{2.43e}$$

Next, we substitute a local plane wave ansatz

$$(u', v', w', p', \rho') = (u'_0, v'_0, w'_0, p'_0, \rho'_0)e^{i(\vec{k}\cdot\vec{x}-\omega t)}, \tag{2.44}$$

where the amplitudes vary on slow scales and $\vec{k} = (k, l, m_n)$, and with some algebra (not shown here), find the local dispersion relation which takes the form

$$\omega = \omega_r + \vec{k}_h \cdot \vec{U}_h, \tag{2.45}$$

where $\vec{k}_h = (k, l)$. The constant absolute frequency ω is that measured by a stationary observer. In a reference frame moving with the local background velocity, the relative frequency ω_r satisfies the dispersion relation (2.35). The local dispersion relation (2.45) is viewed as a Doppler shift equation that relates the absolute and relative frequencies.

Wave packets propagate with the local group velocity

$$\frac{\mathrm{d}\vec{x}}{\mathrm{d}t} = \vec{c}_g = \nabla_{\vec{k}}\,\omega = \vec{c}_{g_0} + \vec{U}_h, \tag{2.46a}$$

where $\frac{\mathrm{d}}{\mathrm{d}t} = \frac{\partial}{\partial t} + \vec{c}_g \cdot \nabla$ and $\vec{c}_{g_0}$ is the group velocity in the moving reference frame (that is, relative to the fluid). The wavenumber of the packet evolves by

$$\frac{\mathrm{d}\vec{k}}{\mathrm{d}t} = -\frac{\partial \omega}{\partial \vec{x}} = -k\frac{\partial U}{\partial \vec{x}} - l\frac{\partial V}{\partial \vec{x}}. \tag{2.46b}$$

Given an initial position $\vec{x}$ and wavevector $\vec{k}_h$, solving the differential equations (2.46) will determine the trajectory and wavenumber of a wave packet as it propagates through a barotropic flow.

Energetics

We estimate the wave packet energy using the conservation of wave action,

$$\frac{\mathrm{d}\hat{A}}{\mathrm{d}t} + \hat{A}\nabla \cdot \vec{c}_g = \frac{\partial \hat{A}}{\partial t} + \nabla \cdot (\vec{c}_g \hat{A}) = 0, \tag{2.47}$$

where $\hat{A} = E/\omega_r$ is the wave action density. An equivalent statement is the energy budget

$$\frac{\mathrm{d}E}{\mathrm{d}t} = -E\nabla \cdot \vec{c}_g + \frac{E}{\omega_r}\frac{\mathrm{d}\omega_r}{\mathrm{d}t} \tag{2.48}$$

that governs the energy of the wave packet as it moves through the nonuniform background flow. The first term on the right arises from the convergence or divergence of rays. If $\nabla \cdot \vec{c}_g$ is positive, energy decreases due to ray divergence, and conversely increases due to ray convergence when $\nabla \cdot \vec{c}_g$ is negative. The second term accounts for energy exchange between the wave and the background flow. Waves gain energy (at the expense of the background flow) when they propagate into regions of increasing ω_r, and lose energy to the background flow when propagating through decreasing ω_r. Equation (2.45) shows that ω_r is larger where waves propagate against the background current and smaller when propagating with the current.

Caustics

Caustics are regions where adjacent ray paths intersect and the wave amplitude rapidly increases toward infinity. The WKBJ assumption of slowly varying wave properties is broken in such regions and the ray tracing predictions deemed of poor quality. In general, the formation of caustics depends on the formulation of the ray model, and dealing with them is nontrivial. A buoyancy frequency turning point is a classic example of a caustic where rays reverse their vertical direction of propagation, and Lighthill (1978) uses an Airy function to "heal" it. The review article by Broutman et al. (2004) looks at ray methods and caustics in more detail.

2.3 Mesoscale Eddies

Eddies are persistent rotating coherent vortices found in the ocean and their lifetime greatly exceeds their rotational period (Cushman-Roisin and Beckers, 2011). Mesoscale eddies have

length scales of order 100 km and are approximately axisymmetric. The gradient wind balance (or cyclo-geostrophic balance) equation describes the eddy in polar coordinates,

$$\frac{u_\theta^2}{r} + f u_\theta = \frac{1}{\rho_0}\frac{\partial p'}{\partial r}, \tag{2.49}$$

where, from left to right, we have the centrifugal term, Coriolis term and pressure term. The quantity u_θ is the azimuthal velocity (counterclockwise positive), f is the Coriolis parameter, p' is the pressure perturbation and ρ_0 is a constant reference density. If we scale u_θ by the peak azimuthal velocity $U_{\max}$ and r by the radius of peak velocity $r_{\max}$, and divide the centrifugal term by the Coriolis term, we get the vortex Rossby number

$$R_o = \frac{U_{\max}}{f r_{\max}}. \tag{2.50}$$

The vortex Rossby number provides a simple way to classify eddies. When the dominant balance is between the last two terms ($R_0 \ll 1$) the eddy is in geostrophic balance and designated a geostrophic eddy. Similarly, a cyclostrophic eddy ($R_o \gg 1$) balances the first and last terms, and a cyclo-geostrophic eddy ($R_o \approx 1$) draws a balance between all three terms.

Mesoscale eddies may be further classified as cyclones or anticyclones. Cyclones rotate in the same direction as the ambient rotation, which is counterclockwise at positive latitude and clockwise at negative latitude. Anticyclones, conversely, rotate in the opposite direction as the ambient rotation; clockwise (counterclockwise) north (south) of the equator (Cushman-Roisin and Beckers, 2011).

2.3.1 Vertical Structure

Use of the quasi-geostrophic equations of motion provides insight on the vertical structure of eddies. Carton (2001) showed that the vertical structure $\Phi(z)$ of the horizontal velocities is composed of solutions to the Sturm-Liouville problem

$$\frac{\mathrm{d}}{\mathrm{d}z}\frac{f^2}{N^2(z)}\frac{\mathrm{d}\Phi_n}{\mathrm{d}z} + \frac{1}{R_{d,n}^2}\Phi_n = 0, \tag{2.51}$$

subject to the boundary conditions

$$\frac{\mathrm{d}\Phi_n(0)}{\mathrm{d}z} = \frac{\mathrm{d}\Phi_n(-H)}{\mathrm{d}z} = 0,$$

where the $R_{d,n}$ is the n^{th} baroclinic radius of deformation. A numerical method is needed for general $N(z)$ (Dunphy (2009) shows one approach), but for a linear stratification where $N(z) = N_0$ we can find analytic solutions of the form

$$\Phi_n = \cos(m_n z), \tag{2.52}$$

where

$$m_n = \frac{n\pi}{H}, \tag{2.53}$$

and

$$R_{d,n} = \frac{f}{N_0} m_n. \tag{2.54}$$

2.3.2 Generation Mechanism

Well known mesoscale eddy generation mechanisms include barotropic and baroclinic instability of jets. Barotropic instability extracts energy from a horizontally sheared flow, while baroclinic instability is powered by a release of potential energy. Both instabilities feed the extracted energy into unstable perturbations which grow into meanders. Initial perturbations to an unstable jet (which may contain both barotropic and baroclinic components) grow into meanders and may eventually undergo occlusion, yielding an eddy (Cushman-Roisin and Beckers, 2011).

Western boundary currents such as the Kuroshio or the Gulf Stream/North Atlantic Current system are well known generation sites for energetic mesoscale eddies. Such eddies are called "rings" and are produced in warm core and cold core variants. Warm core rings are anticyclones and are found poleward of the western boundary current, where they encircle warm water. Conversely, cold core rings are cyclones, found equatorward of the current, and encircle cold water (Olson, 1991). As these eddies propagate they bring their core of anomalously warm or cold water, making them an effective means of transporting water mass properties large distances across the ocean.

Flow past an oceanic obstacle such as a deep island can generate lee eddies, similar to how flow past an obstacle produces a von Kármán vortex street. Variations in atmospheric wind shear can also lead to eddy production (Jia et al., 2011).

2.3.3 Observations

Eddies in the open ocean often have an associated sea-surface height signature. Chelton et al. (2011) conducted an extensive survey of sixteen years worth of sea-surface height data collected from satellite altimeters in an effort to characterise the ocean's eddy field. They found that 90 percent of the observed eddies had length scales falling in the 50–150 km band, which compares well with the Rossby radius of deformation away from the tropics. In terms of longevity, roughly 75 percent of the eddies had a lifetime exceeding 16 weeks. The vortex Rossby number in equation (2.50) was below 0.1 for most of the eddies, indicating that eddies are primarily geostrophically balanced. Most of the surveyed eddies propagate nearly due west and have an advective nonlinearity parameter $U/c > 1$, indicating that they efficiently transport trapped cores of water as they propagate.

Satellite altimeter data is not useful to detect eddies without a sea-surface height signature or eddies trapped below ice cover. However, hydrographic sections collected from surface vessels may reveal subsurface eddies, a well known example of which are "meddies" (Mediterranean eddies). Meddies form when warm salty water overflows from the Strait of Gibraltar, descends to a depth of 500–1500 m, and eventually separates to produce anticyclonic lenses with diameters ranging from 40 to 100 km. Azimuthal velocities reach 30 cm/s, and the meddies transport their warm salty water westward across the North Atlantic until they either spin down or collide with seamounts (Richardson, 2000).

Eddies trapped below ice cover may be observed from hydrographic sections collected via submarines. An example is the Canada Basin eddy observed by Muench et al. (2000) which had velocities exceeding 20 cm/s and a diameter of 20 km. Ice tethered profilers are also used to observe eddies in the Canada Basin, and Timmermans et al. (2008) reported on observations of numerous eddies with horizontal scales at or below 10 km and velocities spanning 9 to 26 cm/s.

Wunsch (1997) examined current meter data and concluded that the barotropic and first baroclinic mode dominate the vertical structure of mesoscale eddies. Zhang et al. (2013) surveyed ARGO float and satellite altimeter data in search of a universal structure of mesoscale eddies. They presented evidence indicating that the horizontal structure of the pressure roughly follows

$$\psi(r) = \left[1 - \frac{1}{2}\left(\frac{r}{L_E}\right)^2\right] e^{-\frac{1}{2}\left(\frac{r}{L_E}\right)^2} \tag{2.55}$$

where L_E is an eddy length scale. They further found that the pressure's vertical structure is well explained by a fit to the barotropic mode plus the first baroclinic mode, consistent with Wunsch (1997).

2.4 Previous Work

The interaction between internal tides and mesoscale eddies has been looked at by a few other authors. This section summarises the work that is closely related to this thesis.

2.4.1 Barotropic Tide

Recent work by Lelong and Kunze (2013) looked at interactions between the barotropic tide and mesoscale eddies as a potential generation mechanism for internal tides. They found that a horizontally uniform barotropic tide produced no interaction, and that optimal interaction occurs when the eddy lengthscale is comparable to the horizontal lengthscale of the barotropic tide. In the ocean, this compatibility is seldom found, and the authors concluded that the large difference in length scales between the two phenomena precluded their interaction from efficiently producing internal tides.

2.4.2 Wave Capture

Bühler and McIntyre (2005) discuss a wave capture mechanism where internal wave packets extract energy from a shear flow as they propagate through. The wavelength of the packet decreases and its energy increases, leading to deformation and eventual breaking. Ferrari and Wunsch (2009) noted that this mechanism may work as an eddy viscosity acting on the large scale shear flow, and thus help close the ocean's eddy kinetic energy budget.

2.4.3 Resonant Triads

Under the assumption of a constant buoyancy fluid, Lelong and Riley (1991) showed that resonant triad interactions (McComas and Bretherton, 1977) can be found between a vortical mode and two internal wave modes. The interaction is interesting because the vortex does not exchange energy with the wave modes, rather the wave modes exchange energy with each other and the vortex acts simply as a catalyst. The vortical mode has zero frequency, $\omega_2 = 0$, and thus the two wave modes will have the same frequency as a consequence of the resonant frequency condition

$$\omega_1 \pm \omega_2 \pm \omega_3 = 0. \tag{2.56}$$

A side effect of matching frequencies is that the wave vector of both internal wave modes are found on a constant frequency cone in wavenumber space. The wavenumbers of each satisfy the resonant wavenumber condition

$$\vec{k}_1 \pm \vec{k}_2 \pm \vec{k}_3 = 0. \tag{2.57}$$

The wave and vortical modes considered here are periodic and Riley et al. (1991) demonstrated the energy exchange numerically using a periodic domain. Lelong and Riley (1991) did not consider rotational effects, but Bartello (1995) found that the same wave-wave-vortex triads form on an f-plane. Both of these authors have described wave-wave-vortex triads as easy to form.

Ward and Dewar (2010) used a shallow water model to investigate the scattering of gravity modes by a periodic potential vorticity field, finding that the gravity waves were scattered into modes with similar wavelengths but a wide array of propagation directions.

2.4.4 Ray Tracing

Ray tracing has been used by a number of authors in the context of internal waves and mesoscale currents. Kunze (1985) traced near-inertial wave packets through a geostrophic shear, and found that waves were trapped in regions of negative vorticity, reflected from critical layers in the horizontal, and stalled at critical layers in the vertical.

Rainville and Pinkel (2006) used a two dimensional ray tracing formulation to track low mode internal tides as they propagate from a generation site through a barotropic mesoscale current field. Results showed that the propagation path of mode-one waves is only mildly affected by the mesoscale currents and that the phase becomes random as the distance propagated increases. Modes three and higher suffered a dramatic loss in coherence resulting from their passing through the currents.

Three dimensional ray tracing of internal tides was used by Chavanne et al. (2010) to study their propagation away from the Hawaiian Ridge and through two idealised mesoscale currents. Propagation through a mesoscale cyclone intensified surface internal wave energy, and propagation through a vortex Rossby wave yielded surface wave energy that increased or decreased depending on their phase.

Hertzog et al. (2002) derived a transport equation for phase-space wave-action density for gravity waves. Muraschko et al. (2014) used the transport equation in one dimension in the context of vertically propagating atmospheric gravity waves, and included comparisons with results from weakly and fully nonlinear numerical models.

2.4.5 Interference Pattern Reconstruction

Rainville et al. (2010) constructed line sources that approximate the generation of the M_2 internal tide at modes one and two at the Hawaiian Ridge. Four line sources were analytically prescribed which describe internal tide beams that radially spread as they propagate away from the ridge on the south side. The superposition of the beams yields an interference pattern that agreed reasonably well with a fully nonlinear high-resolution numerical model.

Zhao et al. (2010) decomposed sea-surface height anomaly data collected north of French Frigate Shoals near Hawaii into northward and southward propagating mode-one M_2 components. A plane wave is constructed for each, and their superposition yielded an interference pattern that resembles the observed sea-surface height anomaly.

Chapter 3

MITgcm

This work looks at the interaction between the internal tide and mesoscale features, particularly mesoscale eddies. We use a numerical model to simulate the interaction of these features and examine the model output to draw conclusions.

The chosen model is the MIT General Circulation Model or MITgcm (Marshall et al., 1997), a finite volume model designed for simulating both the atmosphere and the ocean. When used for the atmosphere it uses pressure coordinates while it uses z-coordinates for the ocean. In this section we discuss the MITgcm configuration, leaving the experiment specifics for later.

3.1 Governing Equations

The equations of motion that MITgcm solves for the ocean are,

$$\frac{D\vec{u}_h}{Dt} + f\hat{k} \times \vec{u}_h + \frac{1}{\rho_0}\nabla_h p_a = \vec{F}_h, \tag{3.1a}$$

$$\epsilon_{nh}\frac{Dw}{Dt} + \frac{g\rho_a}{\rho_0} + \frac{1}{\rho_0}\frac{\partial p_a}{\partial z} = \epsilon_{nh}F_w, \tag{3.1b}$$

$$\nabla_h \cdot \vec{u}_h + \frac{\partial w}{\partial z} = 0, \tag{3.1c}$$

$$\rho_a = \rho(\Theta, S, p_0(z)) - \rho_0, \tag{3.1d}$$

$$\frac{DS}{Dt} = F_S, \tag{3.1e}$$

$$\frac{D\Theta}{Dt} = F_\Theta, \tag{3.1f}$$

where $\vec{u}_h$ is the horizontal velocity vector, w is the vertical velocity, ρ_0 is a constant reference density, ρ_a is the density anomaly, $p_0(z)$ is the hydrostatic pressure profile associated with ρ_0, p_a is the pressure perturbation, f is the Coriolis parameter, g is the gravitational acceleration constant, $\hat{k}$ is the vertical unit vector, ∇_h is the horizontal gradient operator, $\vec{F}_h$ is the horizontal momentum forcing term, F_w is the vertical momentum forcing term, ϵ_{nh} is a non hydrostatic switch, S is the salinity, F_S is the salinity forcing, Θ is the potential temperature, and F_Θ is the temperature forcing. The forcing terms here include contributions from viscosity and diffusivity.

In this work we hold temperature constant, salt is the active tracer, and the equation of state is linear. Viscosity and diffusivity are neglected, eliminating parts of the forcing terms. The governing equations simplify to

$$\frac{D\vec{u}_h}{Dt} + f\hat{k} \times \vec{u}_h + \frac{1}{\rho_0}\nabla_h p_a = \vec{F}_h, \tag{3.2a}$$

$$\epsilon_{nh}\frac{Dw}{Dt} + \frac{g\rho_a}{\rho_0} + \frac{1}{\rho_0}\frac{\partial p_a}{\partial z} = \epsilon_{nh}F_w, \tag{3.2b}$$

$$\nabla_h \cdot \vec{u}_h + \frac{\partial w}{\partial z} = 0. \tag{3.2c}$$

$$\frac{D\rho_a}{Dt} = F_\rho, \tag{3.2d}$$

With these adjustments, the equations solved by MITgcm are consistent with the incompressible Boussinesq equations (2.23). All simulations use the hydrostatic approximation,

which sets $\epsilon_{nh} = 0$. We use the centred second order advection scheme for both momentum and salinity.

3.2 Model Domain

The model uses a rectangular domain of dimensions $L_x \times L_y$ on a f-plane, with a rigid lid, constant buoyancy frequency N_0, and constant depth H. The north-south boundaries are periodic, the east closed, and the west forced.

3.3 Mesoscale Eddy Prescription

The internal tide-eddy interaction experiments use an isolated mesoscale eddy as the initial condition, which we describe by the streamfunction

$$\Psi(r,z) = \psi_h(r)\Phi(z) = -\frac{5^{\frac{5}{2}}}{64} U_E L_E \operatorname{sech}^4\left(\frac{r}{L_E}\right)\Phi(z). \tag{3.3}$$

The location of the eddy centre is (x_c, y_c) and with $r^2 = (x-x_c)^2 + (y-y_c)^2$, $\psi(r)$ and $\Phi(z)$ describe the horizontal and vertical structure. The constant scaling factor of $-5^{5/2}/64$ ensures that ψ_r yields a peak azimuthal velocity of $U_{\max} = U_E$ at $r = r_{\max} = L_E \tanh^{-1}(\sqrt{5}/5) \approx 0.48 L_E$. The eddy's vortex Rossby number (2.50) uses these values of $U_{\max}$ and $r_{\max}$. The parameter L_E is the length scale of the eddy, and the peak velocity drops to below 2 percent at a radial distance of $2L_E$, corresponding to an eddy diameter $D_E = 4L_E$. The eddy's azimuthal velocity is

$$u_\theta = \frac{\partial \Psi}{\partial r} = -\frac{5^{\frac{5}{2}}}{16} U_E \operatorname{sech}^4\left(\frac{r}{L_E}\right)\tanh\left(\frac{r}{L_E}\right)\Phi(z), \tag{3.4}$$

which converts to Cartesian form for model initialisation by

$$(U, V) = (-\sin\theta, \cos\theta)\, u_\theta, \tag{3.5}$$

where

$$\theta = \tan^{-1}\left(\frac{y-y_c}{x-x_c}\right). \tag{3.6}$$

To find a balanced density field we start with the cyclo-geostrophic balance in cylindrical coordinates

$$\frac{u_\theta^2}{r} + f u_\theta = \frac{1}{\rho_0}\frac{\partial p'}{\partial r}, \tag{3.7}$$

take a derivative in the vertical,

$$\frac{2}{r}\frac{\partial u_\theta}{\partial z}u_\theta + f\frac{\partial u_\theta}{\partial z} = \frac{1}{\rho_0}\frac{\partial^2 p'}{\partial r \partial z}, \tag{3.8}$$

multiply by ρ_0 and integrate radially,

$$\rho_0 \int \left(\frac{2}{r}\frac{\partial u_\theta}{\partial z}u_\theta + f\frac{\partial u_\theta}{\partial z}\right) \mathrm{d}r = \frac{\partial p'}{\partial z}. \tag{3.9}$$

Lastly, we substitute the hydrostatic balance

$$-g\rho' = \frac{\partial p'}{\partial z} \tag{3.10}$$

and divide by $-g$ which gives the desired density field

$$\rho' = \frac{-\rho_0}{g} \int \left(\frac{2}{r}\frac{\partial u_\theta}{\partial z}u_\theta + f\frac{\partial u_\theta}{\partial z}\right) \mathrm{d}r. \tag{3.11}$$

The integral is evaluated numerically due to the r^{-1} found in the integrand and the farfield condition $\rho'(r = \infty) = 0$ resolves the constant of integration. A quick inspection reveals that the density perturbation is zero when the azimuthal velocity is depth-independent (barotropic).

We study two types of eddies, the first being a cyclonic barotropic eddy where $\Phi(z) = 1$, and the second a mode-one baroclinic eddy where $\Phi(z) = \cos(\pi z/H)$. The baroclinic eddy is cyclonic at the ocean surface but anticyclonic at the ocean floor. Figure 3.1 shows the meridional velocity extracted from a cross section of an eddy along a $y = y_c$ section. The peak velocity occurs at $x/L_E \approx 0.48$ and the majority of the signal is constrained to $|x/L_E| < 1$.

3.4 Internal Tide Forcing

We use MITgcm's open boundary conditions package `obcs` to produce the internal tide. At the west boundary, we prescribe the normal component of the velocity as

$$u(x = 0, z, t) = U_t \sin(\omega_0(t - T_0)) \cos\left(\frac{n\pi z}{H}\right) R(t - T_0), \qquad t \geq T_0, \tag{3.12}$$

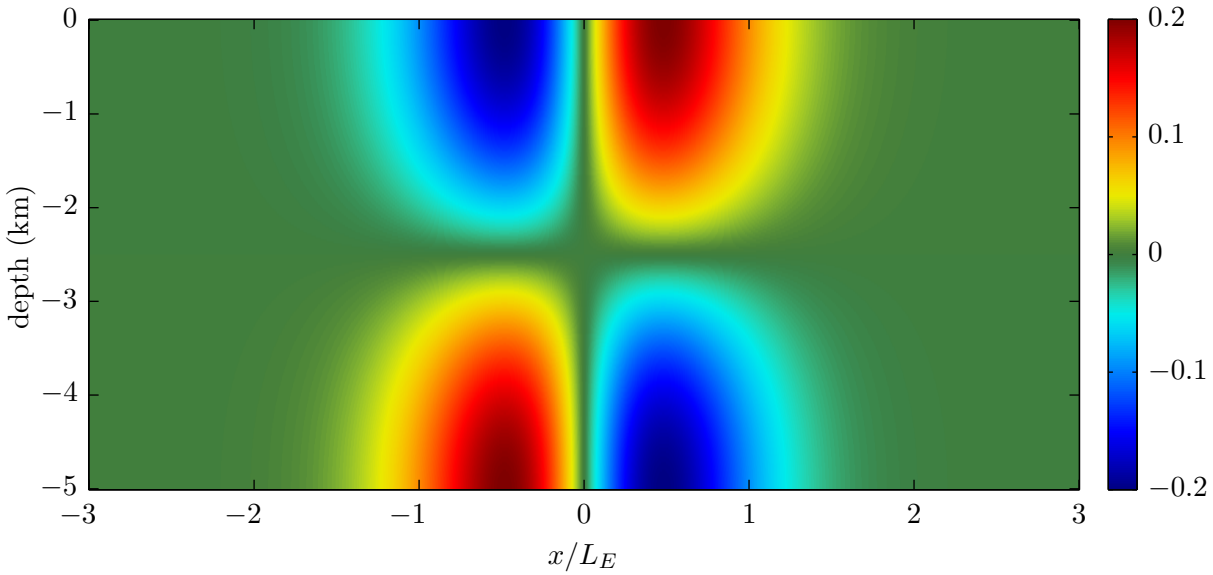

Figure 3.1: Velocity cross section of a baroclinic eddy in m/s for $U_E = 0.2$ m/s. The x-axis is normalised by L_E.

where n is the vertical mode number, U_t and ω_0 are the internal tide amplitude and M_2 tidal frequency, T_0 is the time where we switch on the forcing, and

$$R(\tau) = 0.5(1 - \cos(\omega_0 \tau/4)), \qquad \tau \leq 2T, \tag{3.13}$$

is a ramp-up function used to smoothly ramp the forcing up over two tidal periods and takes on a value of unity afterwards.

3.5 Relaxation Scheme

Following Martinsen and Engedahl (1987), we implement the flow relaxation scheme for both the horizontal momentum and salinity tracer equations. The vertical momentum equation is not relaxed due to use of the hydrostatic approximation. At the end of each time step, we restore the dynamic variables $(\tilde{u}, \tilde{v}, \tilde{S})$ toward a background state according to

$$\vec{u}_h = \hat{\alpha}\bar{\vec{u}}_h + (1 - \hat{\alpha})\tilde{\vec{u}}_h, \tag{3.14a}$$

$$S = \hat{\alpha}\bar{S} + (1 - \hat{\alpha})\tilde{S}, \tag{3.14b}$$

where $\hat{\alpha}(x, y)$ is a unitless restoration strength and $0 \leq \hat{\alpha}(x, y) \leq 1$. Areas where $\hat{\alpha}$ is zero experience no restoration while areas where $\hat{\alpha} = 1$ are completely restored. We restore toward the quiescent state with horizontally uniform stratification, $(\bar{\vec{u}}_h, \bar{S}) = (\vec{0}, \bar{S})$, so this flow relaxation scheme amounts to a simple sponge region. Use of some algebra (Martinsen and Engedahl, 1987) shows that this adjustment is equivalent to using forcing terms of the form

$$\vec{F}_h = -Q(\vec{u}_h - \bar{\vec{u}}_h) = -Q\vec{u}_h, \tag{3.15}$$

in the horizontal momentum equations and

$$F_S = -Q(S - \bar{S}) = -QS' \tag{3.16}$$

in the salinity tracer equation, where use of (2.4) converts it to the density forcing form

$$F_\rho = -Q(\rho - \bar{\rho}) = -Q\rho'. \tag{3.17}$$

The quantity Q assumes the form

$$Q = \frac{1}{\Delta t} \frac{\hat{\alpha}}{(1 - \hat{\alpha})}, \tag{3.18}$$

which amounts to a relaxation scheme that is time-step dependent, meaning that changing the model time step will change the relaxation strength. A preferred form for Q that does not depend on the time step is

$$Q = \frac{1}{\tau_r} \frac{\alpha_0}{(1 - \alpha_0)}, \tag{3.19}$$

where τ_r is a fixed relaxation time scale and α_0 is the desired relaxation strength. Equating these two expressions for Q and solving for $\hat{\alpha}$ yields

$$\hat{\alpha} = \frac{\alpha_0 \Delta t}{\tau_r - \tau_r \alpha_0 + \alpha_0 \Delta t}. \tag{3.20}$$

The relaxation scheme implementation takes α_0, τ_r, and Δt as inputs and computes $\hat{\alpha}$ online to ensure consistent relaxation strength across changes in Δt.

Table 3.1: Parameters common to all MITgcm simulations.

Parameter	Value
N_0	1.0×10^{-3} s^{-1}
ω_0	1.4053×10^{-4} s^{-1} (M_2 tide)
T	44712 s (one tidal period)
g	9.81 m s^{-2}
ρ_0	1028 kg m^{-3}
τ_r	7452 s

3.6 Scaling Analysis

The interaction experiments have eight parameters: three frequencies (f, ω_0 and N_0), the internal tide amplitude (U_t) and mode number (n), the water depth (H), and the eddy length scale (L_E) and peak velocity (U_E). From these, we can construct six independent dimensionless parameters, which we take as n, ω_0/N_0, U_t/N_0H, f/N_0, U_E/N_0H and L_E/H. In the MITgcm experiments that follow, we do not vary the first three, we use two values of the fourth via changing latitude and vary the fifth and sixth via changes in U_E and L_E. In the ray tracing experiments, we vary the first, fifth and sixth. Our results for an ocean of depth $H = 5$ km scale to an ocean of depth H_2 by multiplying L_E, U_t and U_E by H_2/H.

3.7 Model Parameters

We consider two f-planes. The first is a low-latitude regime where $f = 0.5 \times 10^{-4}$ s^{-1} (approximately 20°N) and the second is mid-latitude where $f = 1.0 \times 10^{-4}$ s^{-1} (approximately 43°N). The critical latitude for the M_2 tide, where $f = 0.5\,\omega_0$, is found at 28.9°N. Latitudes poleward of this value do not exhibit parametric subharmonic instability (PSI) (MacKinnon and Winters, 2005), thus we expect to find evidence of PSI only in the low-latitude regime.

Table 3.1 lists the parameters common to all of the MITgcm simulations. The domain size, resolution, eddy position, forcing magnitude and time step vary between experiment sets and are listed in the experiment descriptions of Chapters 5-8. All simulations are based on MITgcm version `checkpoint63b`. The changes made to the source code include the western open boundary forcing, the relaxation scheme, and routines to compute energy diagnostics. The energy diagnostics and their implementation are described in Chapter 4.

Chapter 4

Energetics

In this chapter we use the perturbation governing equations to derive both global kinetic and available potential energy budgets. Also contained in this chapter is the novel energy analysis aspect of this work. We begin by applying a modal decomposition to the momentum and density equations to find what we call projected momentum and density equations. We use these projected equations to derive pseudo-energy budgets for the barotropic mode and each baroclinic mode. A summary links the global budgets with the modal budgets in an intuitive manner, and we include an overview of the online computation of the energy budget terms using the MITgcm.

4.1 Global Energy Budgets

To derive a kinetic energy budget, we start by taking the dot product between $\rho_0\vec{u}_h$ and the unforced horizontal momentum equation (2.27a) (Gill, 1982), producing

$$\rho_0\vec{u}_h \cdot \left(\frac{D\vec{u}_h}{Dt} + f\hat{k}\times\vec{u}_h + \frac{1}{\rho_0}\nabla_h p'\right) = 0. \tag{4.1}$$

Use of the product rule and a bit of algebra produces

$$\rho_0\frac{\partial}{\partial t}\frac{1}{2}(u^2+v^2) + \nabla\cdot\left(\vec{u}[p' + \rho_0\frac{1}{2}(u^2+v^2)]\right) + \rho' g w = 0. \tag{4.2}$$

which is a conservation equation that governs the evolution of kinetic energy density. Integrating over a volume V produces the kinetic energy budget

$$\frac{\mathrm{d}}{\mathrm{d}t}\iiint_V \rho_0 \frac{1}{2}(u^2+v^2)\,\mathrm{d}V + \iint_{\delta V} \vec{u}\cdot\hat{n}[p' + \rho_0\frac{1}{2}(u^2+v^2)]\,\mathrm{d}S + \iiint_V \rho' g w\,\mathrm{d}V = 0, \tag{4.3}$$

where

$$K \equiv \frac{\rho_0}{2}\iiint_V (u^2+v^2)\,\mathrm{d}V \tag{4.4}$$

is the total kinetic energy in V,

$$W \equiv \oiint_{\delta V} p'\vec{u}\cdot\hat{n}\,\mathrm{d}S \tag{4.5}$$

is the work done at the boundaries of V,

$$K_f \equiv \frac{\rho_0}{2}\oiint_{\delta V}(u^2+v^2)\vec{u}\cdot\hat{n}\,\mathrm{d}S \tag{4.6}$$

is the nonlinear flux of kinetic energy through the boundaries of V and

$$C \equiv \iiint_V \rho' g w\,\mathrm{d}V \tag{4.7}$$

is the available potential-kinetic energy conversion term. We take $\hat{n}$ to be the unit outward normal to V. All terms are quadratic in terms of a perturbation quantity except K_f which is cubic, thus we expect K_f to be much smaller than the others.

We find the available potential energy budget by multiplying the unforced density equation (2.27d) by $\frac{g^2\rho'}{\rho_0 N_0^2}$, giving

$$\frac{g^2\rho'}{\rho_0 N_0^2}\left(\frac{D\rho'}{Dt} - \frac{\rho_0 w}{g}N_0^2\right) = 0, \tag{4.8}$$

and use some algebra to arrive at

$$\frac{\partial}{\partial t}\frac{g^2\rho'^2}{2\rho_0 N_0^2} + \frac{g^2}{2\rho_0 N_0^2}\nabla\cdot(\vec{u}\rho'^2) - \rho' g w = 0, \tag{4.9}$$

which is a governing equation for available potential energy density. Integrating over a volume V produces the available potential energy budget

$$\frac{\mathrm{d}}{\mathrm{d}t}\iiint_V \frac{g^2\rho'^2}{2N_0^2\rho_0}\,\mathrm{d}V + \frac{g^2}{2\rho_0 N_0^2}\iint_{\delta V}\vec{u}\cdot\hat{n}\rho'^2\,\mathrm{d}S - \iiint_V \rho' g w\,\mathrm{d}V = 0, \tag{4.10}$$

where

$$A \equiv \frac{g^2}{2\rho_0 N_0^2}\iiint_V \rho'^2\,\mathrm{d}V \tag{4.11}$$

is the total available potential energy in volume V,

$$A_f \equiv \frac{g^2}{2\rho_0 N_0^2}\oiint_{\delta V}\rho'^2\vec{u}\cdot\hat{n}\,\mathrm{d}S \tag{4.12}$$

is the nonlinear flux of available potential energy through the boundaries of V, and the last term is (4.7) with the opposite sign. As in the kinetic energy budget, only A_f is cubic in terms of a perturbation quantity, so we expect it to be much smaller than the others.

Flow relaxation scheme

The forcing terms associated with the relaxation scheme described in Section 3.5 contribute to the energy budget in the form of energy sinks. Taking the dot product between (3.15) and $\rho_0\vec{u}$, and integrating over the volume V gives the contribution to the kinetic energy budget

$$F_K \equiv \rho_0\iiint_V Q(u^2+v^2)\,dV. \tag{4.13}$$

Similarly, scaling (3.17) by $\dfrac{g^2\rho'}{\rho_0 N_0^2}$ and integrating over the same volume V gives the contribution to the available potential energy budget,

$$F_A \equiv \iiint_V Q\frac{g^2\rho'^2}{\rho_0 N_0^2}\,dV. \tag{4.14}$$

The integrand of both (4.13) and (4.14) are always non-negative, which means the terms F_K and F_A are either energy sinks or equal to zero, but are never energy sources.

4.2 Projected Governing Equations

We use the vertical structure function from the polarization relations described in Section 2.2.3 to decompose the model flow fields into contributions from each vertical mode via

$$\{\vec{u}_h, p'\} = \{\vec{u}_{h_0}, p'_0\} + \sum_{n=1}^{\infty} \{\vec{u}_{h_n}, p'_n\} \cos(m_n z), \tag{4.15}$$

$$\{w, \rho'\} = \sum_{n=1}^{\infty} \{w_n, \rho'_n\} \sin(m_n z), \tag{4.16}$$

where the coefficients are functions of x, y and t. To find the projected horizontal momentum equations, we substitute the decompositions (4.15) and (4.16) into the unforced horizontal momentum equation (2.27a) and collect terms at each vertical mode. The linear terms are straightforward,

$$\frac{\partial \vec{u}_h}{\partial t} = \frac{\partial}{\partial t}\left(\vec{u}_{h_0} + \sum_{n=1}^{\infty} \vec{u}_{h_n} \cos(m_n z)\right) = \frac{\partial \vec{u}_{h_0}}{\partial t} + \sum_{n=1}^{\infty} \frac{\partial \vec{u}_{h_n}}{\partial t} \cos(m_n z), \tag{4.17}$$

$$\vec{f} \times \vec{u}_h = \vec{f} \times \left(\vec{u}_{h_0} + \sum_{n=1}^{\infty} \vec{u}_{h_n} \cos(m_n z)\right) = \vec{f} \times \vec{u}_{h_0} + \sum_{n=1}^{\infty} \vec{f} \times \vec{u}_{h_n} \cos(m_n z), \tag{4.18}$$

$$-\frac{1}{\rho_0}\nabla_h p' = -\frac{1}{\rho_0}\nabla_h \left(p'_0 + \sum_{n=1}^{\infty} p'_n \cos(m_n z)\right) = -\frac{1}{\rho_0}\nabla_h p'_0 - \frac{1}{\rho_0}\sum_{n=1}^{\infty} \nabla_h p'_n \cos(m_n z). \tag{4.19}$$

We hande the nonlinear terms in two parts via

$$(\vec{u} \cdot \nabla)\vec{u}_h = (\vec{u}_h \cdot \nabla_h)\vec{u}_h + w\frac{\partial \vec{u}_h}{\partial z} \equiv \vec{N}^u. \tag{4.20}$$

Substituting the decomposition into the first part yields

$$
\begin{aligned}
(\vec{u}_h \cdot \nabla_h)\vec{u}_h =& \left(\left[\vec{u}_{h_0} + \sum_{i=1}^{\infty} \vec{u}_{h_i} \cos(m_i z) \right] \cdot \nabla_h \right) \left(\vec{u}_{h_0} + \sum_{j=1}^{\infty} \vec{u}_{h_j} \cos(m_j z) \right), \\
=& \left(\vec{u}_{h_0} \cdot \nabla_h + \sum_{i=1}^{\infty} \vec{u}_{h_i} \cos(m_i z) \cdot \nabla_h \right) \left(\vec{u}_{h_0} + \sum_{j=1}^{\infty} \vec{u}_{h_j} \cos(m_j z) \right), \\
=& (\vec{u}_{h_0} \cdot \nabla_h)\vec{u}_{h_0} + \left(\vec{u}_{h_0} \cdot \nabla_h \left[\sum_{i=1}^{\infty} \vec{u}_{h_i} \right] + \left[\sum_{i=1}^{\infty} \vec{u}_{h_i} \cdot \nabla_h \right] \vec{u}_{h_0} \right) \cos m_i z \\
&+ \left(\left[\sum_{i=1}^{\infty} \vec{u}_{h_i} \right] \cdot \nabla_h \left[\sum_{j=1}^{\infty} \vec{u}_{h_j} \right] \right) \cos(m_i z) \cos(m_j z), \\
=& (\vec{u}_{h_0} \cdot \nabla_h)\vec{u}_{h_0} + \left(\sum_{i=1}^{\infty} (\vec{u}_{h_0} \cdot \nabla_h)\vec{u}_{h_i} + (\vec{u}_{h_i} \cdot \nabla_h)\vec{u}_{h_0} \right) \cos(m_i z) \\
&+ \left(\sum_{i=1}^{\infty} \sum_{j=1}^{\infty} (\vec{u}_{h_i} \cdot \nabla_h)\vec{u}_{h_j} \right) \cos(m_i z) \cos(m_j z), \\
=& (\vec{u}_{h_0} \cdot \nabla_h)\vec{u}_{h_0} + \sum_{i=1}^{\infty} \left((\vec{u}_{h_0} \cdot \nabla_h)\vec{u}_{h_i} + (\vec{u}_{h_i} \cdot \nabla_h)\vec{u}_{h_0} \right) \cos(m_i z) \\
&+ \frac{1}{2} \left(\sum_{i=1}^{\infty} \sum_{j=1}^{\infty} (\vec{u}_{h_i} \cdot \nabla_h)\vec{u}_{h_j} \right) \left[\cos((m_i - m_j)z) + \cos((m_i + m_j)z) \right],
\end{aligned}
$$

and we collect terms with the same vertical mode,

$$
\begin{aligned}
(\vec{u}_h \cdot \nabla_h)\vec{u}_h = (\vec{u}_{h_0} \cdot \nabla_h)\vec{u}_{h_0} + \frac{1}{2}\sum_{i=1}^{\infty}(\vec{u}_{h_i} \cdot \nabla_h)\vec{u}_{h_i} \\
&+ \Bigg[((\vec{u}_{h_0} \cdot \nabla_h)\vec{u}_{h_1} + (\vec{u}_{h_1} \cdot \nabla_h)\vec{u}_{h_0}) \\
&+ \frac{1}{2}\sum_{i=1}^{\infty}\Big((\vec{u}_{h_i} \cdot \nabla_h)\vec{u}_{h_{i+1}} + (\vec{u}_{h_{i+1}} \cdot \nabla_h)\vec{u}_{h_i}\Big)\Bigg] \cos(m_1 z) \\
&+ \Bigg[((\vec{u}_{h_0} \cdot \nabla_h)\vec{u}_{h_2} + (\vec{u}_{h_2} \cdot \nabla_h)\vec{u}_{h_0}) + \frac{1}{2}(\vec{u}_{h_1} \cdot \nabla_h)\vec{u}_{h_1} \\
&\quad + \frac{1}{2}\sum_{i=1}^{\infty}\Big((\vec{u}_{h_i} \cdot \nabla_h)\vec{u}_{h_{i+2}} + (\vec{u}_{h_{i+2}} \cdot \nabla_h)\vec{u}_{h_i}\Big)\Bigg] \cos(m_2 z) \\
&+ \Bigg[((\vec{u}_{h_0} \cdot \nabla_h)\vec{u}_{h_3} + (\vec{u}_{h_3} \cdot \nabla_h)\vec{u}_{h_0}) + \frac{1}{2}\left((\vec{u}_{h_1} \cdot \nabla_h)\vec{u}_{h_2} + (\vec{u}_{h_2} \cdot \nabla_h)\vec{u}_{h_1}\right) \\
&\quad + \frac{1}{2}\sum_{i=1}^{\infty}\Big((\vec{u}_{h_i} \cdot \nabla_h)\vec{u}_{h_{i+3}} + (\vec{u}_{h_{i+3}} \cdot \nabla_h)\vec{u}_{h_i}\Big)\Bigg] \cos(m_3 z) \\
&+ \dots .
\end{aligned}
\tag{4.21}
$$

Substituting the decomposition into the second part yields

$$
\begin{aligned}
w\frac{\partial \vec{u}_h}{\partial z} =& \Big(\sum_{i=1}^{\infty} w_i \sin(m_i z)\Big)\Big(-\sum_{j=1}^{\infty}\vec{u}_{h_j} m_j \sin(m_j z)\Big), \\
=& -\sum_{i=1}^{\infty}\sum_{j=1}^{\infty} w_i \vec{u}_{h_j} m_j \sin(m_i z)\sin(m_j z), \\
=& \frac{1}{2}\sum_{i=1}^{\infty}\sum_{j=1}^{\infty} w_i \vec{u}_{h_j} m_j \big(\cos((m_i + m_j)z) - \cos((m_i - m_j)z)\big),
\end{aligned}
$$

and again collect terms with the same vertical mode,

$$\begin{aligned} w\frac{\partial \vec{u}_h}{\partial z} =& -\frac{1}{2}\sum_{i=1}^{\infty} w_i \vec{u}_{h_i} m_i - \frac{1}{2}\left[\sum_{i=1}^{\infty} w_i \vec{u}_{h_{i+1}} m_{i+1} + w_{i+1}\vec{u}_{h_i} m_i\right]\cos(m_1 z) \\ &+ \frac{1}{2}\left[w_1 \vec{u}_{h_1} m_1 - \sum_{i=1}^{\infty}(w_i \vec{u}_{h_{i+2}} m_{i+2} + w_{i+2}\vec{u}_{h_i} m_i)\right]\cos(m_2 z) \\ &+ \frac{1}{2}\left[w_2 \vec{u}_{h_1} m_1 + w_1 \vec{u}_{h_2} m_2 - \sum_{i=1}^{\infty}(w_i \vec{u}_{h_{i+3}} m_{i+3} + w_{i+3}\vec{u}_{h_i} m_i)\right]\cos(m_3 z) \\ &+ \ldots . \end{aligned} \tag{4.22}$$

Combining these results yields

$$\vec{N}^u = (\vec{u}_h \cdot \nabla_h)\vec{u}_h + w\frac{\partial \vec{u}_h}{\partial z} = \vec{N}_0^u + \sum_{n=1}^{\infty} \vec{N}_n^u \cos(m_n z), \tag{4.23}$$

where

$$\vec{N}_0^u = (\vec{u}_{h_0}\cdot\nabla_h)\vec{u}_{h_0} + \frac{1}{2}\sum_{i=1}^{\infty}(\vec{u}_{h_i}\cdot\nabla_h)\vec{u}_{h_i} - \frac{1}{2}\sum_{i=1}^{\infty} w_i\vec{u}_{h_i}m_i, \tag{4.24}$$

$$\begin{aligned}\vec{N}_1^u = &\left[((\vec{u}_{h_0}\cdot\nabla_h)\vec{u}_{h_1} + (\vec{u}_{h_1}\cdot\nabla_h)\vec{u}_{h_0}) + \frac{1}{2}\sum_{i=1}^{\infty}\left((\vec{u}_{h_i}\cdot\nabla_h)\vec{u}_{h_{i+1}} + (\vec{u}_{h_{i+1}}\cdot\nabla_h)\vec{u}_{h_i}\right)\right] \\ &- \frac{1}{2}\left[\sum_{i=1}^{\infty} w_i\vec{u}_{h_{i+1}}m_{i+1} + w_{i+1}\vec{u}_{h_i}m_i\right],\end{aligned} \tag{4.25}$$

$$\begin{aligned}\vec{N}_2^u = &\left[((\vec{u}_{h_0}\cdot\nabla_h)\vec{u}_{h_2} + (\vec{u}_{h_2}\cdot\nabla_h)\vec{u}_{h_0}) + \frac{1}{2}(\vec{u}_{h_1}\cdot\nabla_h)\vec{u}_{h_1}\right. \\ &\left. + \frac{1}{2}\sum_{i=1}^{\infty}\left((\vec{u}_{h_i}\cdot\nabla_h)\vec{u}_{h_{i+2}} + (\vec{u}_{h_{i+2}}\cdot\nabla_h)\vec{u}_{h_i}\right)\right] \\ &+ \frac{1}{2}\left[w_1\vec{u}_{h_1}m_1 - \sum_{i=1}^{\infty}(w_i\vec{u}_{h_{i+2}}m_{i+2} + w_{i+2}\vec{u}_{h_i}m_i)\right]\end{aligned} \tag{4.26}$$

$$\begin{aligned}\vec{N}_3^u = &\left[((\vec{u}_{h_0}\cdot\nabla_h)\vec{u}_{h_3} + (\vec{u}_{h_3}\cdot\nabla_h)\vec{u}_{h_0}) + \frac{1}{2}\left((\vec{u}_{h_1}\cdot\nabla_h)\vec{u}_{h_2} + (\vec{u}_{h_2}\cdot\nabla_h)\vec{u}_{h_1}\right)\right. \\ &\left. + \frac{1}{2}\sum_{i=1}^{\infty}\left((\vec{u}_{h_i}\cdot\nabla_h)\vec{u}_{h_{i+3}} + (\vec{u}_{h_{i+3}}\cdot\nabla_h)\vec{u}_{h_i}\right)\right] \\ &+ \frac{1}{2}\left[w_2\vec{u}_{h_1}m_1 + w_1\vec{u}_{h_2}m_2 - \sum_{i=1}^{\infty}(w_i\vec{u}_{h_{i+3}}m_{i+3} + w_{i+3}\vec{u}_{h_i}m_i)\right]\end{aligned} \tag{4.27}$$

$$\vec{N}_4^u = \dots.$$

We now write the total horizontal momentum equation (2.27a) as a sum of the contributions from each vertical modes

$$\frac{D\vec{u}_h}{Dt} + f\hat{k}\times\vec{u}_h + \frac{1}{\rho_0}\nabla_h p' = \vec{M}_0 + \sum_{n=1}^{\infty}\vec{M}_n\cos(m_n z) = 0, \tag{4.28}$$

where the coefficients of each vertical mode sum to zero, yielding the barotropic and baroclinic momentum equations

$$\vec{M}_0 = \frac{\partial\vec{u}_{h_0}}{\partial t} + N_0^u + \vec{f}\times\vec{u}_{h_0} + \frac{1}{\rho_0}\nabla_h p_0' = 0, \tag{4.29}$$

$$\vec{M}_n = \frac{\partial\vec{u}_{h_n}}{\partial t} + N_n^u + \vec{f}\times\vec{u}_{h_n} + \frac{1}{\rho_0}\nabla_h p_n' = 0, \qquad n\in\mathbb{N}. \tag{4.30}$$

Substituting the decompositions (4.15) and (4.16) into the vertical momentum equation (2.27b), gives

$$\frac{\partial p'}{\partial z} = -g\rho' \tag{4.31}$$

$$\frac{\partial}{\partial z}\left(p'_0 + \sum_{n=1}^{\infty} p'_n \cos(m_n z)\right) = -g\left(\sum_{n=1}^{\infty} \rho'_n \sin(m_n z)\right) \tag{4.32}$$

$$-\sum_{n=1}^{\infty} p'_n m_n \sin(m_n z) = -g\sum_{n=1}^{\infty} \rho'_n \sin(m_n z) \tag{4.33}$$

and equating the coefficients of each mode yields

$$p'_n m_n = g\rho'_n. \tag{4.34}$$

Lastly, upon substitution of (4.15) and (4.16) into the unforced density equation (2.27d), we quickly find the linear terms,

$$\frac{\partial \rho'}{\partial t} = \frac{\partial}{\partial t}\sum_{n=1}^{\infty} \rho'_n \sin(m_n z) = \sum_{n=1}^{\infty} \frac{\partial \rho'_n}{\partial t} \sin(m_n z), \tag{4.35}$$

$$\frac{-\rho_0 N_0^2}{g} w = \frac{-\rho_0 N_0^2}{g} \sum_{n=1}^{\infty} w_n \sin(m_n z) \tag{4.36}$$

and break the nonlinear term into two parts,

$$(\vec{u}\cdot\nabla)\rho' = (\vec{u}_h \cdot \nabla_h)\rho' + w\frac{\partial \rho'}{\partial z} \equiv N^{\rho}. \tag{4.37}$$

Substituting the decompositions into the first part yields

$$
\begin{aligned}
(\vec{u}_h \cdot \nabla_h)\rho' =& \bigg(\Big[\vec{u}_{h_0} + \sum_{i=1}^{\infty} \vec{u}_{h_i} \cos(m_i z) \Big] \cdot \nabla_h \bigg) \bigg(\sum_{j=1}^{\infty} \rho'_j \sin(m_j z) \bigg), \\
=& \bigg(\vec{u}_{h_0} \cdot \nabla_h + \sum_{i=1}^{\infty} \vec{u}_{h_i} \cos(m_i z) \cdot \nabla_h \bigg) \bigg(\sum_{j=1}^{\infty} \rho'_j \sin(m_j z) \bigg), \\
=& (\vec{u}_{h_0} \cdot \nabla_h) \bigg(\sum_{j=1}^{\infty} \rho'_j \sin(m_j z) \bigg) + \bigg[\sum_{i=1}^{\infty} \sum_{j=1}^{\infty} (\vec{u}_{h_i} \cdot \nabla_h) \rho'_j \bigg] \cos(m_i z) \sin(m_j z), \\
=& (\vec{u}_{h_0} \cdot \nabla_h) \bigg(\sum_{j=1}^{\infty} \rho'_j \sin(m_j z) \bigg) \\
&+ \frac{1}{2} \sum_{i=1}^{\infty} \sum_{j=1}^{\infty} (\vec{u}_{h_i} \cdot \nabla_h) \rho'_j \big[\sin((m_i + m_j) z) - \sin((m_i - m_j) z) \big], \qquad (4.38)
\end{aligned}
$$

and we collect terms with the same vertical mode,

$$
\begin{aligned}
(\vec{u}_h \cdot \nabla_h)\rho' =& \bigg[(\vec{u}_{h_0} \cdot \nabla_h)(\rho'_1) + \frac{1}{2} \sum_{i=1}^{\infty} \Big((\vec{u}_{h_i} \cdot \nabla_h) \rho'_{i+1} - (\vec{u}_{h_{i+1}} \cdot \nabla_h) \rho'_i \Big) \bigg] \sin(m_1 z) \\
&+ \bigg[(\vec{u}_{h_0} \cdot \nabla_h)(\rho'_2) + \frac{1}{2} \sum_{i=1}^{\infty} \Big((\vec{u}_{h_i} \cdot \nabla_h) \rho'_{i+2} - (\vec{u}_{h_{i+2}} \cdot \nabla_h) \rho'_i \Big) \qquad (4.39) \\
&+ \frac{1}{2} (\vec{u}_{h_1} \cdot \nabla_h) \rho'_1 \bigg] \sin(m_2 z) \\
&+ \bigg[(\vec{u}_{h_0} \cdot \nabla_h)(\rho'_3) + \frac{1}{2} \sum_{i=1}^{\infty} \Big((\vec{u}_{h_i} \cdot \nabla_h) \rho'_{i+3} - (\vec{u}_{h_{i+3}} \cdot \nabla_h) \rho'_i \Big) \\
&\quad + \frac{1}{2} \Big((\vec{u}_{h_1} \cdot \nabla_h) \rho'_2 + (\vec{u}_{h_2} \cdot \nabla_h) \rho'_1 \Big) \bigg] \sin(m_3 z) \\
&+ \ldots . \qquad (4.40)
\end{aligned}
$$

Substitution into the second term yields

$$\begin{aligned} w\frac{\partial \rho'}{\partial z} =& \left(\sum_{i=1}^{\infty} w_i \sin(m_i z) \right) \left(\sum_{j=1}^{\infty} \rho'_j m_j \cos(m_j z) \right), \\ =& \sum_{i=1}^{\infty} \sum_{j=1}^{\infty} w_i \rho'_j m_j \sin(m_i z) \cos(m_j z), \\ =& \frac{1}{2} \sum_{i=1}^{\infty} \sum_{j=1}^{\infty} w_i \rho'_j m_j \big[\sin((m_i + m_j)z) + \sin((m_i - m_j)z) \big], \end{aligned} \tag{4.41}$$

and we collect terms at each vertical mode,

$$\begin{aligned} w\frac{\partial \rho'}{\partial z} =& \frac{1}{2} \sum_{i=1}^{\infty} \left(w_{i+1} \rho'_i m_i - w_i \rho'_{i+1} m_{i+1} \right) \sin(m_1 z) \\ &+ \frac{1}{2} \left[w_i \rho'_1 m_1 + \sum_{i=1}^{\infty} \left(w_{i+2} \rho'_i m_i - w_i \rho'_{i+2} m_{i+2} \right) \right] \sin(m_2 z) \\ &+ \frac{1}{2} \left[w_2 \rho'_1 m_1 + w_1 \rho'_2 m_2 + \sum_{i=1}^{\infty} \left(w_{i+3} \rho'_i m_i - w_i \rho'_{i+3} m_{i+3} \right) \right] \sin(m_3 z) \\ &+ \dots . \end{aligned} \tag{4.42}$$

Combining these results yields

$$N^{\rho} = (\vec{u}_h \cdot \nabla_h)\rho' + w\frac{\partial \rho'}{\partial z} = \sum_{n=1}^{\infty} N_n^{\rho} \sin(m_n z), \tag{4.43}$$

where

$$N_1^\rho = \left[(\vec{u}_{h_0}\cdot\nabla_h)(\rho_1') + \frac{1}{2}\sum_{i=1}^{\infty}\left((\vec{u}_{h_i}\cdot\nabla_h)\rho_{i+1}' - (\vec{u}_{h_{i+1}}\cdot\nabla_h)\rho_i'\right)\right] + \frac{1}{2}\sum_{i=1}^{\infty}\left(w_{i+1}\rho_i' m_i - w_i\rho_{i+1}' m_{i+1}\right) \tag{4.44}$$

$$N_2^\rho = \left[(\vec{u}_{h_0}\cdot\nabla_h)(\rho_2') + \frac{1}{2}\sum_{i=1}^{\infty}\left((\vec{u}_{h_i}\cdot\nabla_h)\rho_{i+2}' - (\vec{u}_{h_{i+2}}\cdot\nabla_h)\rho_i'\right) + \frac{1}{2}(\vec{u}_{h_1}\cdot\nabla_h)\rho_1'\right] + \frac{1}{2}\left[w_1\rho_1' m_1 + \sum_{i=1}^{\infty}\left(w_{i+2}\rho_i' m_i - w_i\rho_{i+2}' m_{i+2}\right)\right] \tag{4.45}$$

$$N_3^\rho = \left[(\vec{u}_{h_0}\cdot\nabla_h)(\rho_3') + \frac{1}{2}\sum_{i=1}^{\infty}\left((\vec{u}_{h_i}\cdot\nabla_h)\rho_{i+3}' - (\vec{u}_{h_{i+3}}\cdot\nabla_h)\rho_i'\right) + \frac{1}{2}\left((\vec{u}_{h_1}\cdot\nabla_h)\rho_2' + (\vec{u}_{h_2}\cdot\nabla_h)\rho_1'\right)\right] + \frac{1}{2}\left[w_2\rho_1' m_1 + w_1\rho_2' m_2 + \sum_{i=1}^{\infty}\left(w_{i+3}\rho_i' m_i - w_i\rho_{i+3}' m_{i+3}\right)\right] \tag{4.46}$$

$$N_4^\rho = \ldots.$$

We write the density equation as a sum of contributions from each vertical mode,

$$\frac{D\rho'}{Dt} - \frac{\rho_0 N_0^2}{g}w = \sum_{n=1}^{\infty} D_n \sin(m_n z) = 0, \tag{4.47}$$

where the coefficients of each mode sum to zero, yielding modal density equations

$$D_n = \frac{\partial\rho_n'}{\partial t} + N_n^\rho - \frac{\rho_0 N_0^2}{g}w_n = 0, \qquad n \in \mathbb{N}. \tag{4.48}$$

4.3 Modal Energy Budgets

We desire an evolution equation for the kinetic energy at each mode, and begin with the barotropic mode by taking the dot product between $\rho_0 H\vec{u}_{h_0}$ and the barotropic momentum equation $\vec{M}_0$, giving

$$\rho_0 H\left(\vec{u}_{h_0}\cdot\frac{\partial\vec{u}_{h_0}}{\partial t} + \vec{u}_{h_0}\cdot\vec{N}_0^u + \vec{u}_{h_0}\cdot\vec{f}\times\vec{u}_{h_0} + \frac{1}{\rho_0}\vec{u}_{h_0}\cdot\nabla_h p_0'\right) = 0. \tag{4.49}$$

We then use $\vec{u}_{h_0} \cdot \vec{f} \times \vec{u}_{h_0} = 0$ and $\nabla_h \cdot \vec{u}_{h_0} = 0$ to get

$$\rho_0 \frac{H}{2} \frac{\partial (u_0^2 + v_0^2)}{\partial t} + \rho_0 H \vec{u}_{h_0} \cdot \vec{N}_0^u + H \nabla_h \cdot (\vec{u}_{h_0} p_0') = 0. \tag{4.50}$$

This is an evolution equation for the vertically integrated barotropic kinetic energy density. Integrating over an area A yields

$$\rho_0 \frac{H}{2} \frac{\mathrm{d}}{\mathrm{d}t} \iint\limits_A (u_0^2 + v_0^2) \, \mathrm{d}A + \rho_0 H \iint\limits_A \vec{u}_{h_0} \cdot \vec{N}_0^u \, \mathrm{d}A + H \iint\limits_A \nabla_h \cdot (\vec{u}_{h_0} p_0') \, \mathrm{d}A = 0, \tag{4.51}$$

and use of the divergence theorem leaves the barotropic kinetic energy budget

$$\rho_0 \frac{H}{2} \frac{\mathrm{d}}{\mathrm{d}t} \iint\limits_A (u_0^2 + v_0^2) \, \mathrm{d}A + \rho_0 H \iint\limits_A \vec{u}_{h_0} \cdot \vec{N}_0^u \, \mathrm{d}A + H \oint\limits_{\delta A} (\vec{u}_{h_0} \cdot \hat{n}) p_0' \, \mathrm{d}S = 0. \tag{4.52}$$

We identify

$$K_0 \equiv \rho_0 \frac{H}{2} \iint\limits_A (u_0^2 + v_0^2) \, \mathrm{d}A \tag{4.53}$$

as the total barotropic kinetic energy,

$$S_0 \equiv \rho_0 H \iint\limits_A \vec{u}_{h_0} \cdot \vec{N}_0^u \, \mathrm{d}A \tag{4.54}$$

as the barotropic kinetic energy sink, and

$$W_0 \equiv H \oint\limits_{\delta A} (\vec{u}_{h_0} \cdot \hat{n}) p_0' \, \mathrm{d}S \tag{4.55}$$

as the total barotropic work at the boundaries. We use a similar procedure for each of the n baroclinic modes, which is to take the dot product $(\rho_0 H/2) \vec{u}_{h_n} \cdot \vec{M}_n$

$$\frac{\rho_0 H}{2} \left(\vec{u}_{h_n} \cdot \frac{\partial \vec{u}_{h_n}}{\partial t} + \vec{u}_{h_n} \cdot \vec{N}_n^u + \vec{u}_{h_n} \cdot \vec{f} \times \vec{u}_{h_n} + \frac{1}{\rho_0} \vec{u}_{h_n} \cdot \nabla_h p_n' \right) = 0, \tag{4.56}$$

then use $\vec{u}_{h_n} \cdot \vec{f} \times \vec{u}_{h_n} = 0$ and $\nabla_h \cdot (p_n' \vec{u}_{h_n}) = \vec{u}_{h_n} \cdot \nabla p_n' + p_n' \nabla_h \cdot \vec{u}_{h_n}$ to get

$$\frac{\rho_0 H}{4} \frac{\partial (u_n^2 + v_n^2)}{\partial t} + \frac{\rho_0 H}{2} \vec{u}_{h_n} \cdot \vec{N}_n^u + \frac{H}{2} \left(\nabla_h \cdot (p_n' \vec{u}_{h_n}) - p_n' \nabla_h \cdot \vec{u}_{h_n} \right) = 0, \tag{4.57}$$

and finally apply $\nabla_h \cdot \vec{u}_{h_n} = -m_n w_n$ to get

$$\frac{\rho_0 H}{4}\frac{\partial(u_n^2+v_n^2)}{\partial t} + \frac{\rho_0 H}{2}\vec{u}_{h_n}\cdot\vec{N}_n^u + \frac{H}{2}\left(\nabla_h\cdot(p_n'\vec{u}_{h_n}) + p_n' m_n w_n\right) = 0, \tag{4.58}$$

which is an evolution equation for the vertically integrated kinetic energy density at mode-n. Integrating over an area A, using the divergence theorem, and substituting (4.34) yields the baroclinic kinetic energy budget at mode-n

$$\frac{\rho_0 H}{4}\frac{\mathrm{d}}{\mathrm{d}t}\iint_A (u_n^2+v_n^2)\,\mathrm{d}A + \frac{\rho_0 H}{2}\iint_A \vec{u}_{h_n}\cdot\vec{N}_n^u\,\mathrm{d}A + \frac{H}{2}\oint_{\delta A}(\vec{u}_{h_n}\cdot\hat{n})p_n'\,\mathrm{d}S + \frac{Hg}{2}\iint_A \rho_n' w_n\,\mathrm{d}A = 0. \tag{4.59}$$

We identify

$$K_n \equiv \frac{\rho_0 H}{4}\iint_A (u_n^2+v_n^2)\,\mathrm{d}A \tag{4.60}$$

as the total kinetic energy at mode-n,

$$S_n^u \equiv \frac{\rho_0 H}{2}\iint_A \vec{u}_{h_n}\cdot\vec{N}_n^u\,\mathrm{d}A \tag{4.61}$$

as the kinetic energy sink at mode-n,

$$W_n \equiv \frac{H}{2}\oint_{\delta A} p_n'\vec{u}_{h_n}\cdot\hat{n}\,\mathrm{d}S \tag{4.62}$$

as the work done at the boundaries at mode-n, and

$$C_n \equiv \frac{Hg}{2}\iint_A \rho_n' w_n\,\mathrm{d}A \tag{4.63}$$

as the kinetic-available potential energy conversion term at mode-n. Lastly, we multiply D_n by $(Hg^2/2\rho_0 N_0^2)\rho_n'$, producing

$$\frac{g^2 H}{4\rho_0 N_0^2}\frac{\partial}{\partial t}\rho_n'^2 + \frac{g^2 H}{2\rho_0 N_0^2}\rho_n' N_n^\rho - \frac{Hg}{2}\rho_n' w_n = 0, \tag{4.64}$$

which is a governing equation for vertically integrated available potential energy density at mode-n. Integrating over an area A gives the available potential energy budget at mode-n

$$\frac{g^2 H}{4\rho_0 N_0^2}\frac{\mathrm{d}}{\mathrm{d}t}\iint_A \rho_n'^2\,\mathrm{d}A + \frac{g^2 H}{2\rho_0 N_0^2}\iint_A \rho_n' N_n^\rho\,\mathrm{d}A - \frac{Hg}{2}\iint_A \rho_n' w_n\,\mathrm{d}A = 0, \tag{4.65}$$

and we identify

$$A_n \equiv \frac{g^2 H}{4\rho_0 N_0^2}\iint_A \rho_n'^2\,\mathrm{d}A \tag{4.66}$$

as the available potential energy at mode-n, and

$$S_n^\rho \equiv \frac{g^2 H}{2\rho_0 N_0^2}\iint_A \rho_n' N_n^\rho\,\mathrm{d}A \tag{4.67}$$

as the available potential energy sink at mode-n. The last term is the same as (4.63) but with the opposite sign.

Flow relaxation term

Substituting the decompositions (4.15) and (4.16) into (3.15) and collecting terms at each vertical mode, we find the projected horizontal momentum forcing

$$\vec{F}_h = Q\vec{u}_{h_0} + \sum_{n=1}^{\infty} Q\vec{u}_{h_n}\cos(m_n z) \equiv \vec{F}_{h_0} + \sum_{n=1}^{\infty}\vec{F}_{h_n}\cos(m_n z), \tag{4.68}$$

and similarly substituting into (3.17) gives the projected density forcing

$$F_\rho = \sum_{n=1}^{\infty} Q\rho_n'\sin(m_n z) \equiv \sum_{n=1}^{\infty} F_{\rho_n}\sin(m_n z). \tag{4.69}$$

Following same dot product and integrate procedure as above, we find the contribution to the barotropic kinetic energy budget due to forcing is

$$F_{K_0} = \iint_A \rho_0 H\vec{u}_{h_0}\cdot Q\vec{u}_{h_0}\mathrm{d}A = \rho_0 H\iint_A Q(u_0^2 + v_0^2)\mathrm{d}A. \tag{4.70}$$

Similarly for the mode-n baroclinic budget we find

$$F_{K_n} = \iint_A \frac{\rho_0 H}{2} \vec{u}_{h_n} \cdot Q\vec{u}_{h_n} \mathrm{d}A = \frac{\rho_0 H}{2} \iint_A Q(u_n^2 + v_n^2) \mathrm{d}A, \tag{4.71}$$

and for the mode-n available potential energy budget we find

$$F_{A_n} = \iint_A \frac{g^2 H \rho_n'}{2\rho_0 N_0^2} Q\rho_n' \mathrm{d}A = \frac{g^2 H}{2\rho_0 N_0^2} \iint_A Q\rho_n'^2 \mathrm{d}A. \tag{4.72}$$

As in the global energy budgets, these terms are always non-negative, making them energy sinks and never sources.

4.4 Summary

To summarise, the total kinetic energy budget is

$$\frac{\mathrm{d}}{\mathrm{d}t} K + W + K_f + C + F_K = 0, \tag{4.73}$$

and the available potential energy budget is

$$\frac{\mathrm{d}}{\mathrm{d}t} A + A_f - C + F_A = 0. \tag{4.74}$$

Assigning

$$P \equiv A + K \tag{4.75}$$

as the total pseudo-energy, and

$$F \equiv F_A + F_K \tag{4.76}$$

as the total rate of change of pesudo-energy due to the relaxation scheme, then we can add the budget equations (4.73) and (4.74) to find the pseudo-energy budget

$$\frac{\mathrm{d}}{\mathrm{d}t} P + W + K_f + A_f + F = 0. \tag{4.77}$$

We interpret this budget to say that the rate of change of pseudo-energy P in a volume V balances with the fluxes through the boundaries W, K_f and A_f, and the rate that

pesudo-energy changes due to forcing. The energy conversion term C does not make an appearance in the pseudo-energy budget as it only represents energy conversion between kinetic and available potential energy.

The modal budget derivations left us with the barotropic kinetic energy budget

$$\frac{\mathrm{d}}{\mathrm{d}t}K_0 + S_0 + W_0 + F_{K_0} = 0, \tag{4.78}$$

the baroclinic kinetic energy budget at mode-n

$$\frac{\mathrm{d}}{\mathrm{d}t}K_n + S_n^u + W_n + C_n + F_{K_n} = 0, \tag{4.79}$$

and the available potential energy budget at mode-n

$$\frac{\mathrm{d}}{\mathrm{d}t}A_n + S_n^\rho - C_n + F_{A_n} = 0. \tag{4.80}$$

If we assign

$$P_n \equiv K_n + A_n \tag{4.81}$$

as the pseudo-energy at mode-n,

$$S_n \equiv S_n^u + S_n^\rho \tag{4.82}$$

as the total sink of pseudo-energy at mode-n, and

$$F_n \equiv F_{K_n} + F_{A_n} \tag{4.83}$$

as the total rate of change of pesudo-energy due to the relaxation scheme at mode-n, then we can add (4.79) and (4.80) to get the pseudo-energy budget at mode-n

$$\frac{\mathrm{d}}{\mathrm{d}t}P_n + S_n + W_n + F_n = 0. \tag{4.84}$$

Relation between budgets

Working term by term, we can sum the barotropic and baroclinic budgets to form the total budgets. The pseudo-energy, work, and forcing term sums are intuitive

$$\frac{\mathrm{d}}{\mathrm{d}t}K_0 + \sum_{n=1}^{\infty}\frac{\mathrm{d}}{\mathrm{d}t}P_n = \frac{\mathrm{d}}{\mathrm{d}t}P, \tag{4.85}$$

$$W_0 + \sum_{n=1}^{\infty} W_n = W, \tag{4.86}$$

$$F_{K_0} + \sum_{n=1}^{\infty} F_n = F. \tag{4.87}$$

The remaining terms are the sinks and nonlinear fluxes, which sum following

$$S_0 + \sum_{n=1}^{\infty} S_n = K_f + A_f. \tag{4.88}$$

4.5 Implementation in MITgcm

The MITgcm can compute an extensive set of diagnostics online, and we extend the capability to compute both the global and modal energy budget terms as follows. First, at $t = kT_S$ (where $T_S = 414$ s is the sampling period and $k \in \mathbb{N}$) we find the coefficients in (4.15) and (4.16) for use in modal budget terms by projecting the model flow fields onto the vertical structure functions,

$$\{\vec{u}_{h_0}, p_0'\} = \frac{1}{H}\int_{-H}^{0}\{\vec{u}_h, p'\}\,\mathrm{d}z, \tag{4.89}$$

$$\{\vec{u}_{h_n}, p_n'\} = \frac{2}{H}\int_{-H}^{0}\{\vec{u}_h, p'\}\cos(m_n z)\,\mathrm{d}z, \tag{4.90}$$

$$\{w_n, \rho_n'\} = \frac{2}{H}\int_{-H}^{0}\{w, \rho'\}\sin(m_n z)\,\mathrm{d}z. \tag{4.91}$$

Next, we compute the integrand of each energy budget term (except the time derivative terms). We pass the integrand to MITgcm's `diagnostic` package which manages the area/volume integration and saves the result, yielding a time series for each energy budget term. We handle the time derivative terms differently: we save a time series of the

differentiated quantities (P, K_0, etc) at $t = kT_S \pm \Delta t$, and compute the time derivative offline using centred second order differences. These online diagnostics consume roughly one quarter of the model runtime. Performing the computations online eliminates the need to save the complete wavefields at high time resolution for offline computation of the energy budget terms.

Chapter 5

Benchmark Case

This chapter describes the benchmark experiments where we verify that the forcing and energy diagnostics are working as desired.

5.1 Experiment Design

These experiments are the benchmark cases where the internal tide forcing at the western boundary forcing is used but no eddy prescribed. Figure 5.1 shows the domain and Table 5.1 shows the chosen parameters. The 120 km radius dashed circle centred at (250, 200) km is the energy analysis region over which the energy budget diagnostics are computed (volume V for the total budgets and area A for the modal budgets). One experiment is conducted at low-latitude and one at mid-latitude, and each used 64 cores on the `gpc` cluster at SciNet for 11.6 hours.

We initialise the model with a quiescent initial state and apply the mode-one internal tide forcing (3.12) to the west boundary, which ramps up over two tidal periods. The generated wave propagates eastward, crossing the energy analysis region, and eventually reaches the east boundary where the sponging region removes it. The relaxation map (via Equation (3.19)) is given by

$$Q\tau_r = \frac{\alpha_0}{1-\alpha_0} = \frac{1}{2}[1 + \tanh(S_1(x - S_2)/L)] \tag{5.1}$$

$$\tag{5.2}$$

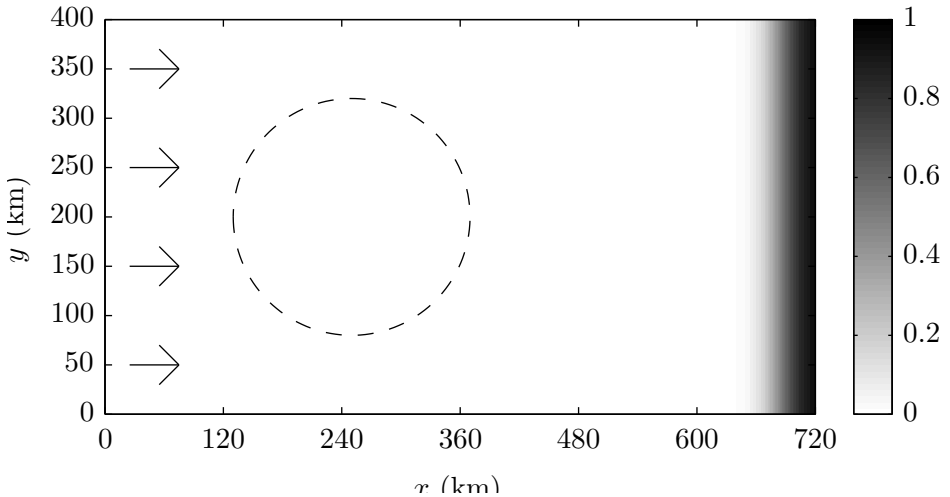

Figure 5.1: The domain used for the benchmark (eddy free) cases. The shaded area indicates $Q\tau_r$, the strength of the sponge region.

where $S_1 = 30$, $S_2 = L - 35$ km, and L is the domain length. These parameters are chosen such that the sponge region ramps up slowly, ensuring that waves are not reflected westward.

5.2 Results

Figure 5.2 shows the tidally averaged time series of the W and $\mathrm{d}\bar{P}/\mathrm{d}t$ terms from the total pseudo-energy budget (4.77). No signal is present until the wave front reaches the

Table 5.1: Parameters used for the benchmark cases.

Parameter	Value
$L_x \times L_y \times H$	720 km × 400 km × 5000 m
$\Delta x \times \Delta y \times \Delta z$	0.5 km × 0.5 km × 100 m
$N_x \times N_y \times N_z$	1440 × 800 × 50
U_t	5 cm/s
Δt	69 s

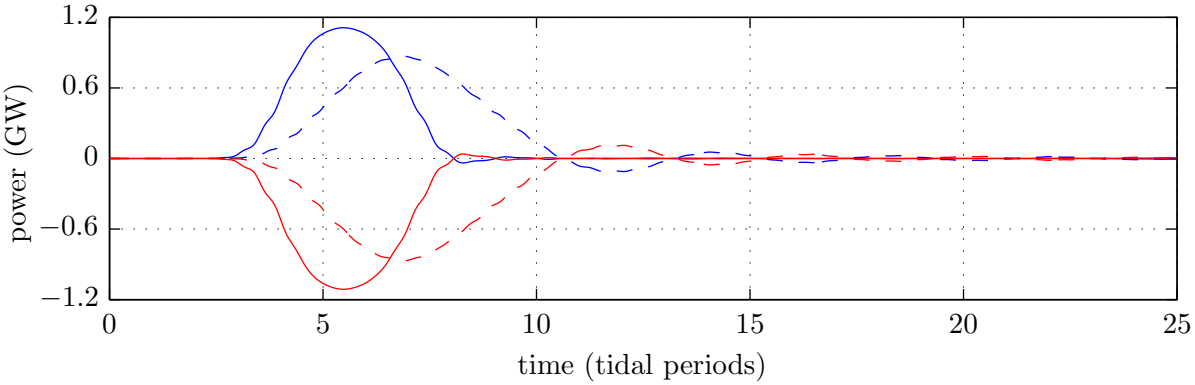

Figure 5.2: The tidally averaged linear terms from the pseudo-energy budget (4.77) where $\bar{W}$ is red and $\mathrm{d}\bar{P}/\mathrm{d}t$ is blue. The low-latitude case is solid and mid-latitude case dashed.

west edge of the energy analysis region at about $t = 3T$. As the wave propagates across, the outward energy flux is negative ($\bar{W} < 0$), approximately balancing the rise in pseudo-energy ($\mathrm{d}\bar{P}/\mathrm{d}t > 0$). Eventually the wave saturates the energy analysis domain, and by $t = 15T$ it has achieved a quasi-steady state. These two terms make up the dominant balance for (4.77), $\mathrm{d}\bar{P}/\mathrm{d}t + \bar{W} \approx 0$.

Figure 5.3 shows the tidally averaged nonlinear flux terms in the total pseudo-energy budget (4.77) and also the first four sink terms from the barotropic and baroclinic budgets (4.78) and (4.84). The vertical scale here is three orders of magnitude smaller than in Figure 5.2. There is a signal present at the mode-one ($\bar{S}_1$) and mode-two ($\bar{S}_2$) sinks, with the low- (mid-) latitude cases showing levels around 0.2 MW (0.1 MW) in quasi-steady state, which is comparable to the nonlinear terms $\bar{K}_f + \bar{A}_f$. The barotropic ($\bar{S}_0$) and mode-three ($\bar{S}_3$) sinks are negligible. The dominant balance for (4.88) is $\bar{K}_f + \bar{A}_f \approx \bar{S}_1 + \bar{S}_2$.

Figure 5.4 shows a snapshot of the projection coefficients u_1 and u_2 at $t = 10T$ with the upper (lower) panel showing the low- (mid-) latitude case. The black curve shows the expected 5 cm/s mode-one signal that spans most of the domain. As the wavelength and group speed depend on the Coriolis parameter f, the black curves differ in both wavelength and propagation extent between the upper and lower panels.

In red (and on a different scale) is a much weaker mode-two signal. The signal for the low-latitude case has two components: a long wavelength part coincident with the mode-one signal that is due to PSI, and a short wavelength part that is due to the crude forcing at the western boundary that corresponds to a wave of twice the tidal frequency.

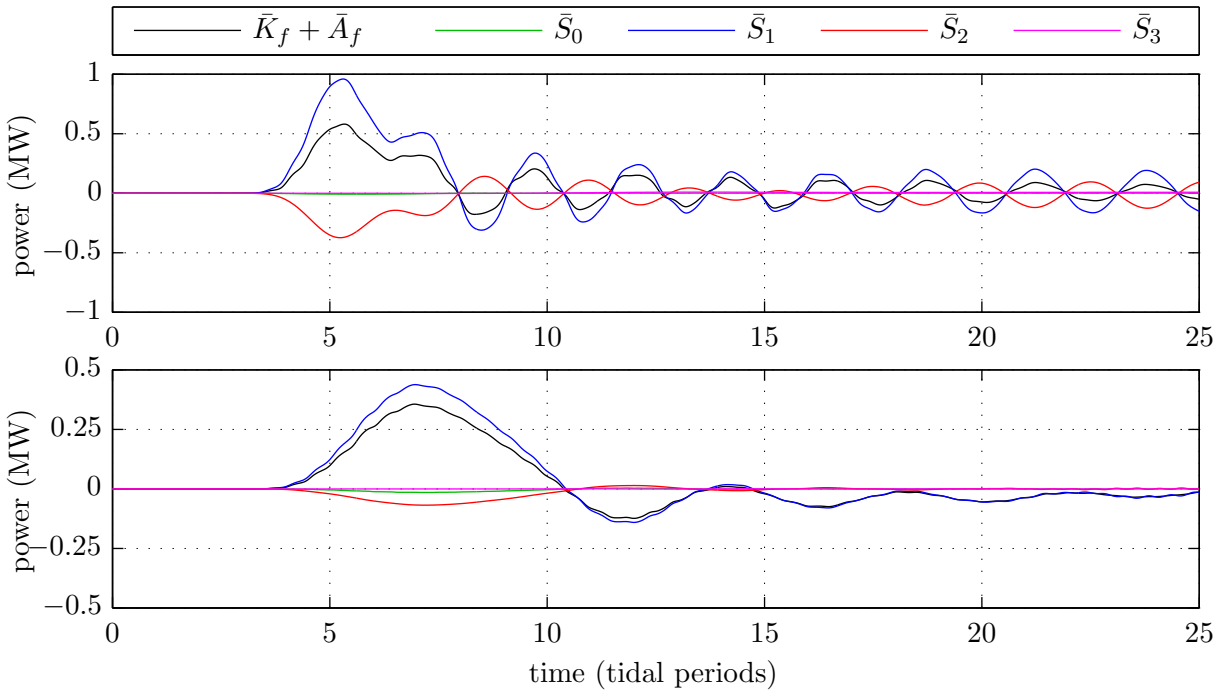

Figure 5.3: The nonlinear terms $\bar{K}_f + \bar{A}_f$ from the pseudo-energy budget (4.77), the barotropic sink $\bar{S}_0$ from the barotropic kinetic energy budget (4.78) and the baroclinic sinks $\bar{S}_1$, $\bar{S}_2$, and $\bar{S}_3$ from the first three baroclinic pseudo-energy budgets (4.84). All terms are tidally averaged.

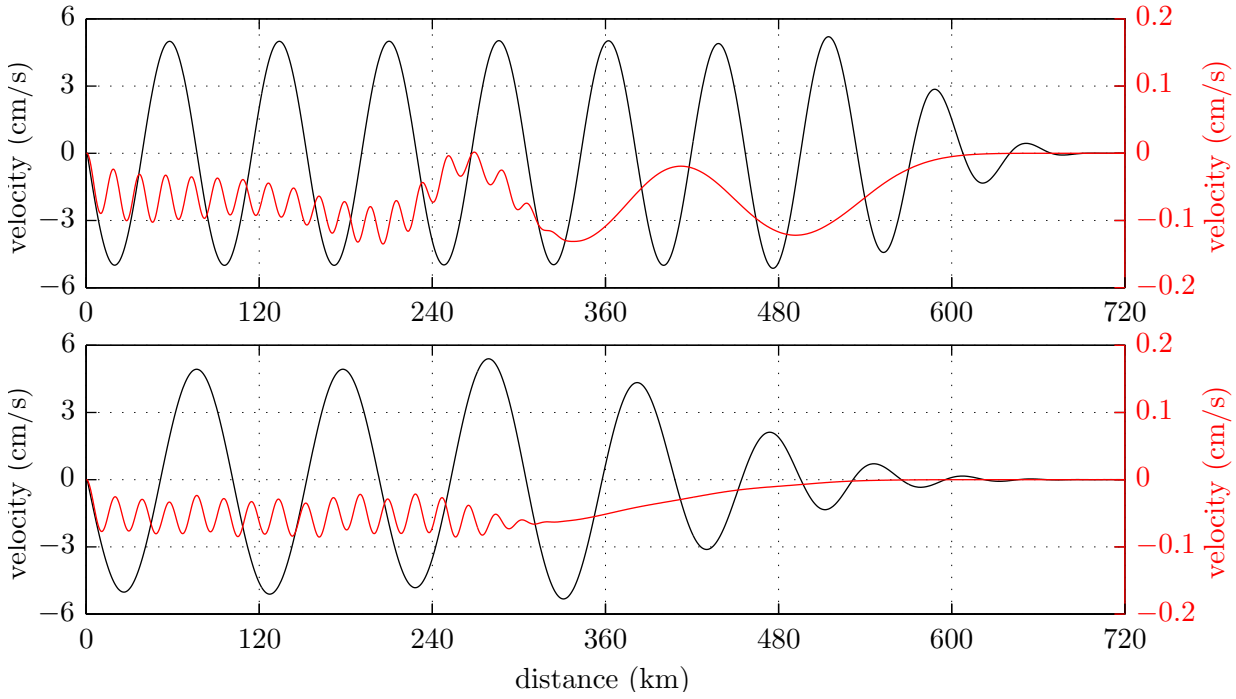

Figure 5.4: Snapshot of the projection coefficients u_1 (black) and u_2 (red) from the benchmark cases at $t = 10T$. The top panel shows the low-latitude case and the bottom panels shows mid-latitude.

The mid-latitude case is similar, however it lacks the large wavelength component, which is expected as the mid-latitude case exceeds the critical latitude above which PSI does not occur. The larger mode-two velocity signal in the low-latitude case is consistent with the larger mode-two sink signal in Figure 5.3. The mode-two signal has a non-zero mean produced by mode-one self interaction, particularly radiation stress convergence, in the wave front where the mode-one amplitude increases.

The tidally averaged eastward energy flux is 4.78 and 3.68 kW/m for the low- and mid-latitude cases.

This chapter showed that the forcing and diagnostics function as designed. Further, we have measured the sink terms for the eddy-free case. These terms provide a baseline estimate of inter-mode scattering in the absence of an eddy; we shall contrast them with cases that include an eddy in the next two chapters.

Chapter 6

Barotropic Eddy

In this chapter we examine the interaction of an internal tide field with barotropic eddies.

6.1 Experiment Design

In these experiments, we prescribe a barotropic eddy ($\Phi(z) = 1$) and permit it to adjust for five tidal periods ($0 \leq t \leq 5T$, where $T = 44712$ s $= 12.42$ hr). During this adjustment process, the relaxation scheme (Martinsen and Engedahl, 1987) is activated surrounding the eddy to damp out emitted waves as shown in the left panel of Figure 6.1. A small adjustment takes place resulting from numerical discretisation errors in the eddy initialisation. The initial eddy is otherwise an exact solution of the model's equations of motion.

Once the adjustment period is complete, the relaxation scheme is moved to only the east boundary as shown in the right panel of Figure 6.1. At this time the western boundary forcing is switched on, and ramps up over $5T \leq t \leq 7T$. Table 6.1 shows the eddy position and domain parameters. The energy analysis is performed over the same 120 km radius circle as in the benchmark experiments, centred at (x_c, y_c). We conduct a suite of barotropic eddy cases, varying the eddy size L_E and velocity magnitude U_E as shown in Table 6.2. These simulations used 64 cores on the `gpc` cluster at SciNet where the mean runtime was 20.5 hours.

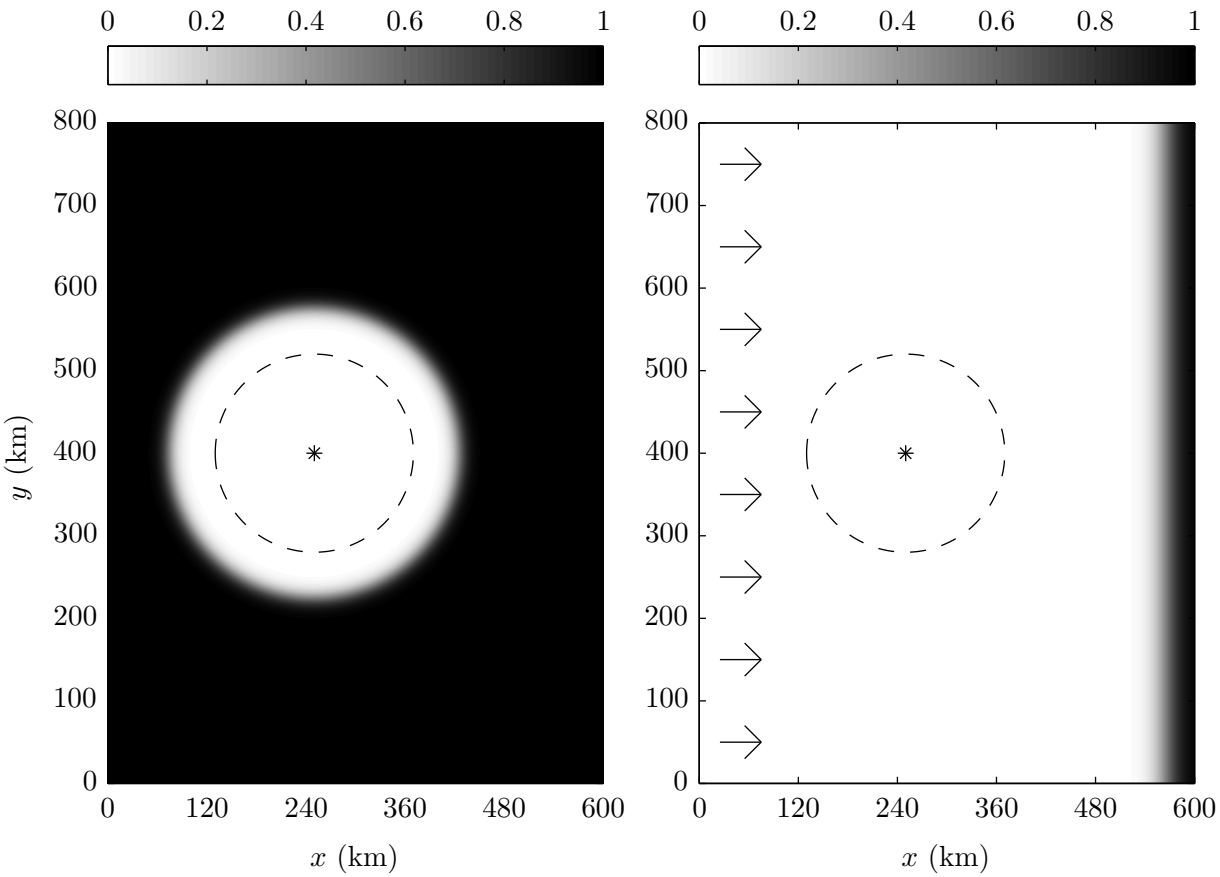

Figure 6.1: The domain used for the barotropic eddy cases during (left) the adjustment phase and (right) the forced phase. The black regions are restored to no flow by the relaxation scheme, the asterisk denotes the centre of the eddy, the arrows show the propagation direction of the forced wave, and the circle shows the energy analysis domain.

Table 6.1: Parameters used for the barotropic eddy cases.

Parameter	Value
$L_x \times L_y \times H$	600 km $\times$ 800 km $\times$ 5000 m
$\Delta x \times \Delta y \times \Delta z$	0.5 km $\times$ 0.5 km $\times$ 200 m
$N_x \times N_y \times N_z$	$1200 \times 1600 \times 25$
(x_c, y_c)	(250, 400) km
U_t	5 cm/s
Δt	69 s

Table 6.2: The parameters varied in this set of experiments. The table entries are the vortex Rossby number (2.50) for the low-latitude cases. The mid-latitude values are one half of these values.

	L_E (km)			
U_E (cm/s)	20	30	40	50
30		0.42		
45	0.94	0.62	0.47	0.37
60		0.83		
75		1.04		
90		1.25		

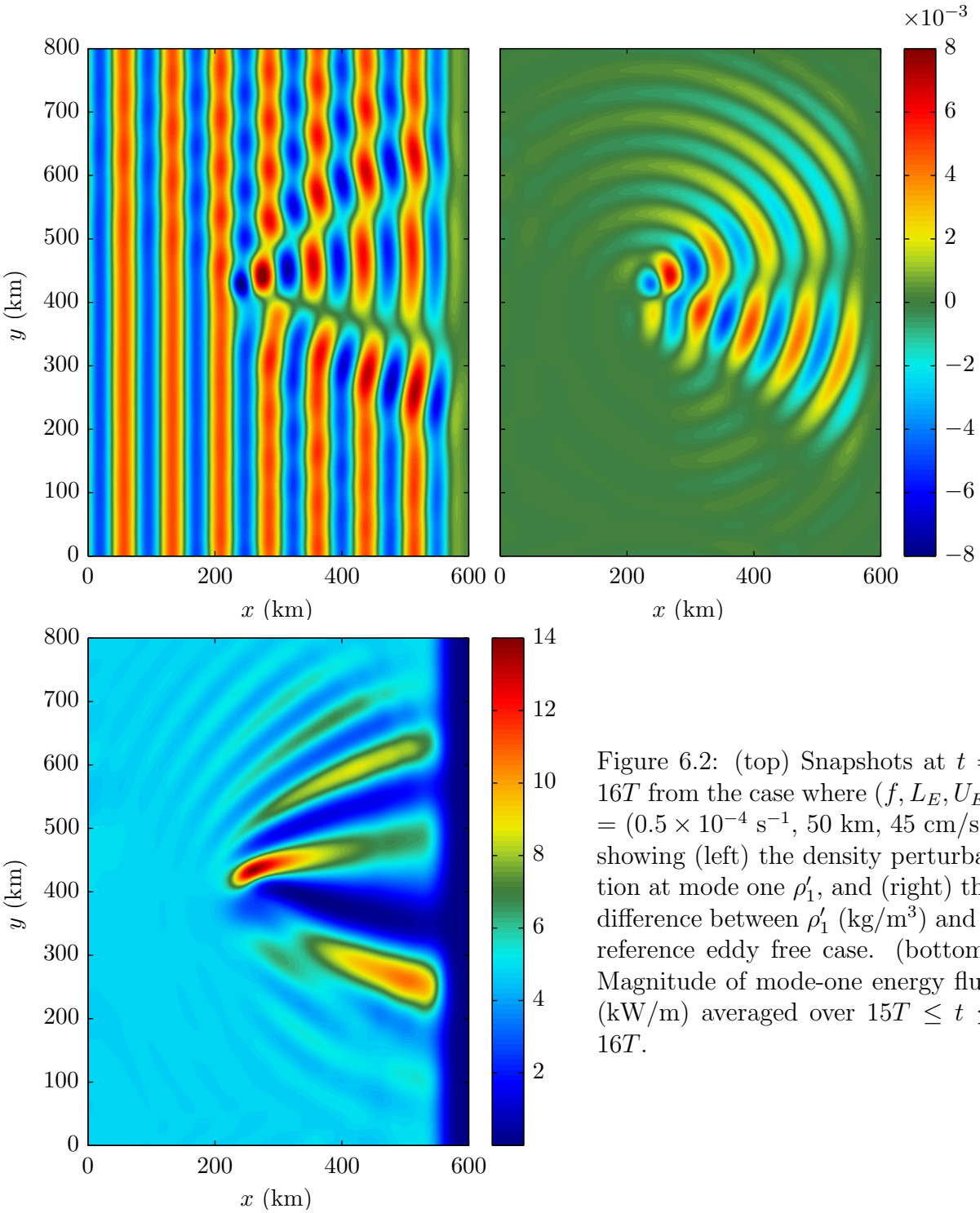

Figure 6.2: (top) Snapshots at $t = 16T$ from the case where $(f, L_E, U_E) = (0.5 \times 10^{-4}\ \mathrm{s}^{-1}, 50\ \mathrm{km}, 45\ \mathrm{cm/s})$, showing (left) the density perturbation at mode one ρ_1', and (right) the difference between ρ_1' (kg/m^3) and a reference eddy free case. (bottom) Magnitude of mode-one energy flux (kW/m) averaged over $15T \leq t \leq 16T$.

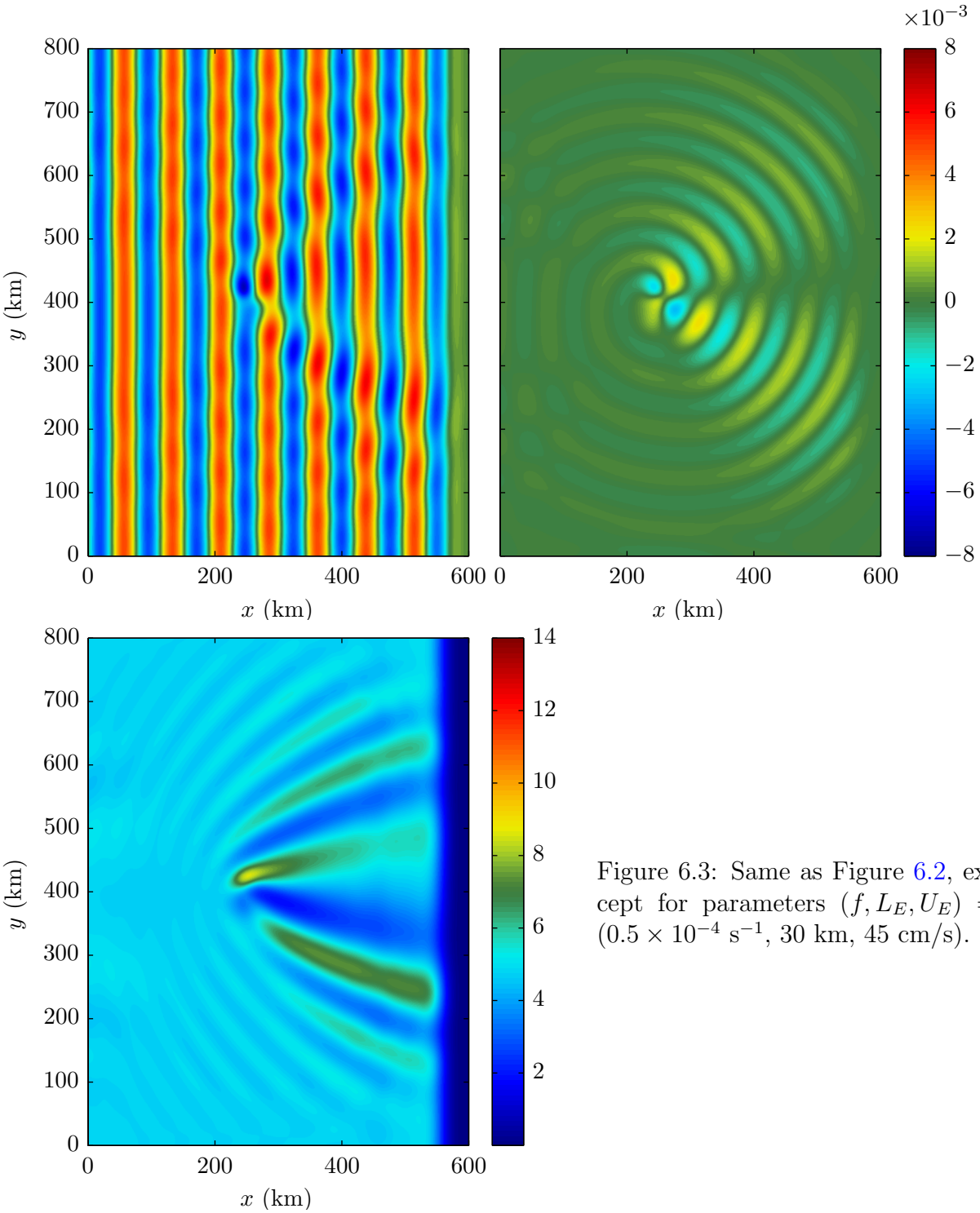

Figure 6.3: Same as Figure 6.2, except for parameters $(f, L_E, U_E) = (0.5 \times 10^{-4}\ \mathrm{s}^{-1}, 30\ \mathrm{km}, 45\ \mathrm{cm/s})$.

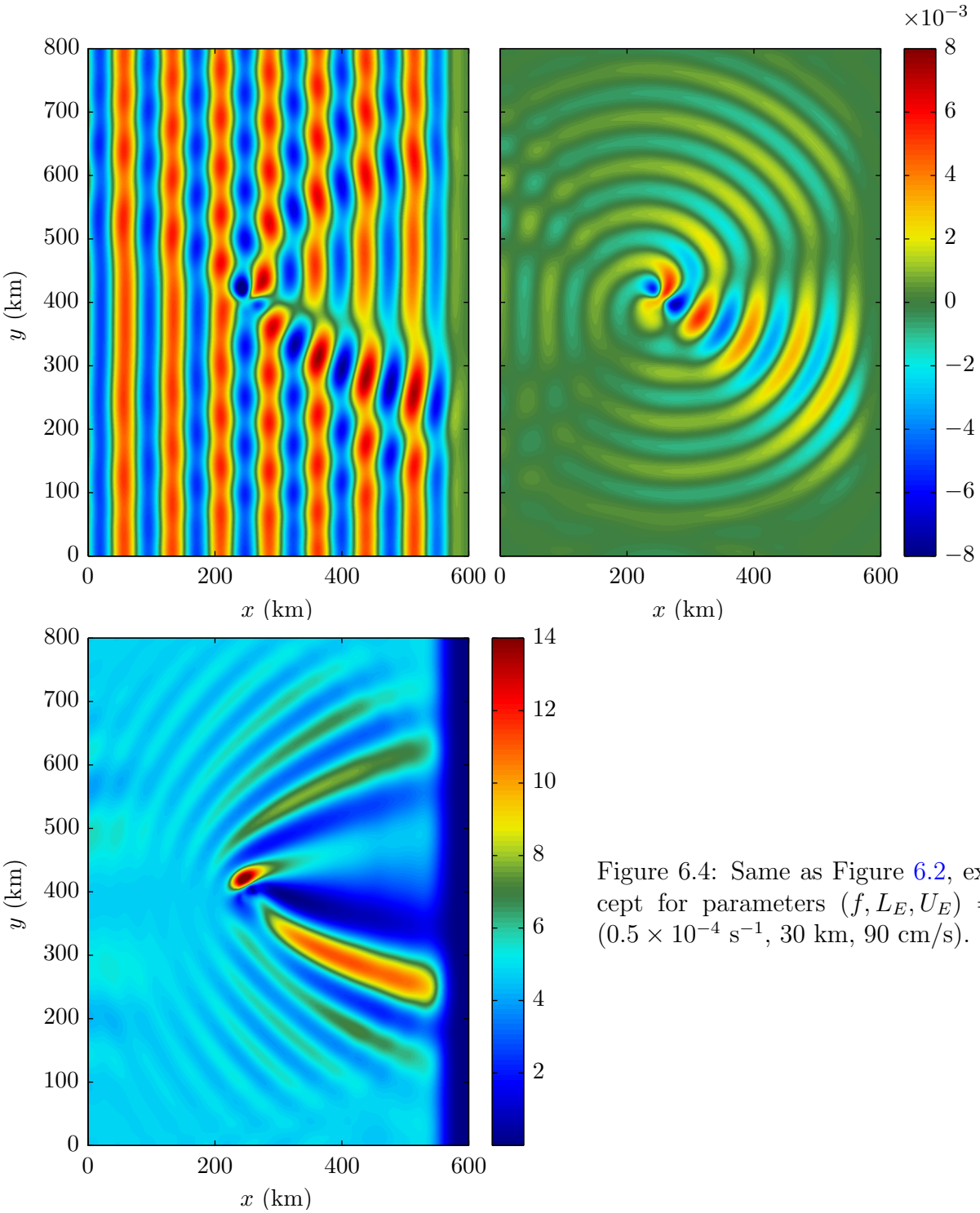

Figure 6.4: Same as Figure 6.2, except for parameters $(f, L_E, U_E) = (0.5 \times 10^{-4}\ \mathrm{s}^{-1}, 30\ \mathrm{km}, 90\ \mathrm{cm/s})$.

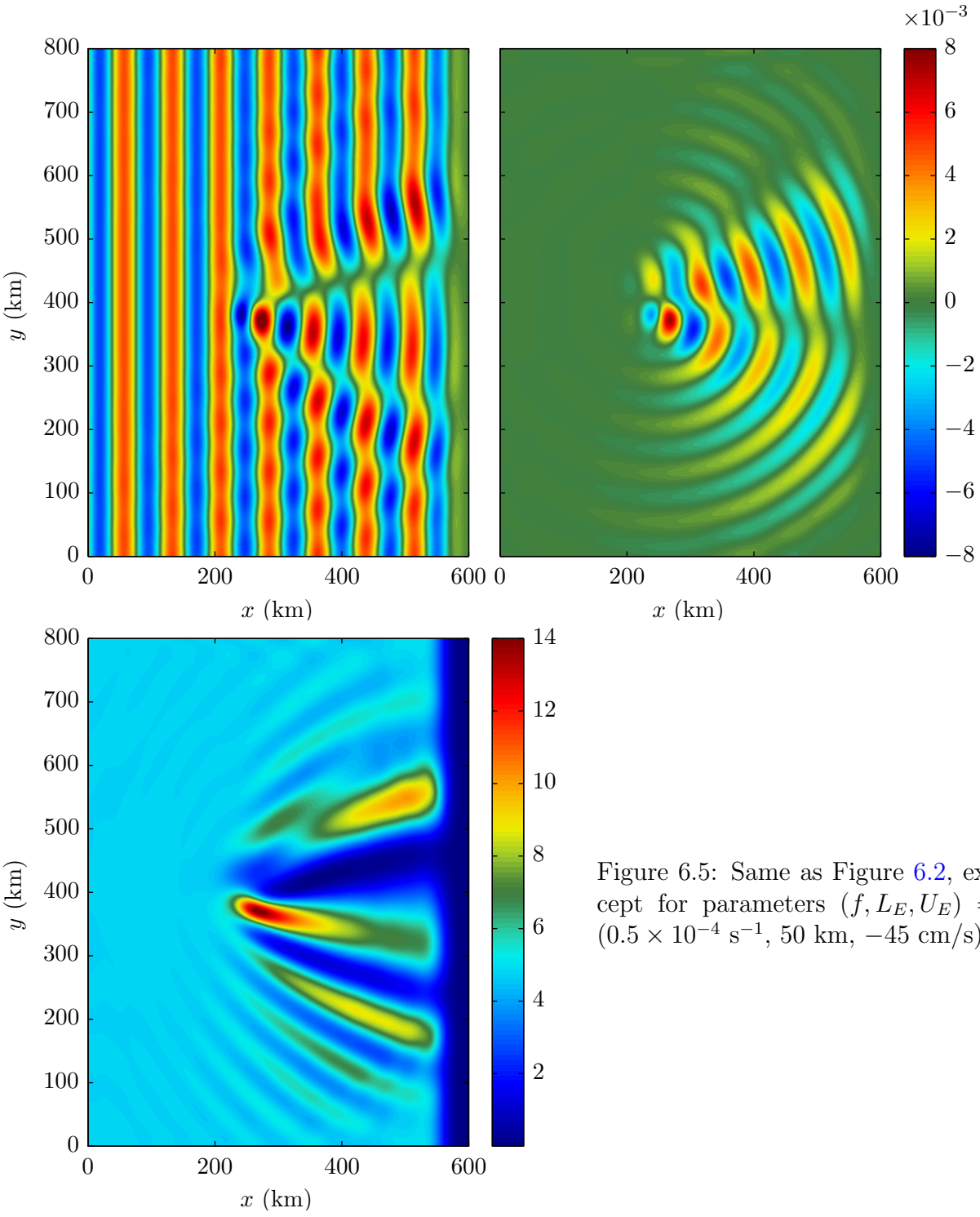

Figure 6.5: Same as Figure 6.2, except for parameters $(f, L_E, U_E) = (0.5 \times 10^{-4}\ \mathrm{s}^{-1}, 50\ \mathrm{km}, -45\ \mathrm{cm/s})$.

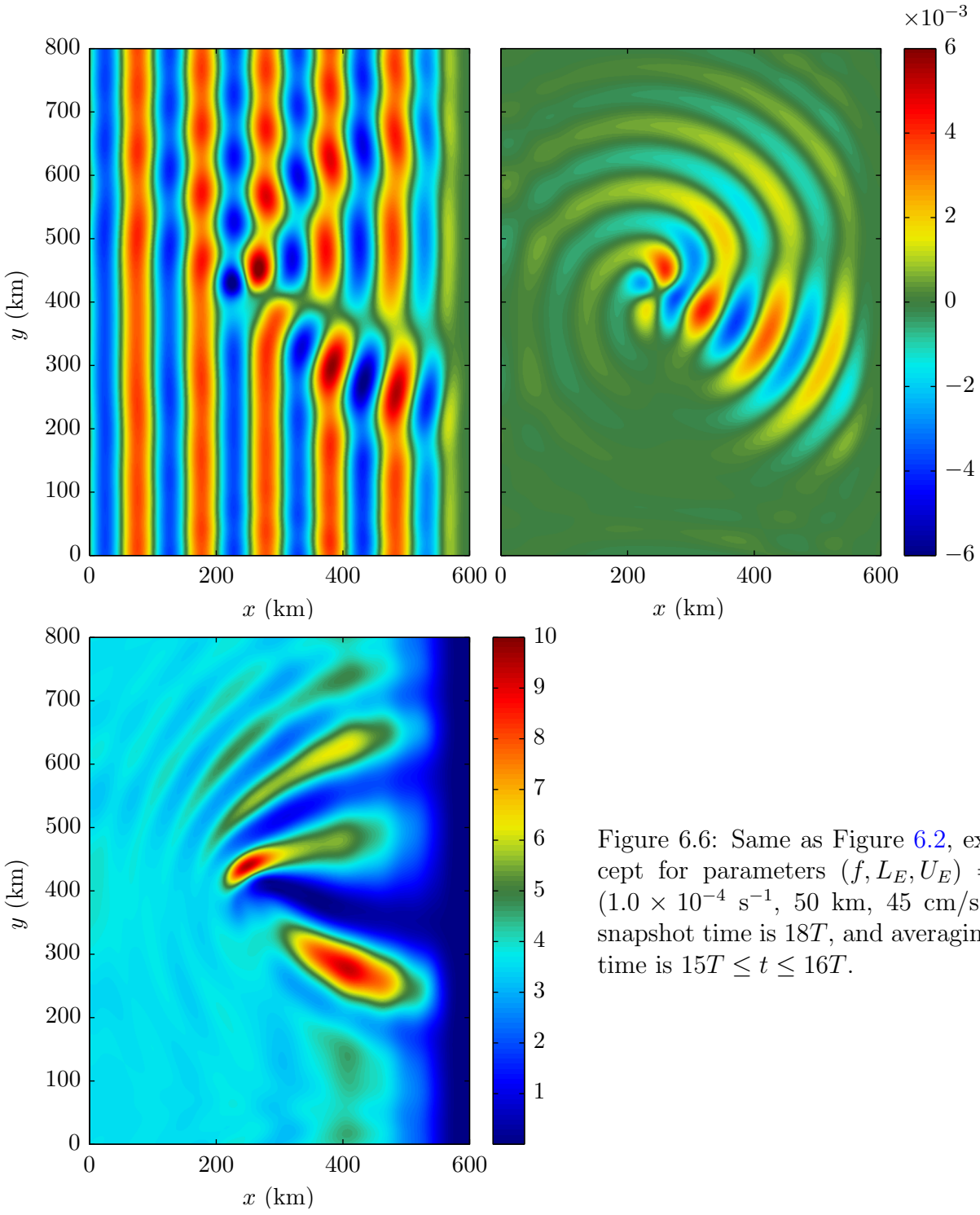

Figure 6.6: Same as Figure 6.2, except for parameters $(f, L_E, U_E) = (1.0 \times 10^{-4}\ \text{s}^{-1},\ 50\ \text{km},\ 45\ \text{cm/s})$, snapshot time is $18T$, and averaging time is $15T \leq t \leq 16T$.

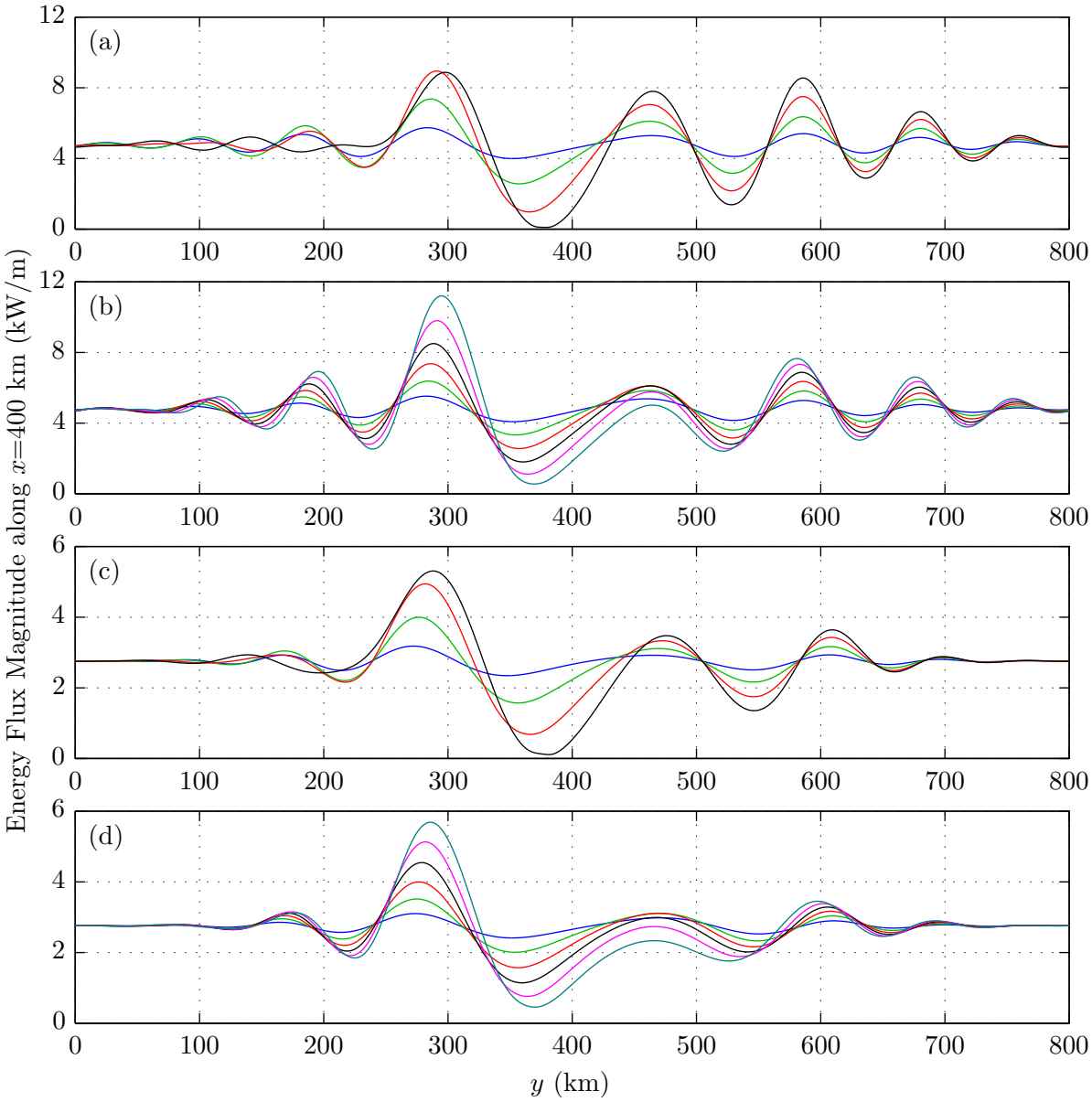

Figure 6.7: (a) $f = 0.5 \times 10^{-4}$ s^{-1}, $U_E = 45$ cm/s, $L_E = 20$ km (blue), 30 km (green), 40 km (red) and 50 km (black). (b) $f = 0.5 \times 10^{-4}$ s^{-1}, $L_E = 30$ km, $U_E = 15$ cm/s (blue), 30 cm/s (green), 45 cm/s (red), 60 cm/s (black), 75 cm/s (magenta) and 90 cm/s (cyan). (c) and (d) are the same as (a) and (b) but for $f = 1.0 \times 10^{-4}$ s^{-1}.

6.2 Results

Figure 6.2 shows three visualisations of the modified mode-one internal tide field after interacting with a barotropic eddy with parameters $(f, L_E, U_E) = (0.5 \times 10^{-4}\ \text{s}^{-1}, 50\ \text{km}, 45\ \text{cm/s})$. The first is the density perturbation at mode-one, ρ_1', and the second is the difference in ρ_1' between the eddy case and a reference eddy-free case. Both snapshots are taken at $t = 16T$. The third uses the modal energy flux magnitude,

$$E_n(x, y) = |p_n' \vec{u}_n| = \sqrt{p_n'^2 (u_n^2 + v_n^2)}, \tag{6.1}$$

where the mode-one energy flux magnitude, $E_1(x, y)$, has been averaged over $15T \leq t \leq 16T$.

From the mode-one density perturbation, we see that the density field is distorted by a barotropic eddy, and the strongest distortion is localised to the east and north of the eddy. Some parts of the density perturbation have been enhanced, while others are diminished. The density difference signal shows a well defined beam emanating from the eddy centre travelling roughly east-southeast, and weaker but wider beam travelling roughly northeast. These beams have a wavelength matching the forced mode-one wavelength of 76.1 km and a magnitude of $\approx 0.006\ \text{kg/m}^3$, which is comparable to that of the reference mode-one density signal of $\approx 0.008\ \text{kg/m}^3$. Barotropic eddies with the chosen parameters have an order-one effect on the internal tide.

An inspection of the energy flux plot shows that hot and cold beams of energy flux have been produced and are superimposed on the incoming energy flux of 4.78 kW/m. The area where the beams are present is roughly coincident with the area where the difference signal is present. The region of no energy flux along the east boundary is due to the relaxation scheme. The variation in energy flux about the incoming energy flux is of the same order of magnitude as the incoming level itself, further supporting that barotropic eddies have order-one effects on the internal tide.

In Figure 6.3 we show the same plots for a smaller eddy with $L_E = 30$ km, and see that the density distortion, density difference signal, and hot and cold spots have all been reduced in magnitude. In Figure 6.4 we see that raising the eddy velocity has effect of increasing the magnitude and extent of the distortion, difference, and hot/cold spot production.

In a similar vein, changing to an anticyclonic (negative U_E) eddy simply has the effect of mirroring the fields about $y = 400$ km as shown in Figure 6.5. Lastly, increasing f to $1.0 \times 10^{-4}\ \text{s}^{-1}$ in Figure 6.6 shows a similar picture as at low-latitude; the order-one effect

persists at faster rotation. We use a later time for illustration in this case because the mode-one waves propagate slower at higher f.

Figure 6.7 shows the same averaged energy flux magnitude evaluated along $x = 400$ km and plotted as a function of y, for each of the low-latitude cases of Table 6.2. In the first panel we vary the eddy length scale L_E and vary the strength of the eddy U_E in the second panel. The third and fourth panel show the same curves for the mid latitude case.

From these plots we see that increasing the eddy size and eddy velocity both have the effect of intensifying the hot and cold spots. The position of the beams (as inferred from the local maxima of the curves) move slightly. Most striking is that the energy flux is reduced to nearly zero in some cold spots (black lines of the first and third panels), and also enhanced to more than double the incident flux in some hot spots (cyan line, second panel). The effect at mid-latitude resembles that observed at low-latitude.

Finally, a look at the sink terms from the energy budgets shows that $\bar{S}_0$ through $\bar{S}_3$ are similar to those obtained in the forcing only case (Figure 5.3), indicating that the barotropic eddy does not efficiently scatter internal tide energy between vertical modes (not shown here).

Chapter 7

Baroclinic Eddy

This chapter looks at the effects that a mesoscale baroclinic eddy has on an internal tide field. The first section describes a set of experiments conducted, followed by a section that details the results. Following this is a verification experiment designed to confirm one of the main results.

7.1 Experiment Design

These experiments use a mode-one baroclinic eddy with $\Phi(z) = \cos(\pi z/H)$ and the same adjustment followed by forcing schedule as in the barotropic eddy chapter. The domain size is different (see Figure 7.1), Table 7.1 lists the chosen parameters, and Table 7.2 lists the suite of cases which vary the values of L_E and U_E. The simulations in this chapter used 64 cores on the `gpc` cluster at SciNet where the mean runtime was about 12.5 hours.

7.2 Results

For the baroclinic eddy cases we illustrate the results with the case $(f, L_E, U_E) = (0.5\times10^{-4}$ s^{-1}, 35 km, 45 cm/s) in Figure 7.2. The top row shows snapshots of the density perturbation at modes two and three taken at $t = 15T$. At the bottom is the modal energy flux magnitude (6.1) for $n = 2, 3$, averaged over $14T \le t \le 15T$.

The plots depict the production of higher mode internal tide beams which emanate from the eddy centre. At mode two the beam-like packets are about five wavelengths long and

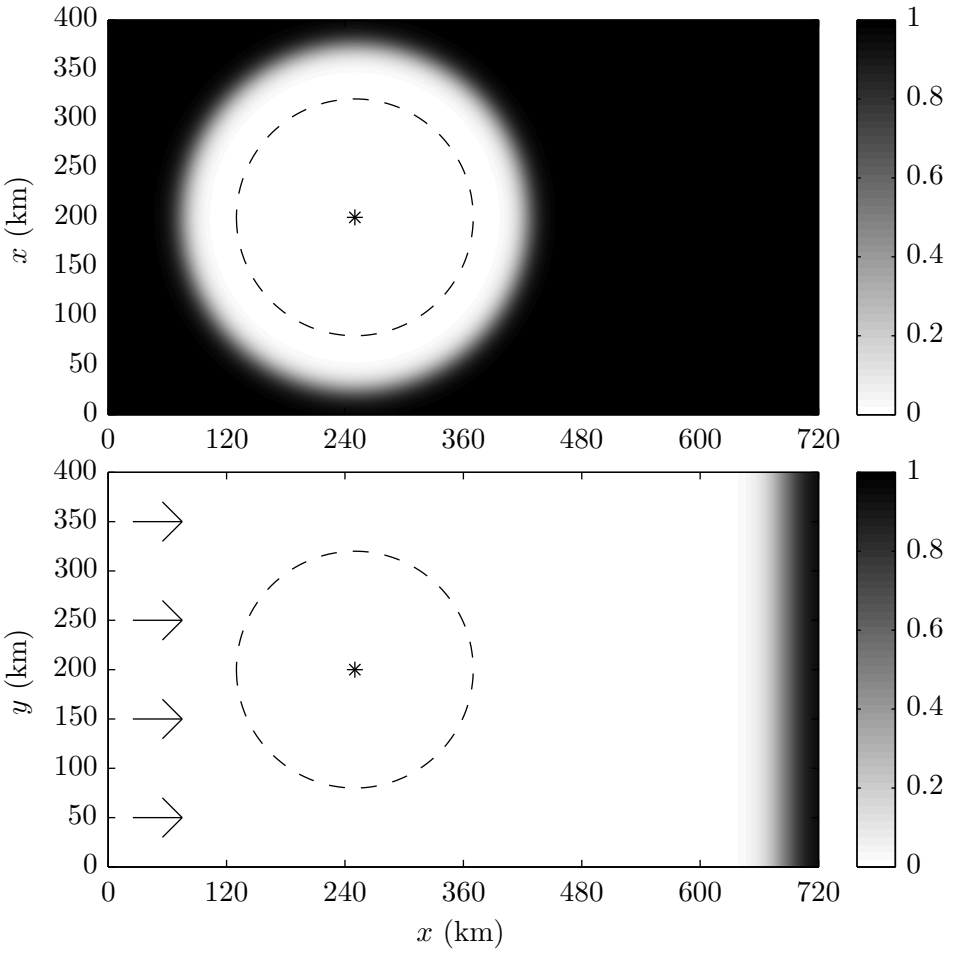

Figure 7.1: The domain used for the baroclinic eddy cases during (top) the adjustment phase and (bottom) the forced phase.

Table 7.1: The domain parameters used for the baroclinic eddy cases.

Parameter	Value
$L_x \times L_y \times H$	720 km $\times$ 400 km $\times$ 5000 m
$\Delta x \times \Delta y \times \Delta z$	0.5 km $\times$ 0.5 km $\times$ 100 m
$N_x \times N_y \times N_z$	$1440 \times 800 \times 50$
(x_c, y_c)	(250, 200) km
U_t	5 cm/s
Δt	69 s

Table 7.2: The parameter values used in this set of experiments. The table entries are the vortex Rossby number (2.50) for the low-latitude case. Mid-latitude values are half of the listed value.

	L_E (km)								
U_E (cm/s)	15	20	25	30	35	40	45	50	55
30	0.83	0.62	0.50	0.42	0.36	0.31	0.28	0.25	0.23
45		0.94	0.75	0.62	0.53	0.47	0.42	0.37	0.34
60				0.83	0.71	0.62	0.55	0.50	0.45

is strongest in magnitude in two main beams, although the signal is present at all angles about the eddy. One beam travels roughly east-northeast and the other east-southeast. Between the beams is a phase shift of roughly π. There is weak signal visible to the west of the eddy (faint vertical lines) corresponding to the weak mode-two signal of Figure 5.4. The magnitude of the produced beams swamps the weak signal to the east of the eddy.

The energy flux signal highlights the beams where the energy flux is most concentrated, also revealing that the east-southeast beam is somewhat stronger in magnitude than the east-northeast beam. Radial spreading reduces the amplitude of the beams as they get further from the eddy centre.

Three beams are produced at mode three: one travels roughly north-northeast, one south-southeast and one due east. The eastward beam has the largest amplitude, and the south-southeast beam is somewhat stronger than the north-northeast beam. Similarly, a phase shift of roughly π is present between the due-east beam and the other two beams.

In Figure 7.3 we show the same mode two and three density plots for the cases where $U_E = -45$ cm/s at the top and $f = -0.5 \times 10^{-4}$ s^{-1} at the bottom. Switching the sign of the velocity results in a phase shift of π in the mode-two beams but maintains the asymmetry in mode-two beam strength and maintains the mode-three phase. The energy flux magnitude plots remain the same (not shown). Switching the sign of the rotation mirrors the plots about $y = 200$ km.

Figure 7.4 shows the same plots as Figure 7.2 except for modes four and five. At mode four, two main beams are formed propagating in roughly the same directions as those at mode two, including the magnitude asymmetry that favours the south side. A very weak third beam is found propagating roughly south. The mode-five picture is similar to mode-three: a primary due-east beam and weaker side beams. The magnitudes in both density and energy flux are considerably weaker at modes four and five than that seen at modes two and three.

Figure 7.5 shows the averaged mode-two energy flux normal to an 80 km radius circle centred at the eddy for the cases where $L_E = 35$ km ($\theta = 0$ is due east) with low latitude at the top and mid latitude at the bottom. The curves show that increasing the eddy velocity has the effect of increasing the energy flux, and also that the east-southeast beam is consistently stronger in magnitude than the east-northeast beam. We also note that the angle of propagation at mid latitude is higher than for low-latitude. The same plot for the other values of L_E are similar (not shown).

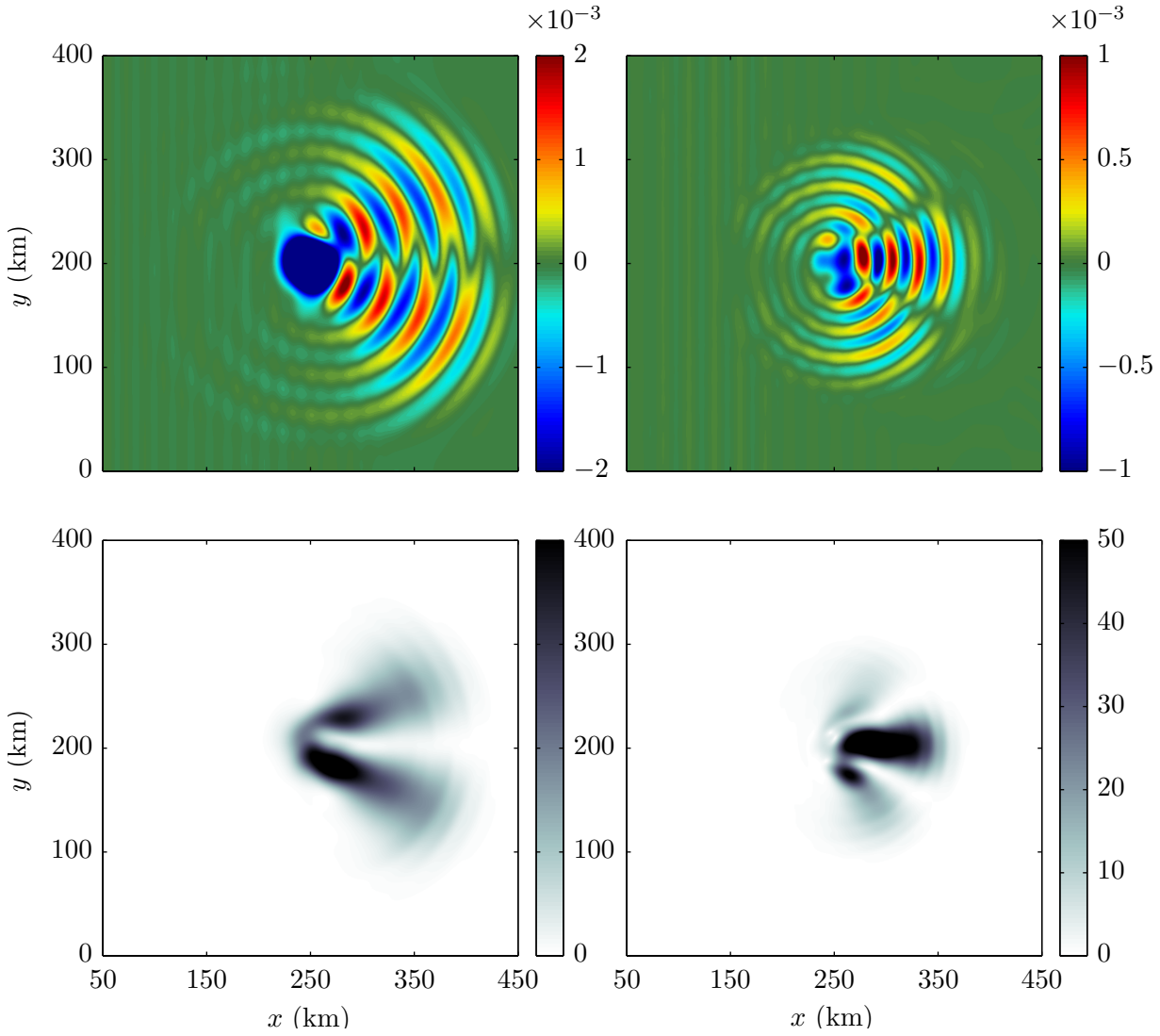

Figure 7.2: (top) Snapshots at $t = 15T$ for the case $(f, L_E, U_E) = (0.5 \times 10^{-4}\ \mathrm{s}^{-1}, 35\ \mathrm{km}, 45\ \mathrm{cm/s})$, showing density perturbation at mode two (left) and three (right). (bottom) Magnitude of energy flux at mode two (left) and mode three (right) averaged over $14T \leq t \leq 15T$.

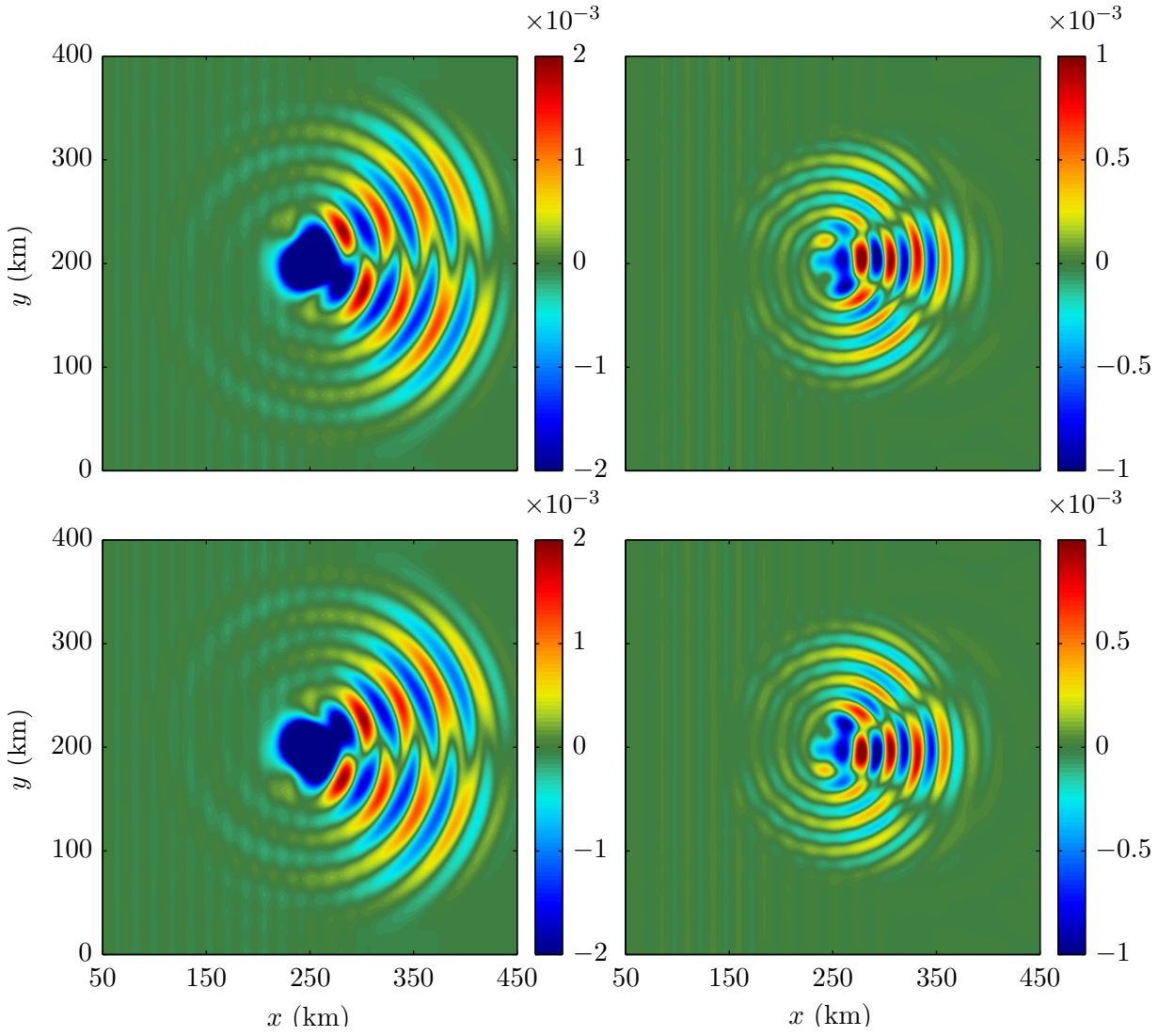

Figure 7.3: Same as the top row of Figure 7.2 except (top) $U_E = -45$ cm/s, and (bottom) $f = -0.5 \times 10^{-4}$ s^{-1}.

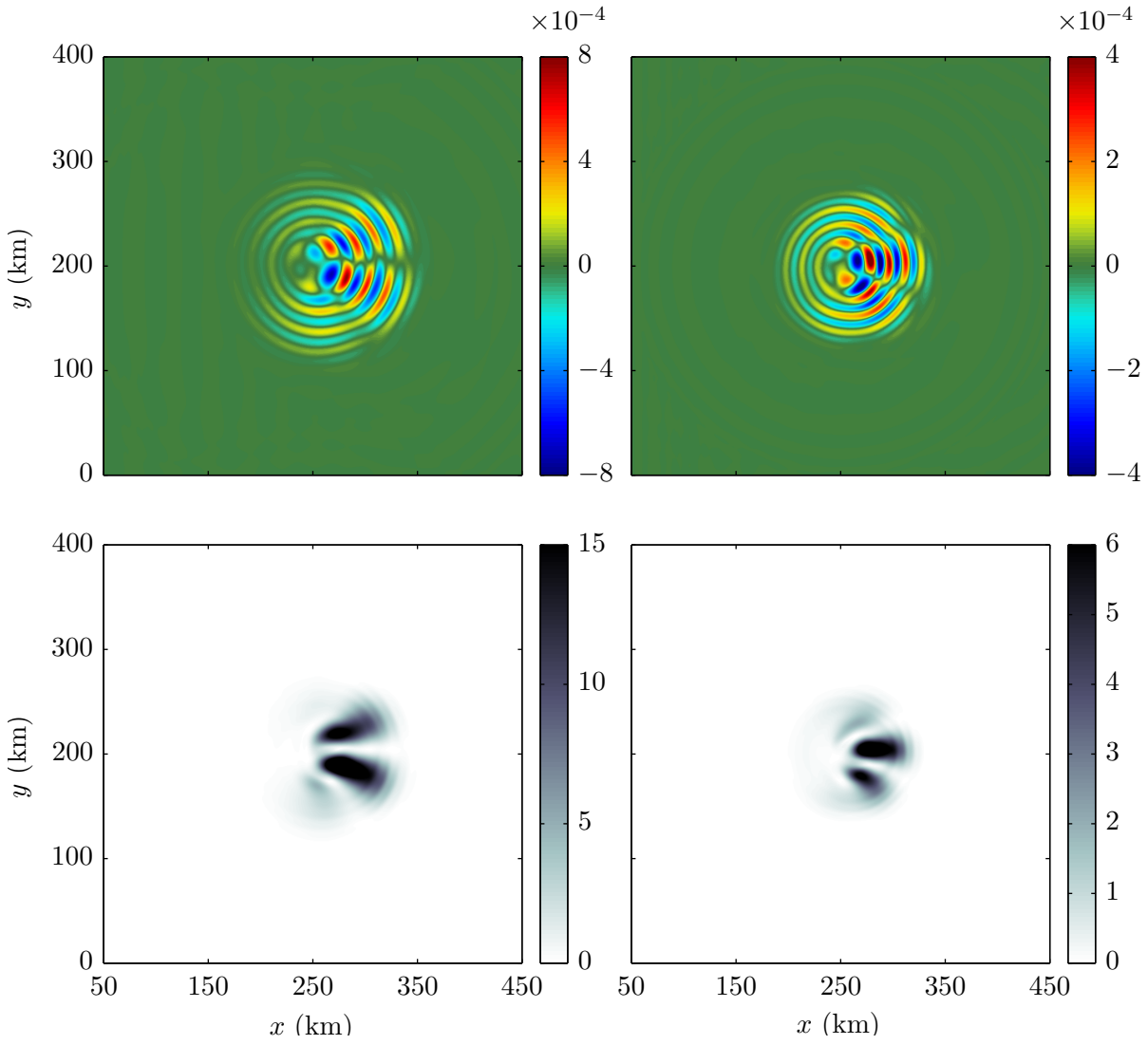

Figure 7.4: Same as Figure 7.2 except (left) mode-four and (right) mode-five.

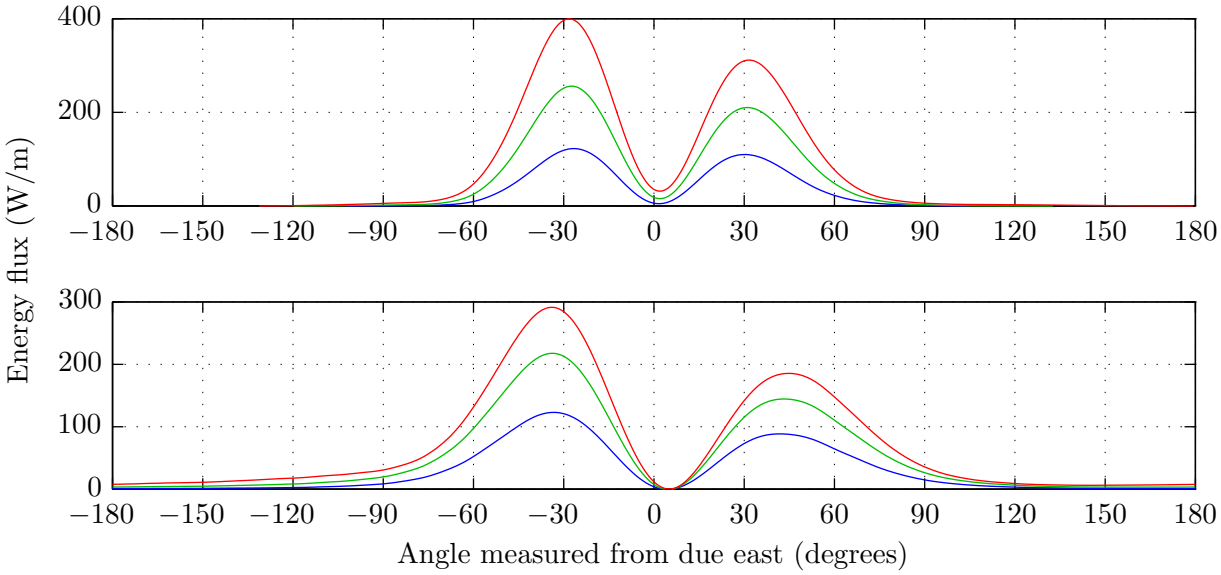

Figure 7.5: Energy flux magnitude at mode two (averaged over $14T \leq t \leq 15T$) normal to an 80 km radius circle as a function of angle, where due east is zero. Top shows low latitude and bottom shows mid latitude. The eddy length scale L_E is 35 km and the eddy velocity U_E is (blue) 30 cm/s, (green) 45 cm/s, and (red) 60 cm/s.

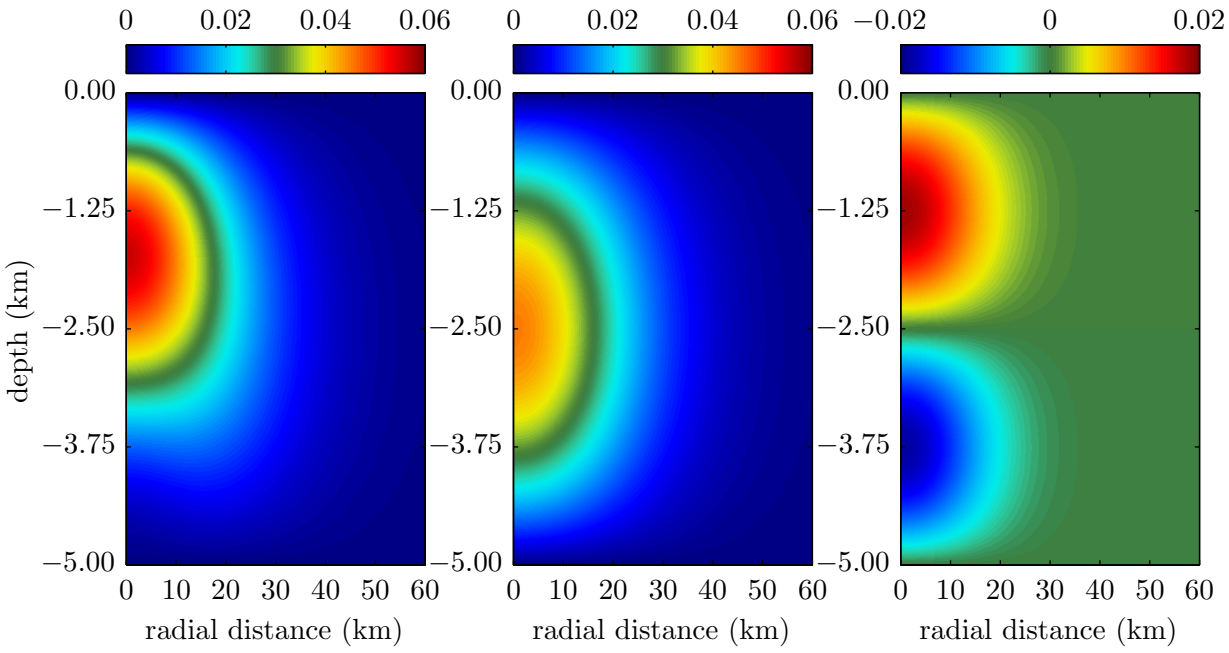

Figure 7.6: Cross section of density perturbation for the illustrative eddy. (left) total density perturbation, (middle) mode one component, (right) mode two component.

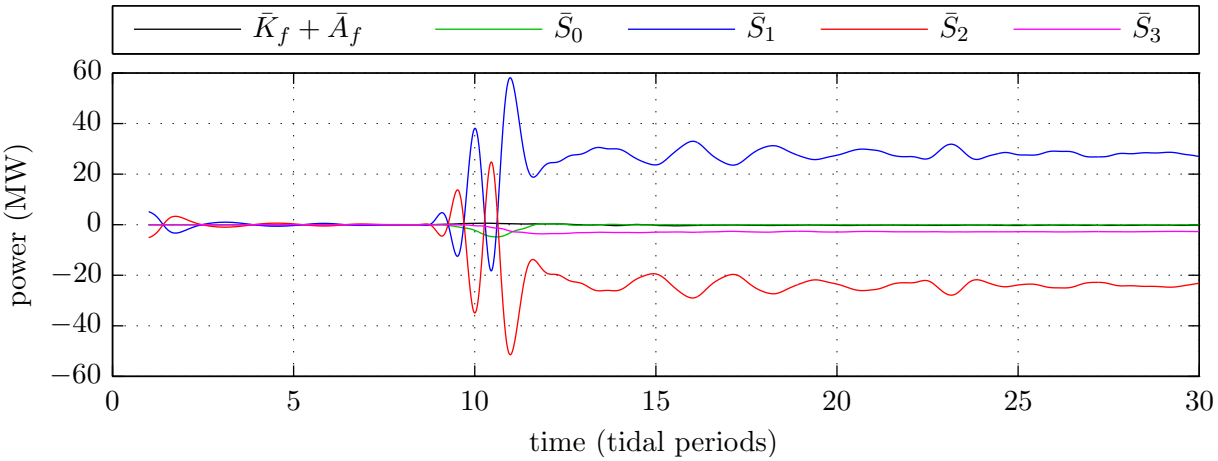

Figure 7.7: Same as Figure 5.3 except for the illustrative baroclinic eddy case.

7.2.1 Beam Asymmetry

The prescribed eddy velocities follow a mode-one vertical profile, however the corresponding density perturbation profile is asymmetric about mid-depth, as shown in Figure 7.6. The cyclo-geostrophic balance equation is used in computing the eddy's density profile, which has a mode-one component which balances the Coriolis term, and a mode-two component that balances the nonlinear term. This asymmetry is the likely explanation for the asymmetry in the generated north and south beams at mode-two.

The sign of the mode-one component of the density perturbation switches when switching the sign of U_E. However, the cyclostrophic term is quadratic in U_E, thus the mode-two density component is not affected by the sign change. The preservation of mode-two beam asymmetry with $U_E = -45$ cm/s as shown in Figure 7.3 is consistent with this explanation.

Further, the vortex Rossby number (2.50) is the ratio of the cyclostrophic term to geostrophic term at $r{=}r_{\max}$. The value of this parameter for the cases shown in Figure 7.5 are (0.36, 0.53, 0.71) at low latitude and (0.72, 1.06, 1.41) at mid latitude. The asymmetry of the beams increases with this parameter, further supporting the cyclostrophic explanation for the asymmetry.

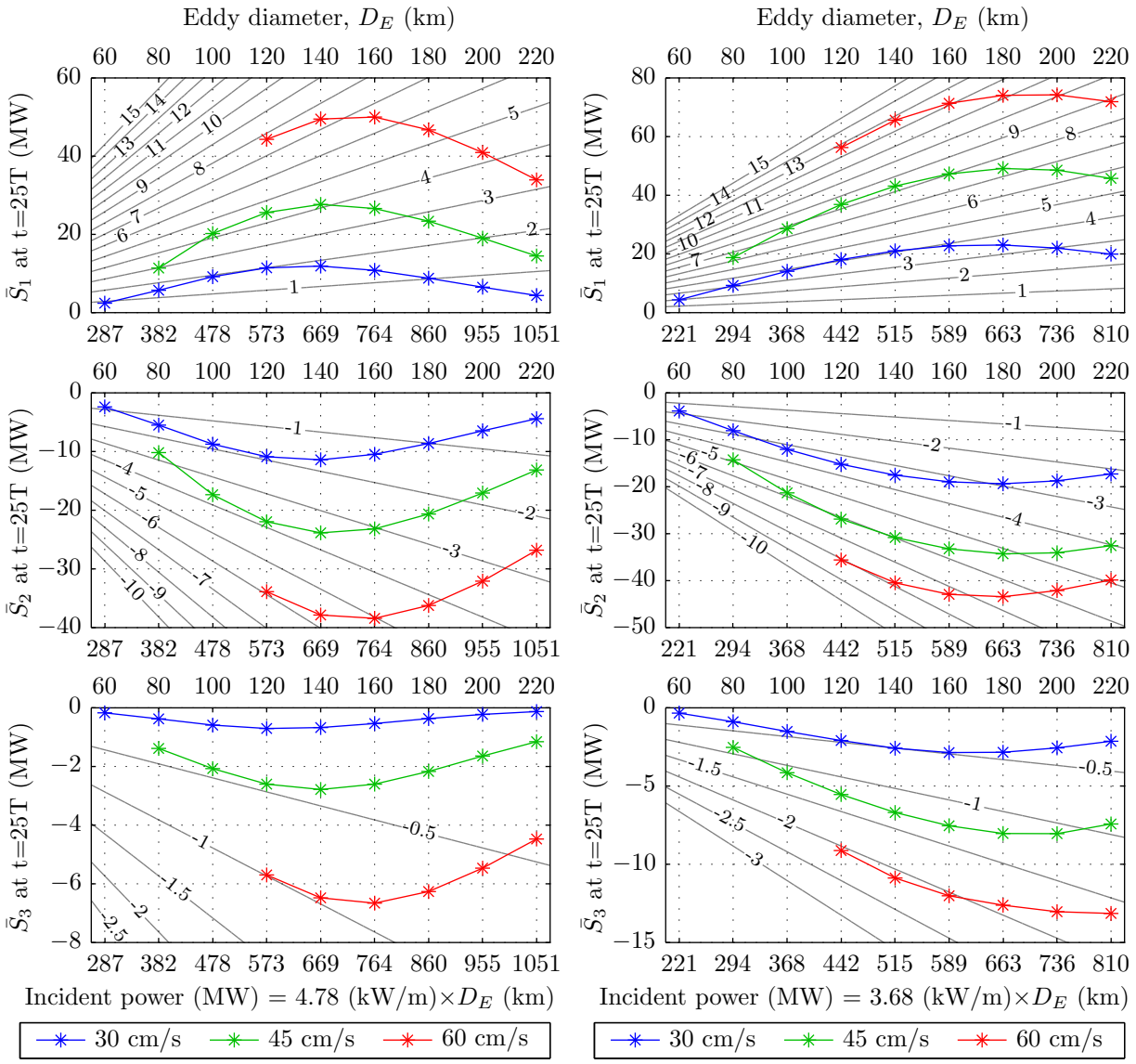

Figure 7.8: Quasi-steady state sink term at mode-one (top), mode-two (middle) and mode-three (bottom) for the (left column) low-latitude cases and (right column) mid-latitude cases. The upper axis is eddy diameter ($D_E = 4L_E$) and the lower axis is power incident to the eddy. The data points are $\bar{S}_n$ evaluated at $t = 25T$. The gray contours show the sink terms as a percentage of the incident power.

7.2.2 Generation Rates

Figure 7.7 shows the tidally averaged sink terms for the illustrative case. Following initialisation for $1T \leq t \leq 5T$, a small signal is evident depicting the small adjustment of the eddy. When $t \geq 5T$, the forcing turns on and waves propagate inward, reaching the eddy around $t = 9T$, and begin interacting with the eddy. The oscillations between $t = 9T$ and $t = 12T$ are partly an artifact of the sliding mean used for tidal averaging and are not particularly revealing other than to indicate that the interaction has begun. At $t = 13T$, the sink terms have reached quasi-steady state, and we interpret the value as a net conversion rate where a positive (negative) value indicates a sink (source). The $\bar{K}_f + \bar{A}_f$ and $\bar{S}_0$ terms are small compared to $\bar{S}_1$, $\bar{S}_2$ and $\bar{S}_3$. The mode-one, two and three signals are about two orders of magnitude larger here than those from the benchmark case shown in Figure 5.3. The dominant balance here is $\bar{S}_1 + \bar{S}_2 + \bar{S}_3 \approx 0$.

Figure 7.8 shows the quasi-steady sink terms for both the low- and mid-latitude cases by evaluating $\bar{S}_n$ at $t = 25T$. The top panel shows the quasi-steady sink at mode-one, the middle shows mode-two and the bottom mode three, and the left (right) panel shows the low (mid) latitude case. The upper axis is eddy diameter ($D_E = 4L_E$) and the lower axis is power incident to the eddy (incoming energy flux times eddy diameter).

The top panels show that the sink at mode-one is always positive and that mid-latitude evokes a larger magnitude than the low-latitude cases. For the parameters explored here, the low-latitude cases lose up to about 50 MW and the mid-latitude lose up to about 70 MW. Peaks appear in each curve near $D_E = 140$ km ($L_E = 35$ km) for low-latitude and near $D_E = 180$ km ($L_E = 45$ km) for mid-latitude. In all cases, raising the eddy velocity U_E yields a larger sink signal.

The contours on the plot show the sink as a fraction of incident power, expressed as a percentage. This value is interpreted as the fraction of power removed from the mode-one tide as it crosses the eddy. At low latitude, losses reach 8 percent, but reach 13 percent at mid latitude. The fractional losses peak at a smaller diameter than the absolute losses; near $D_E = 120$ km ($L_E = 30$ km) for low-latitude and $L = 140$ km ($L_E = 35$ km) for mid-latitude.

At the middle panel, we see that the mode-two sink is always negative, which makes it a source. The shape of the curves follow that of the mode-one sinks but with magnitude reduced to 60–80 percent. The peaks are comparable to those at mode-one. The lower panel shows similar negative sinks at mode three, much smaller magnitude, and comparable peaks.

7.2.3 Frequency Spectrum

Synthetic mooring data is extracted from two locations: the first is in a mode-two beam at $(x, y) = (325, 250)$ km and the second in a mode-three beam at $(x, y) = (325, 200)$ km. The reference benchmark case is also sampled at $(x, y) = (325, 250)$. The synthetic vertical velocity $w(z, t)$ is projected onto vertical modes one through five, giving a time series for each mode $w_n(t)$. Lastly, the power spectral density is estimated using MATLAB's `pwelch` function and plotted in Figure 7.9.

The top panels show the benchmark case, which reveals that the forced mode-one wave dwarfs all other signals. A small signal is evident in mode-two at the second harmonic in both latitude regimes, which we ascribe to the mode-two signals of Figure 5.4. The low latitude has an even smaller mode-two signal at half of the forced frequency, due to PSI.

The middle panels show the spectrum within a mode-two beam. A strong mode-two signal is visible at the forced frequency, undoubtedly corresponding to the mode-two beam itself. Modes three, four and five are also visible at the forced frequency, but with a smaller magnitude. A variety of weaker signals are discernible at each harmonic, representing scattering of energy to higher frequencies due to numerous wave-wave interactions.

The bottom panels show the mode-three beam spectrums and they paint a similar picture, with mode-three taking the place of mode-two as the second strongest signal at the forced frequency. The strong mode-two signal at the second harmonic is comparable in magnitude to the mode-three signal at the first harmonic. The likely candidate for its generation is interaction between the forced mode-one wave and the generated mode-three beam. Signals at higher frequency harmonics are also present at this location.

7.3 Verification Experiment

The baroclinic eddy verification experiment is conducted to see if the eddy exchanges net energy with the internal tide as it crosses. The expectation is that it will not exchange any net energy, but rather act as a catalyst to enable energy exchange as described by Lelong and Riley (1991).

The modal energy budget approach described in Chapter 4 combines, at modes one and two, the energy of the eddy with the energy of the internal tides. A net sink observed at mode-one may be due to losses in either the mode-one eddy, the mode-one internal tide, or both.

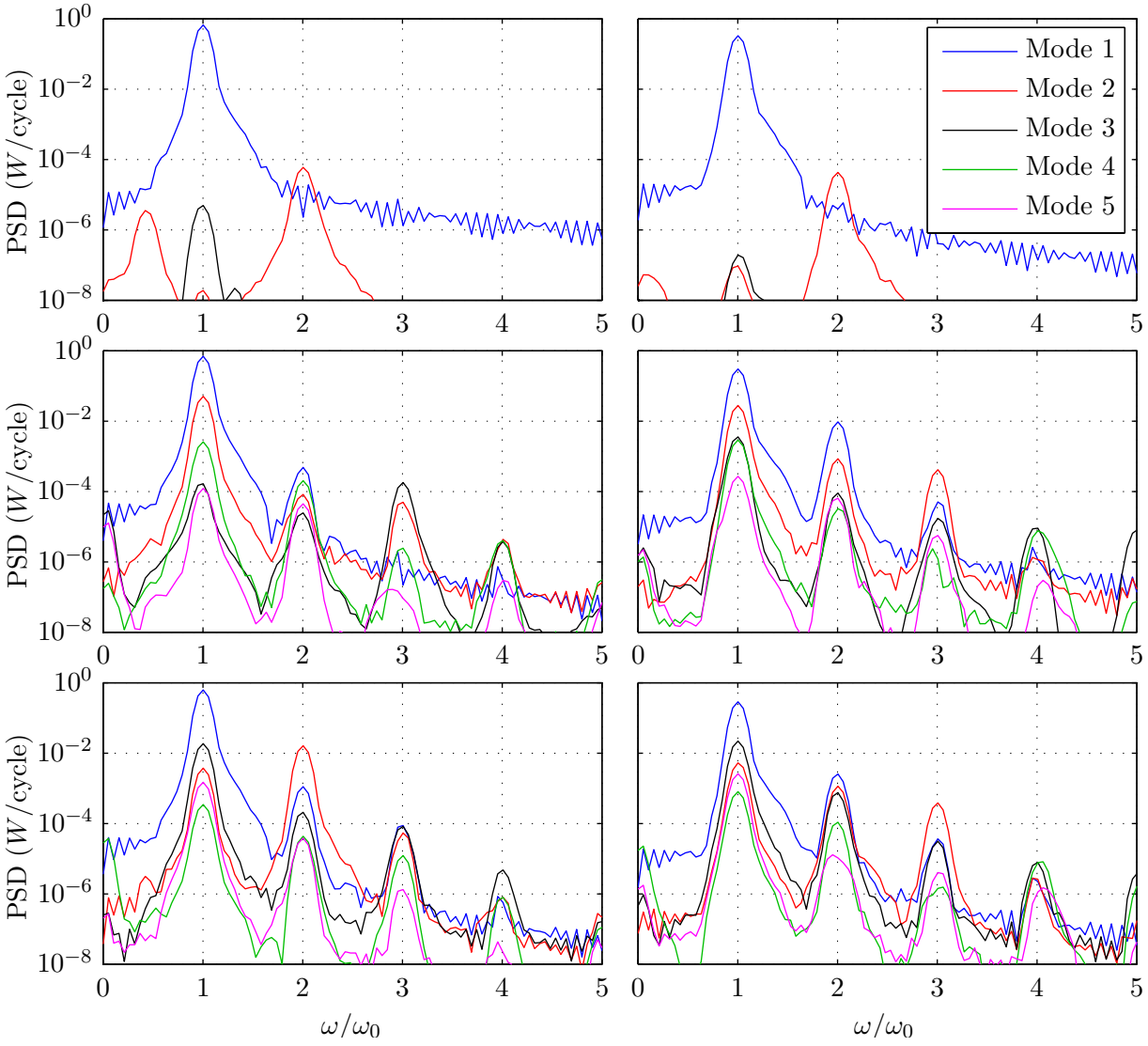

Figure 7.9: Power spectral density estimated for synthetic mooring data after projection onto modes one through five. The top panel shows the reference forcing only case sampled at $(x, y) = (325, 250)$ km. The middle and bottom panels show the illustrative baroclinic eddy case sampled at $(325, 250)$ km and $(325, 200)$ km. The left (right) column shows the low- (mid-) latitude case.

Relaxation regions are added to the domain along the north and south boundaries of the domain, and the width expanded from 400 km to 500 km to make room for these regions as shown in Figure 7.10. An unforced simulation is run out to $t = 45T$ to measure the spindown of the eddy due to numerical viscosity. A second simulation of the same length is conducted where the forcing is ramped up over $5T < t < 7T$ and ramped down over $20T < t < 22T$ for a forcing duration of $15T$. Once the forcing is ramped down, the waves propagate from the energy analysis region and get absorbed in the expanded relaxation regions. Comparing $P(t)$ between the forced and unforced case once the waves have left the domain gives an estimate of how much energy the eddy has lost following $15T$ of interaction with the forced internal tide. We consider one case with parameters $(f, L_E, U_E) = (1.0 \times 10^{-4}\ \text{s}^{-1}, 35\ \text{km}, 45\ \text{cm/s})$.

Figure 7.11 shows a time series of the change in total pseudo-energy within the energy analysis domain (normalised to the initial pseudo-energy). In the absence of any waves, this is a direct measure of the change in the eddy's pseudo-energy. In the unforced case, the eddy undergoes a small adjustment during the first three tidal periods and loses under one thousandth of one percent of its pseudo-energy. The average change in energy during adjustment is roughly $[P(5T) - P(0)]/5T = -18.3$ kW, and that over the remainder of the simulation is roughly $[P(45T) - P(5T)]/40T = -0.15$ kW.

In the forced case, the curve matches the unforced case during adjustment period and until the forced waves begin to enter the energy analysis region. The energy analysis domain saturates by about $t = 13T$. Forcing rampdown begins at $t = 20T$ and the pseudo-energy in the analysis domain begins to drop as waves propagate from the analysis domain around $t = 24T$ and by $t = 35T$ has dropped to within one hundredth of one percent of the initial pseudo-energy, remaining remains below this level through to the end of the simulation. We estimate the average change as $[P(35T) - P(5T)]/30T = 25.2$ kW.

These estimates for the average eddy energy change are small compared to the mode-one sink and mode-two source that are three orders of magnitude larger. Thus it is fair to deduce that the energy source of the mode two and mode three waves is the forced mode-one wave and not the baroclinic eddy. The eddy does not exchange net energy with the waves, supporting a wave-wave-vortex triad explanation as the energy scattering mechanism.

7.4 Convergence

We conduct a convergence check to confirm the use of sufficient resolution. The illustrative case is re-simulated at 4, 2, 1, and 0.25 km horizontal resolution. We use a time step of

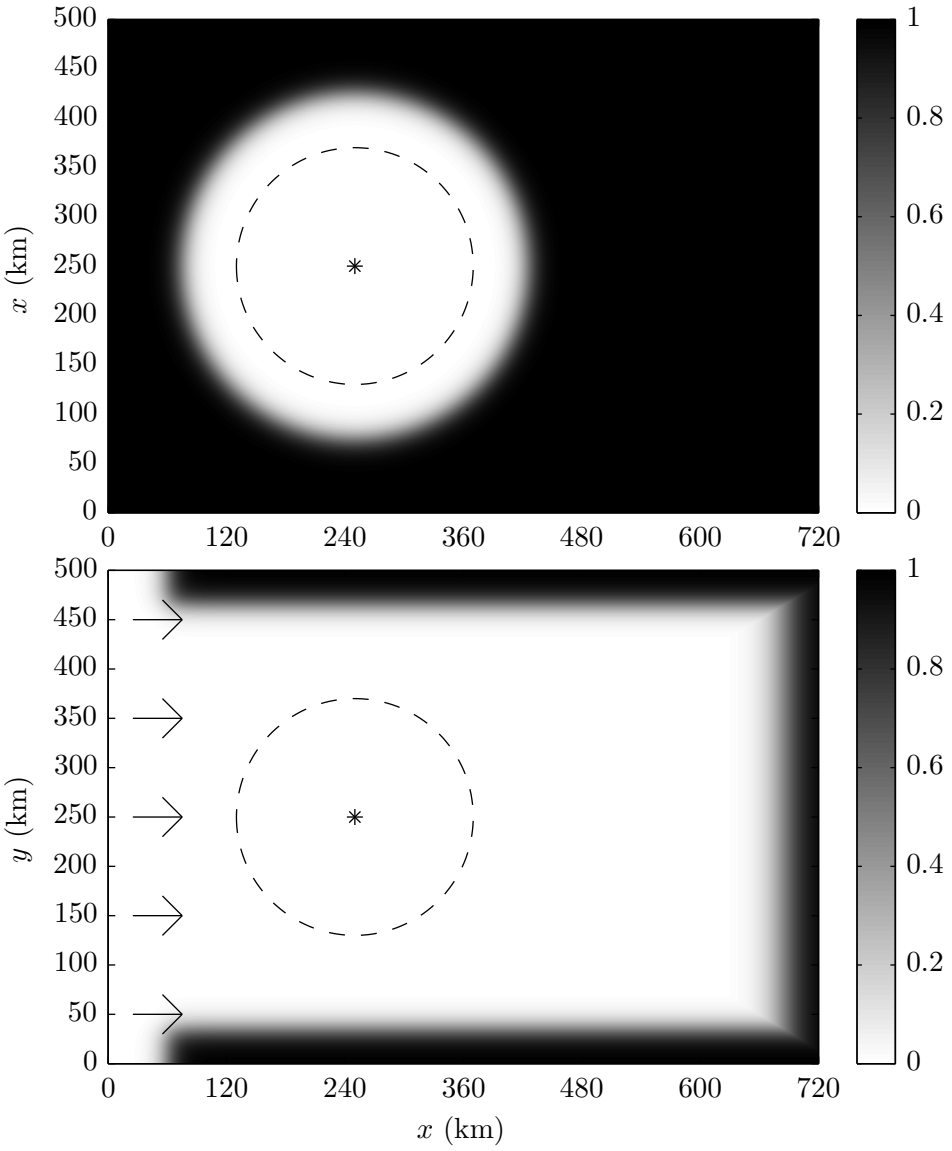

Figure 7.10: The domain used for the baroclinic eddy verification case during (top) the adjustment phase and (bottom) the forced phase.

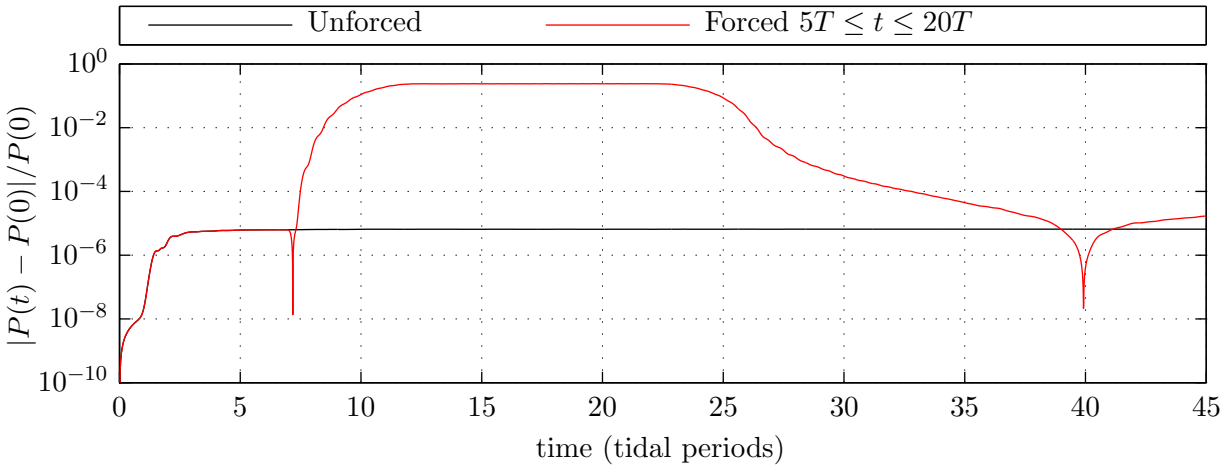

Figure 7.11: The difference between the eddy's total pseudo-energy $P(t)$ and the pseudo-energy upon initialisation $P(0)$, normalised by $P(0)$. The black curve shows the unforced reference case and red shows the verification experiment.

69 s for all cases except 0.25 km, where we use 23 s. The top figure of Figure 7.12 shows the residual in the global pseudo-energy budget (4.77) for each case and the lower panel shows the maximum absolute residual over $15T < t < 30T$ as a function of resolution.

A large residual is present while the energy analysis region is saturating ($8T < t < 13T$), but drops to a consistent smaller value once reaching quasi-steady state ($13T < t < 30T$). The maximum absolute residual at the 0.5 km resolution is about 0.11 MW, a value small compared to the sink values reported earlier in this chapter. A 60% drop in residual results when moving from 4 km to 2 km resolution. Improvements beyond that are modest— a four fold increase in resolution moving from 2 km to 0.5 km only reduces the residual by 34%. The last drop to 0.25 km resolution yields a residual reduction of 40%, and is likely due in large part to the time step reduction used as well. We conclude that the horizontal resolution of 0.5 km used here is appropriate.

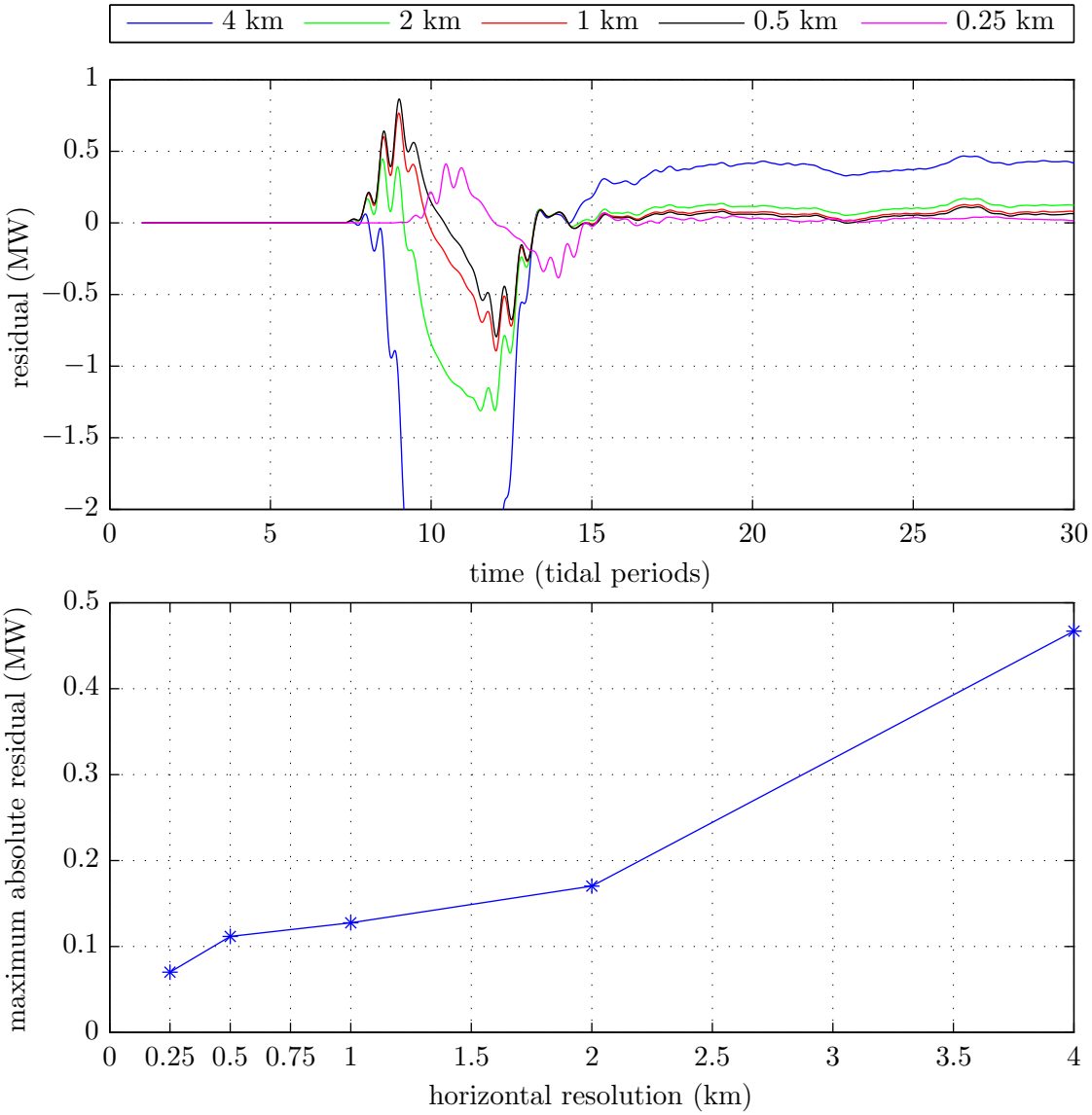

Figure 7.12: (top) The residual in the pseudo-energy budget for five different resolutions, and (bottom) maximum absolute residual over $15T < t < 30T$ as a function of resolution.

Chapter 8

Ray Tracing

In this chapter we investigate the utility of ray tracing to predict the result of mode-one and two internal tides interacting with a barotropic eddy. We begin by outlining a set of fully nonlinear numerical experiments conducted with the MITgcm which we use as a reference. Time stepping the ray tracing equations produces ray paths corresponding to parameters from the MITgcm cases, and we analyse five of the resulting paths.

To enable comparisons between ray tracing results and fully nonlinear numerical simulation outputs, we use a ray tracing methodology and post processing procedure which reconstructs a complete wave field using numerous ray paths. We build reconstructions for five of the numerical experiments and compare them with the numerical results to evaluate the reconstruction approach.

8.1 Numerical Experiments

The numerical experiments conducted for this chapter are similar to those conducted in Chapter 6. Each experiment uses a forcing amplitude of $U_t = 2.5$ cm/s and the low-latitude Coriolis parameter of $f = 0.5 \times 10^{-4}$ s^{-1}. Table 8.1 lists the four domains used and the varied parameters are the forcing mode (we consider modes one and two), and the eddy velocity and length scale. Table 8.2 lists the chosen values, and also includes the corresponding vortex Rossby number (2.50), the ratio of internal tide wavelength to eddy length scale $\epsilon = \lambda/L_E$, and the ratio of peak eddy velocity to group velocity, $\delta = U_E/|\vec{c_g}|$. The simulations run until the leading edge of the forced internal tide reaches the sponge region at the east boundary.

Table 8.1: Domains used for ray tracing investigation.

Domain	Δt (s)	x_c (km)	y_c (km)	$L \times W \times H$ (km)	$\Delta x \times \Delta y \times \Delta z$ (km)
A	69	180	337.5	$675 \times 675 \times 5$	$1 \times 1 \times 0.25$
B	69	405	675	$1080 \times 1350 \times 5$	$1 \times 1 \times 0.25$
C	69	675	1125	$1800 \times 2250 \times 5$	$1 \times 1 \times 0.25$
D	103.5	1350	2250	$3600 \times 4500 \times 5$	$1.5 \times 1.5 \times 0.25$

Table 8.2: Set of runs conducted for ray tracing.

Case	L_E (km)	Mode	U_E (cm/s)	$\epsilon = \frac{\lambda}{L_E}$	$\delta = \frac{U_E}{\lvert\vec{c_g}\rvert}$	$R_o = \frac{U_E}{0.48 f L_E}$
A1a	45	1	10	1.69	0.067	0.093
A1b	45	1	20	1.69	0.13	0.19
A1c	45	1	30	1.69	0.20	0.28
A2a	45	2	10	0.85	0.13	0.093
A2b	45	2	20	0.85	0.27	0.19
A2c	45	2	30	0.85	0.40	0.28
B1a	135	1	10	0.56	0.067	0.031
B1b	135	1	20	0.56	0.13	0.062
B1c	135	1	30	0.56	0.20	0.093
B2a	135	2	10	0.28	0.13	0.031
B2b	135	2	20	0.28	0.27	0.062
B2c	135	2	30	0.28	0.40	0.093
C2a	225	2	10	0.17	0.13	0.019
D1b	450	1	20	0.17	0.13	0.019
D2a	450	2	10	0.085	0.13	0.0093
D2b	450	2	20	0.085	0.27	0.0093

8.2 Ray Paths

We compute ray paths by time stepping equations (2.46) numerically with the forward Euler stepping scheme. We employ three rays that form a triangle centred about a nominal initial position to handle energy evolution. Upon initialisation, we find the initial wave action density $\hat{A} = E/\omega_r$ and the triangle area a. After each time step of equations (2.46), we find the new triangle area a^{n+1} and use the conservation of wave action, $\hat{A}^n a^n = \hat{A}^{n+1} a^{n+1}$, to find the post-time step wave action density $\hat{A}^{n+1}$, and use (2.45) to find ω_r^{n+1}. Lastly the post-time step energy is $E^{n+1} = \hat{A}^{n+1}\omega_r^{n+1}$.

We compute ray paths and energies for nine wave packets entering an eddy from the west along $y = y_c + aL_E$ for $a = (0, \pm 0.5, \pm 1, \pm 1.5, \pm 2)$. For illustrative purposes, we choose the MITgcm case `A2b` and use the parameters from Table 8.2. Figure 8.1 shows the ray paths on a pseudo-colour backdrop of the eddy velocity and velocity gradients, which reveals that

- the wave that enters the eddy along $y = y_c$ (black curve) is strongly deflected to the north.
- waves crossing the eddy along $y = y_c \pm 2L_E$ (outermost white curves) experience little deflection, essentially missing the eddy. A slight deflection to the south results from entering the eddy at $y = y_c \pm 1.5L_E$ (inner white curves).
- waves that enter the eddy along $y = y_c \pm 0.5L_E$ (blue curves) and $y = y_c \pm L_E$ (red curves) experience varying degrees of deflection, some to the south and some to the north.
- the area to the east of the eddy shows an asymmetric collection of irregularly aligned ray paths, including rays that intersect with other rays.

To assist in interpreting the curves, recall that the ray tracing equations (2.46) in component form are

$$\frac{\mathrm{d}x}{\mathrm{d}t} = c_{g_0,x} + U, \tag{8.1}$$

$$\frac{\mathrm{d}y}{\mathrm{d}t} = c_{g_0,y} + V, \tag{8.2}$$

$$\frac{\mathrm{d}k}{\mathrm{d}t} = -k\frac{\partial U}{\partial x} - l\frac{\partial V}{\partial x}, \tag{8.3}$$

$$\frac{\mathrm{d}l}{\mathrm{d}t} = -k\frac{\partial U}{\partial y} - l\frac{\partial V}{\partial y}. \tag{8.4}$$

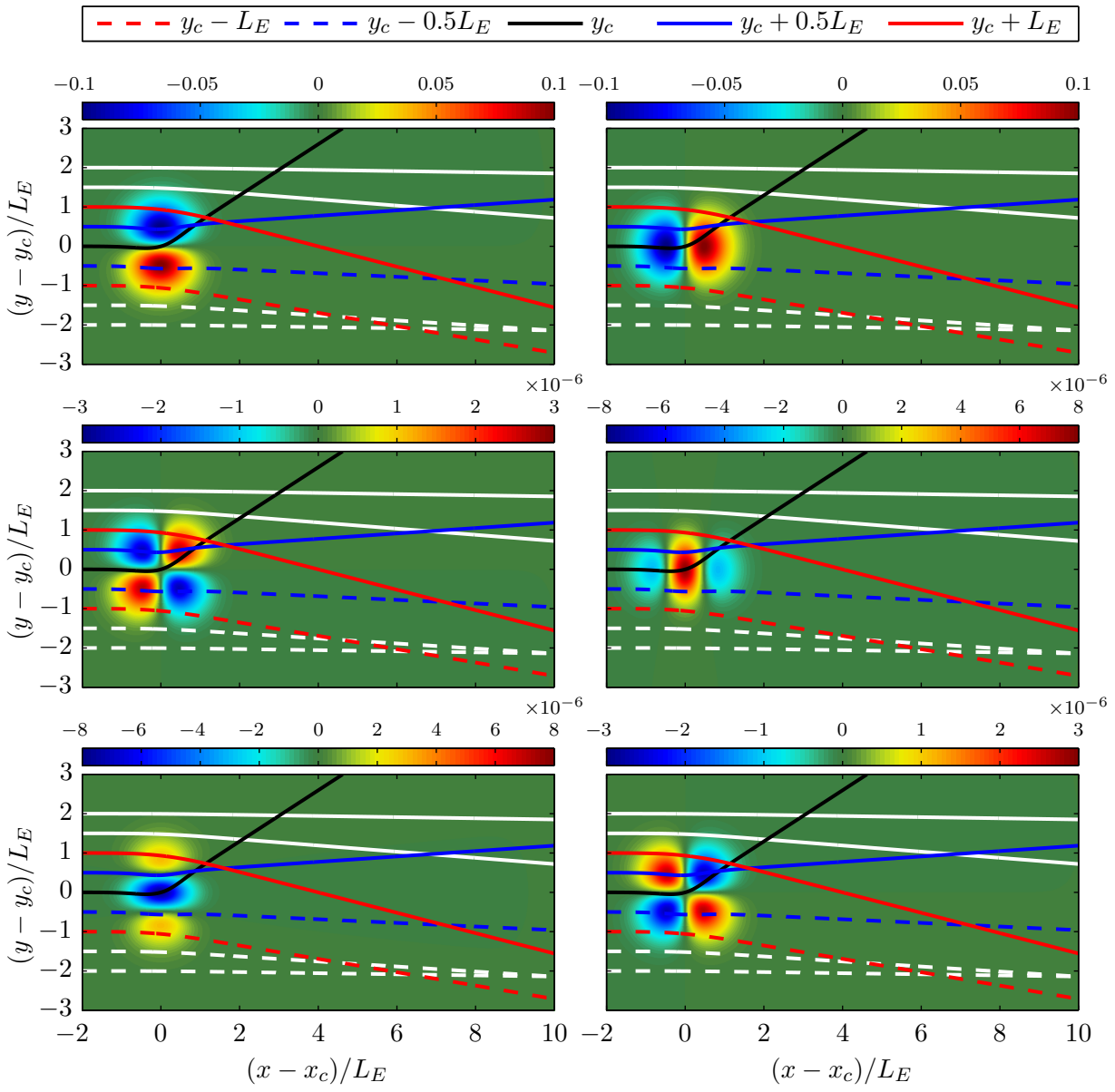

Figure 8.1: Nine ray paths overlaid on heatmaps of, from top to bottom, (left) u, u_x and u_y, and (right) v, v_x and v_y. The wave packets are mode-two, $U_E = 10$ cm/s, $L_E = 45$ km and $\delta = 0.13$. The horizontal coordinates are centred at the eddy centre (x_c, y_c) and normalised by L_E. The white lines show $y = y_c \pm 1.5L_E$ and $y = y_c \pm 2L_E$, and examine the rays corresponding to the five legend in more detail in Figure 8.2.

The rays propagate in the direction of the group velocity, which has two components: the intrinsic group velocity and the local background current velocity. The phase velocity is parallel to the wave vector, and in the absence of a background velocity, the phase and group velocity are also parallel. Here the background velocity peaks at 10 cm/s and the intrinsic group velocity is 74 cm/s. Thus the propagation direction is heavily weighted toward the intrinsic group velocity, and consequently the group and phase speeds are only approximately parallel while rays are inside of the eddy. Increasing the eddy velocity will reduce the alignment of the group and phase speeds.

Figure 8.2 shows the properties of wave packets entering the eddy along $y = y_c + aL_E$ for $a = (0, \pm 0.5, \pm 1)$ as a function of distance along the ray path. The curves show that

- at $y = y_c$, the wavenumber, relative frequency, and phase speed do not change as the packet passes through the eddy, while the group speed is temporarily increased slightly. The ray experiences a small deflection to the south as it enters the west edge of the eddy where the v is maximum negative as predicted by (8.2). However once it reaches the centre, it experiences negative u_y and positive v_x, which act to increase l via (8.4) and decrease k via (8.3). The ray exits the eddy after turning about 33 degrees counterclockwise, and the energy is negligibly affected. The ray propagates approximately normal to the eddy velocities such that $\vec{k} \cdot \vec{U} \approx 0$, which explains the constant relative frequency.

- at $y = y_c + 0.5L_E$, the packet enters the eddy against the eddy velocity near the peak (recall the peak eddy velocity occurs at about $0.48L_E$ from the centre). The relative frequency increases because $k \cdot \vec{U} < 0$. The horizontal wave number κ increases during transit due to an increase in the k wavenumber as it enters through negative u_x, and κ is reduced as it exits through positive u_x. The group and phase speeds reduce while in the eddy, and the propagation direction shifts slightly north upon exit. The energy briefly spikes to a high level just as it exits the eddy, and then undergoes a terminal decline.

- at $y = y_c + L_E$, having entered the eddy against weaker eddy velocity, the wavenumber, relative frequency, group and phase speeds show similar although weaker changes as those seen in the $y = y_c + 0.5L_E$ case. The final direction, however, shows a deflection of a few degrees south, and the energy drops in magnitude, opting not to show a temporary spike.

- at $y = y_c - 0.5L_E$, the packet enters with the peak eddy velocity, and the relative frequency decreases due to $\vec{k} \cdot \vec{U} > 0$. The l wavenumber sees little change and the

k wavenumber temporarily decreases as it passes through positive and then negative u_x, and κ reflects the temporary drop. The group and phase speed increase while in the eddy. The packet exits with a small deflection to the south, and the energy shows a simple decline.

- at $y = y_c - L_E$, entering south of the peak velocity shows a similar although muted response in the wavenumber, relative frequency and group and phase speeds when compared to $y = y_c - 0.5L_E$. The propagation direction deflects roughly 15 degrees to the south. The energy signal slowly rises after leaving the eddy, briefly spikes to a high level while about one eddy diameter distant from the eddy, and then begins its decline.

The response of the wave parameters κ, ω_r, $|\vec{c}_g|$ and $|\vec{c}_p|$ to crossing the eddy is approximately anti-symmetric, that is, at $y_c + aL_E$ the response is approximately the opposite of that at $y = y_c - aL_E$. However, the propagation direction and energy curves do not follow that pattern.

The examined paths suggest that there may exist classes of ray behaviour that depend on the offset along which the packets enter the eddy. Indeed, computing ray paths for many finely spaced entry offsets reveals four classes of rays paths. Figure 8.3 illustrates the four classes of rays, showing

- (top left) the "North spreading" rays, where each ray deflects to the south and in the farfield they undergo spreading. There are no ray crossings in the farfield.
- (top right) the "North crossover" rays, which cross at a point near the eddy boundary before undergoing farfield spreading in a fanned out pattern.
- (bottom left) the "South spreading" rays, which are much like the "north spreading" rays except they deflect to the north and undergo stronger spreading.
- (bottom right) the "South crossover" rays, which deflect only slightly to the south and cross others at a farfield location distant from the eddy, before undergoing a fanned out spreading.

Table 8.3 lists the entry offset extents of each band that were (approximately) determined by a trial and error approach.

Varying the eddy size L_E produced the same ray paths when plotted in horizontal coordinates normalised by L_E. As the ray tracing equations are linear, this is expected.

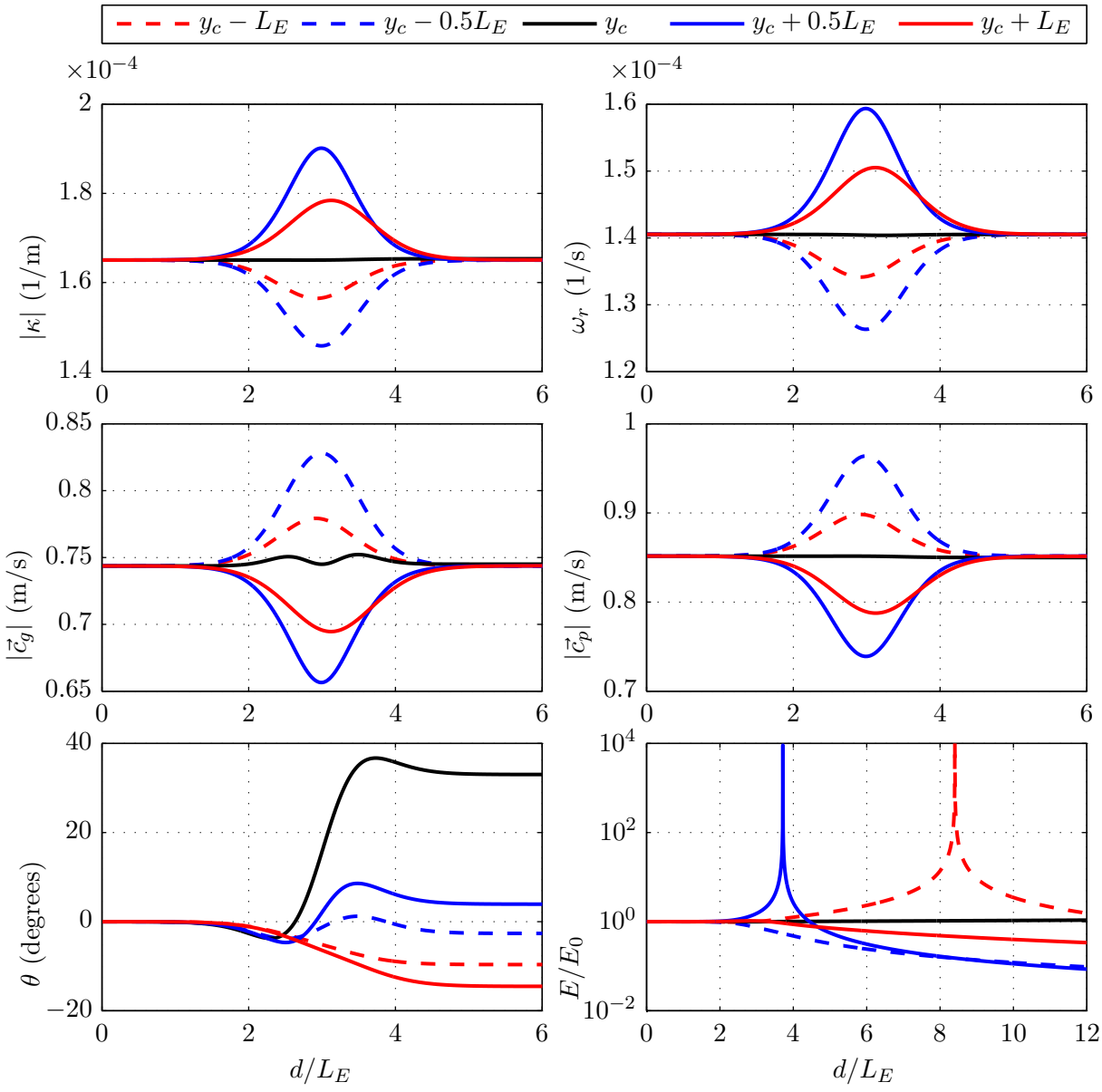

Figure 8.2: Ray variables for five selected rays plotted as a function of d, the distance along the ray path, normalised by L_E. The legend is consistent with that in Figure 8.1.

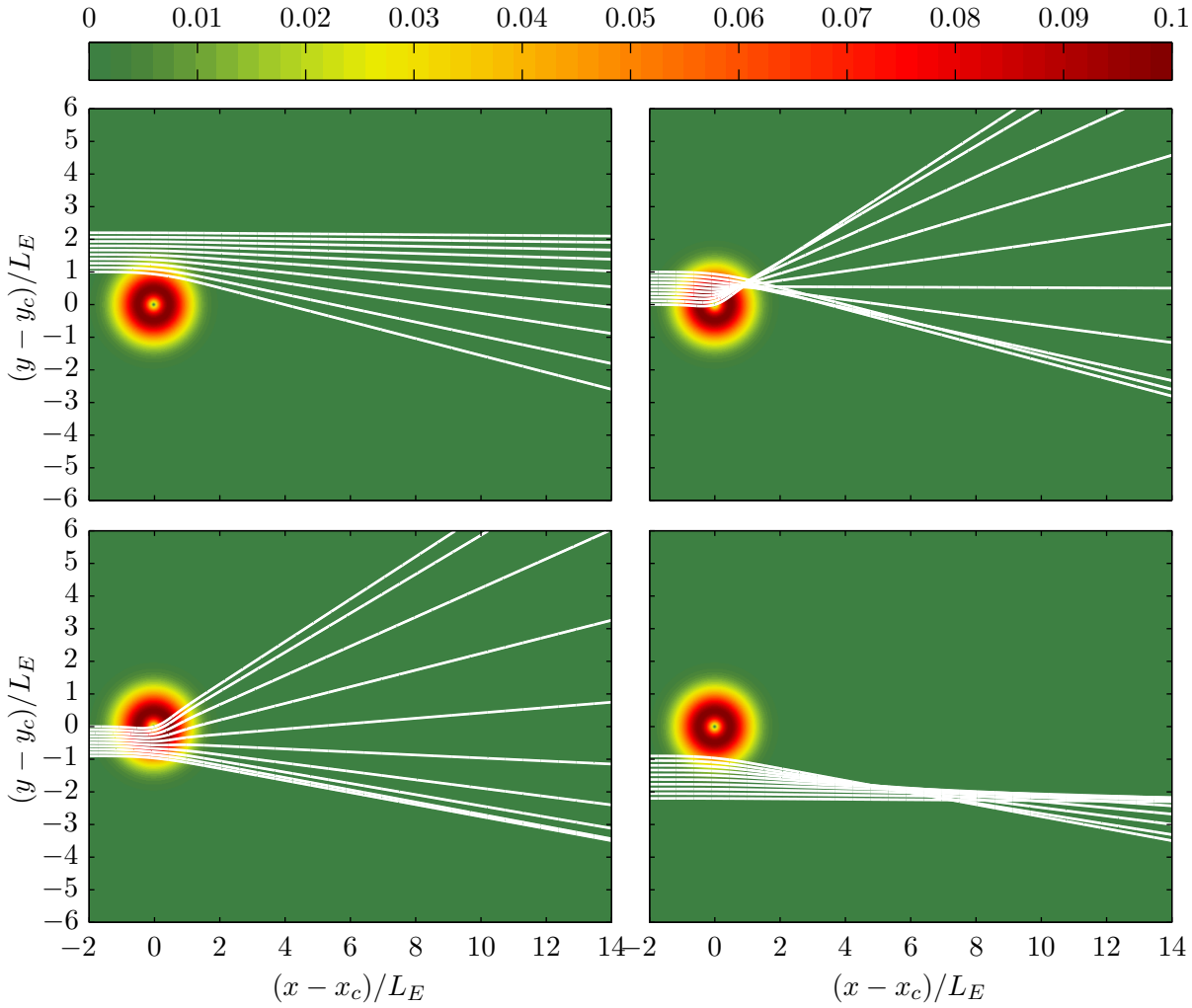

Figure 8.3: Four families of ray paths arising from ray tracing through an eddy where $\delta = 0.13$. The heatmap shows eddy velocity in m/s.

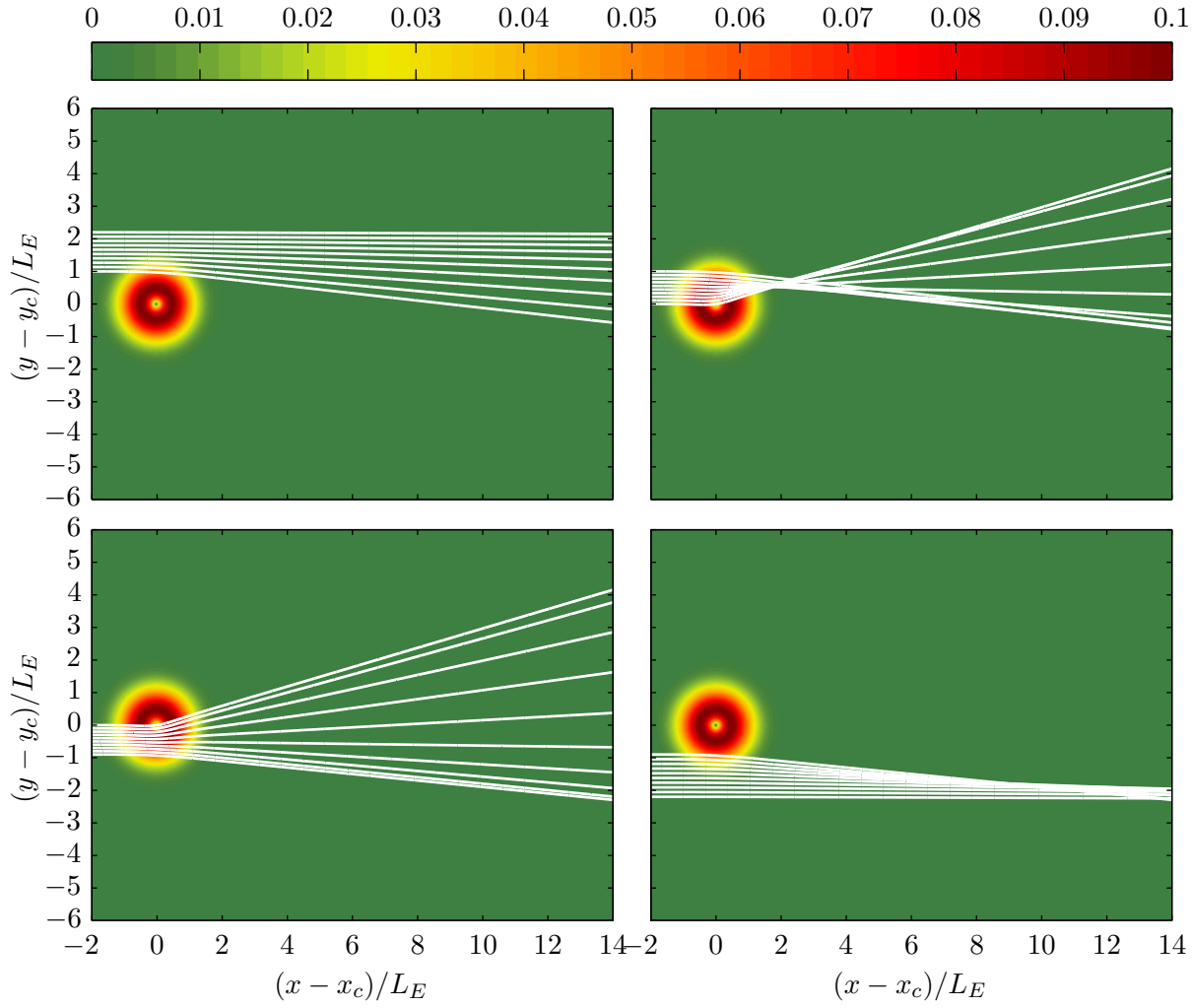

Figure 8.4: Four families of ray paths arising from ray tracing through an eddy where $\delta = 0.067$. The heatmap shows eddy velocity in m/s.

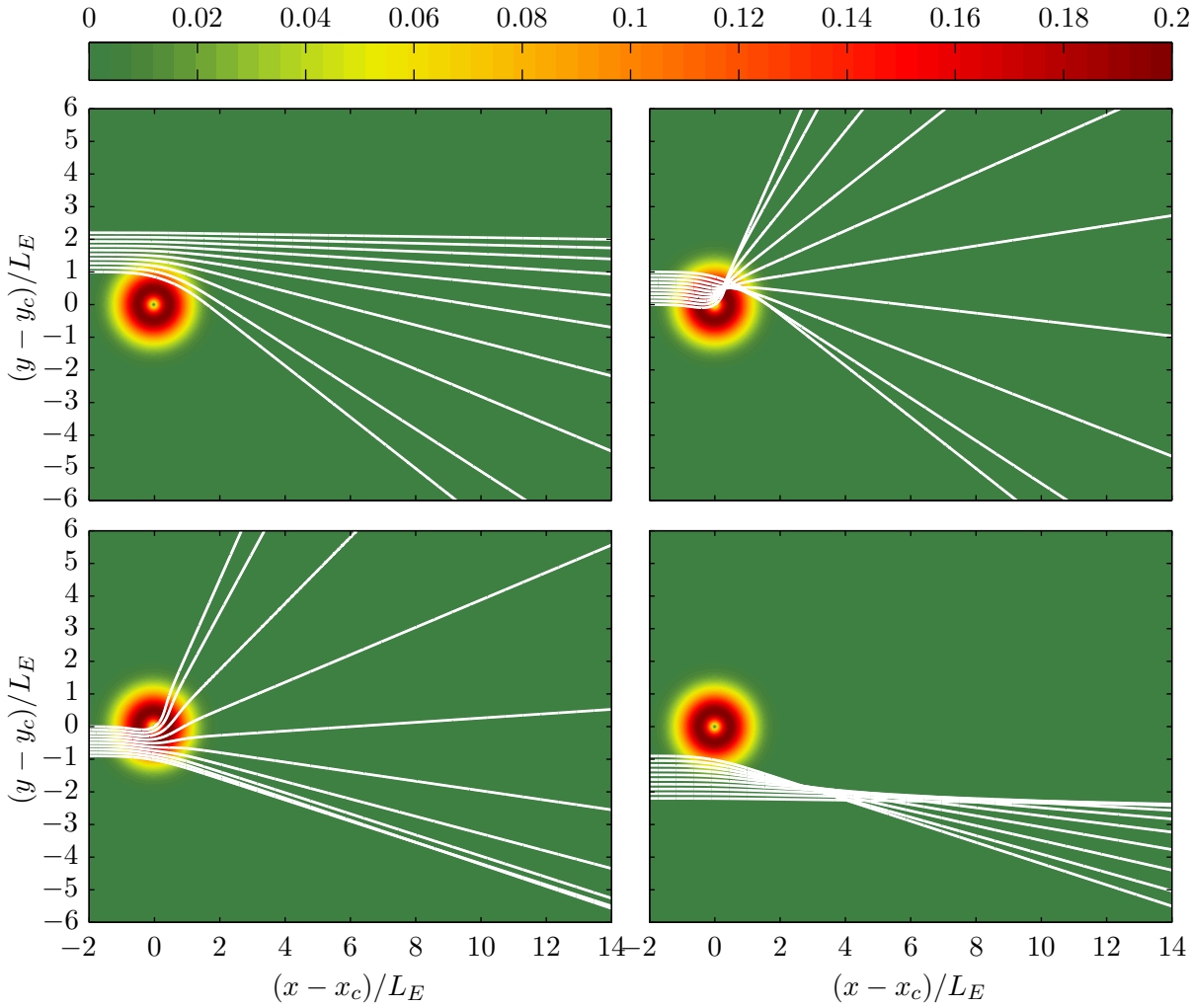

Figure 8.5: Four families of ray paths arising from ray tracing through an eddy where $\delta = 0.27$. The heatmap shows eddy velocity in m/s.

Table 8.3: Ray path families determined approximately by trial and error.

Class	Entry offsets
North spreading	$y = y_c + (1.0, 2.2)L_E$
North crossover	$y = y_c + (0.0, 1.0)L_E$
South spreading	$y = y_c + (-0.9, 0.0)L_E$
South crossover	$y = y_c + (-2, 2, -0.9)L_E$

The important parameter here is $\delta = U_E/|\vec{c}_g|$, the varying of which yields different ray paths. Figures 8.4 and 8.5 show the four classes of rays after a halving and doubling of δ, respectively. At smaller δ (weaker eddy currents) the ray paths deflect less and spreading reduces in the far field, while a larger δ (stronger eddy currents) yields both larger deflections and spreading. The entry offset extents of Table 8.3 are (at least approximately) preserved under this halving/doubling of δ.

The boundary of the farfield spreading fan of rays found in the two "crossover" classes are also locations where caustics form (recall that caustics are regions where adjacent ray paths intersect). The dramatic rise in energy in two of the curves from Figure 8.2 are evidence of caustics. Computing many ray paths at finely spaced eddy entry offsets permits the identification of caustics by checking adjacent ray paths for intersection. The locus of such intersections form caustics. Figure 8.6 shows the location of the caustic loci for four values of δ as computed via an adjacent ray intersection search.

8.3 Wavefield Reconstruction Method

The ray paths computed in the previous section are ill suited for comparison with model output fields. This section describes a method of synthesising a wave field from ray tracing results.

The overview of the method is to create a grid of wave packet starting points positioned to the west of the numerical model forcing boundary. We trace each packet's position, energy and central phase from $t = 0$ to the model output time. The ray tracing results yield the flow variables at the final ray positions via the polarisation relations, and an interpolation process collects the data at the model grid points.

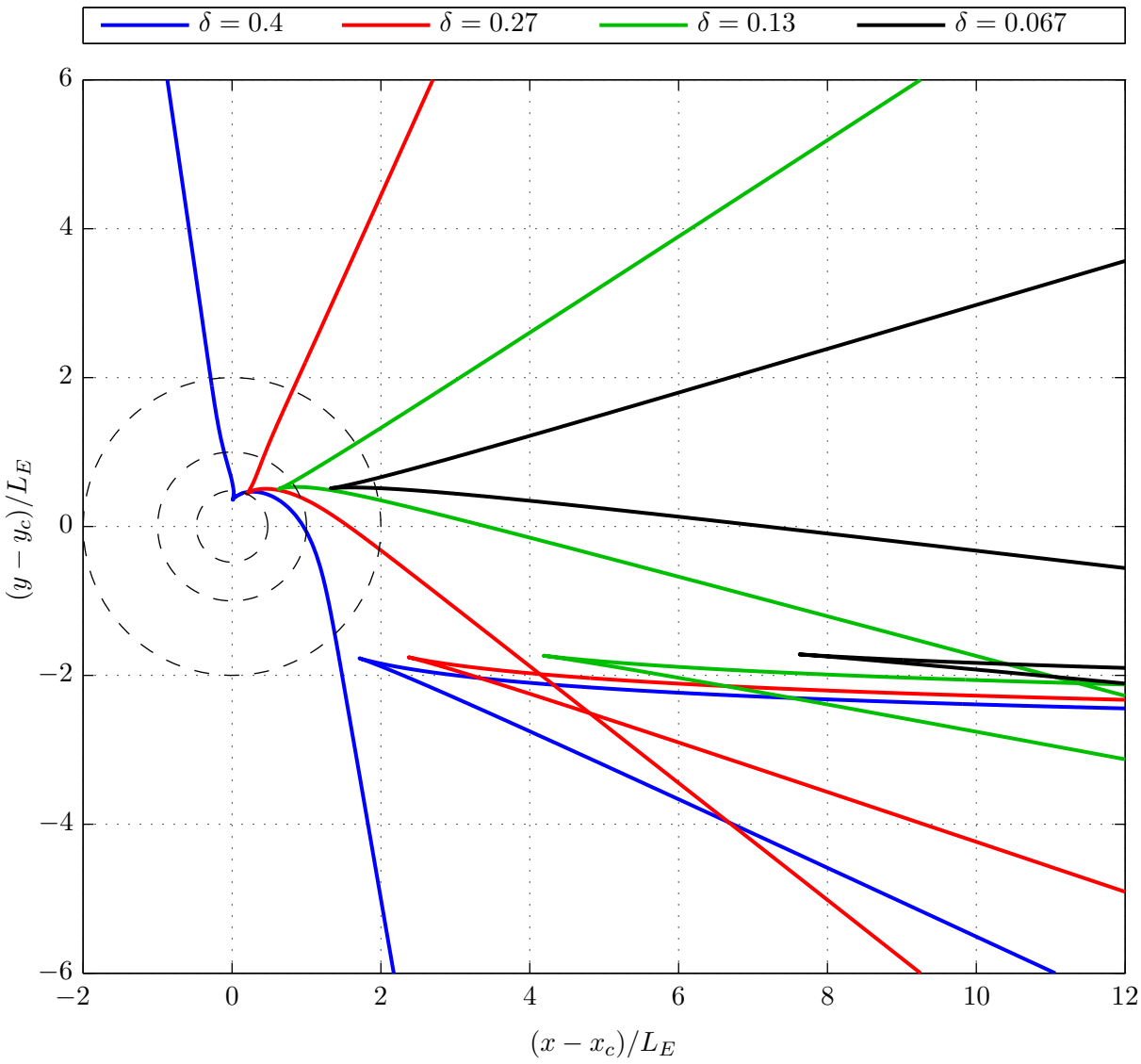

Figure 8.6: The locus of points where caustics form at four values of δ. The black dashed lines show the $r/L_E = 0.48$, 1, and 2 contours.

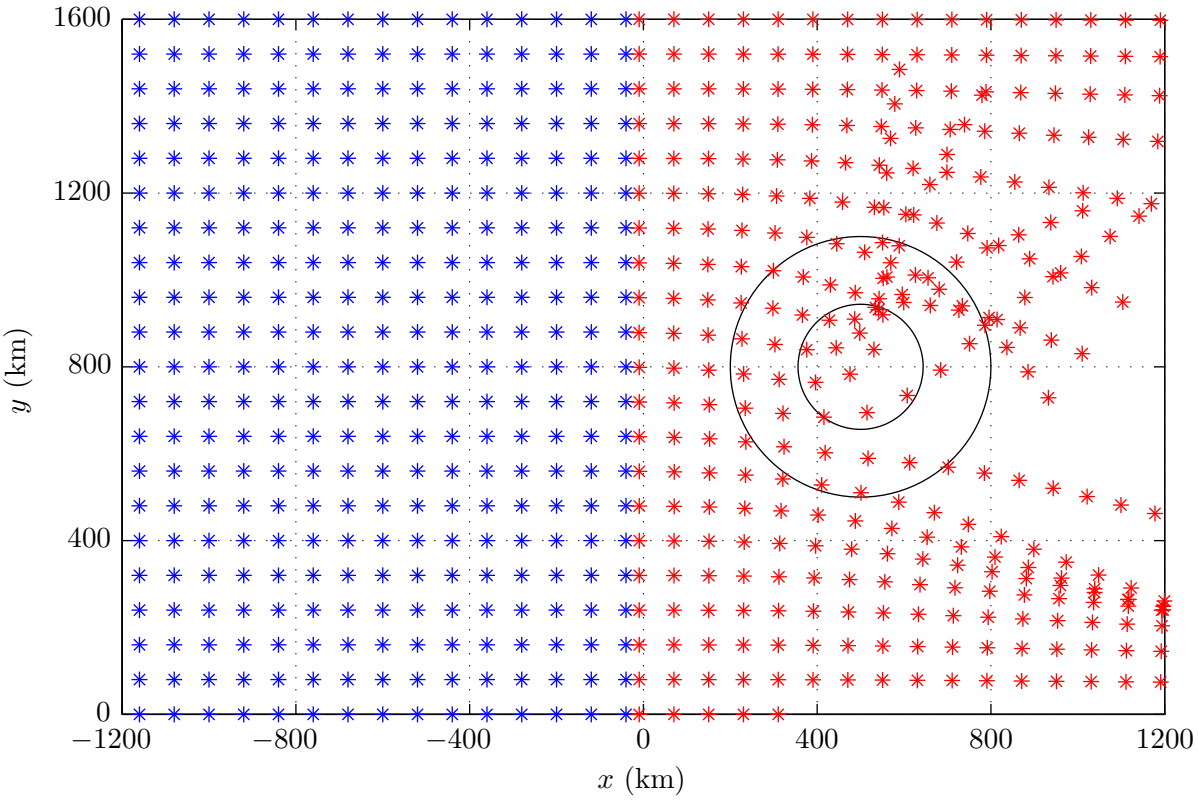

Figure 8.7: An example of ray tracing results, where the blue markers indicate the initial positions and red markers indicate the final positions. The black lines show the $r/L_E = 0.48$ and 1 contours of the eddy through which the wave packets propagate.

8.3.1 Wave Array Initialisation

We initialise a grid of wave packets in an equal sized duplicate domain to the west of the MITgcm domain as depicted with blue markers in the left half of Figure 8.7. Each packet has an initial wave vector directed due east $\vec{k}_{h_0} = (k, 0)$ such that it propagates into the MITgcm domain across the west boundary, mimicking the MITgcm western boundary forcing. The initial amplitude of each wave is $u_0 = U_t$, the forcing amplitude, and the polarisation relation (2.38b) converts that to w_0, which reads

$$w_0 = -u_0 \frac{k}{m_n}. \tag{8.5}$$

The pseudo-energy density equation (2.41) assigns an initial energy $\overline{E}$ to each packet and $\phi_0 = \vec{k}_{h_0} \cdot \vec{x}_0$ assigns the initial central phase. The phase increment with each time step is

$$\Delta\phi = \vec{k} \cdot (\Delta x, \Delta y) - \omega \Delta t = (\vec{k} \cdot \vec{c}_g - \omega)\Delta t, \tag{8.6}$$

and thus we update the central phase with

$$\phi^{n+1} = \phi^n + (\vec{k} \cdot \vec{c}_g - \omega)\Delta t. \tag{8.7}$$

We step the equations from $t = 0$ until the output time of the MITgcm simulation. The red markers in the right half of Figure 8.7 show an example of the final positions after time stepping.

8.3.2 Flow Variable Recovery

We convert the energy $\overline{E}$ at each final position to amplitude w_0 using (2.41),

$$w_0 = \overline{E}^{1/2} \left[\frac{\rho_0 H}{8} \frac{m_n^2}{\kappa_h^2} \left(1 + \frac{f^2}{\omega^2} + \epsilon_{nh} \frac{\kappa_h^2}{m_n^2} \right) + \frac{\rho_0 H}{8} \frac{N_0^2}{\omega^2} \right]^{-1/2}. \tag{8.8}$$

The polarisation relations (2.38) recover the flow variables (u, v, etc) with use of the tracked central phase as the argument to the cos and sin terms.

8.3.3 Interpolation Process

The last step is to interpolate the flow variable data onto a target grid, which we take as the MITgcm grid here. We perform the interpolation process "strip by strip" and superpose the

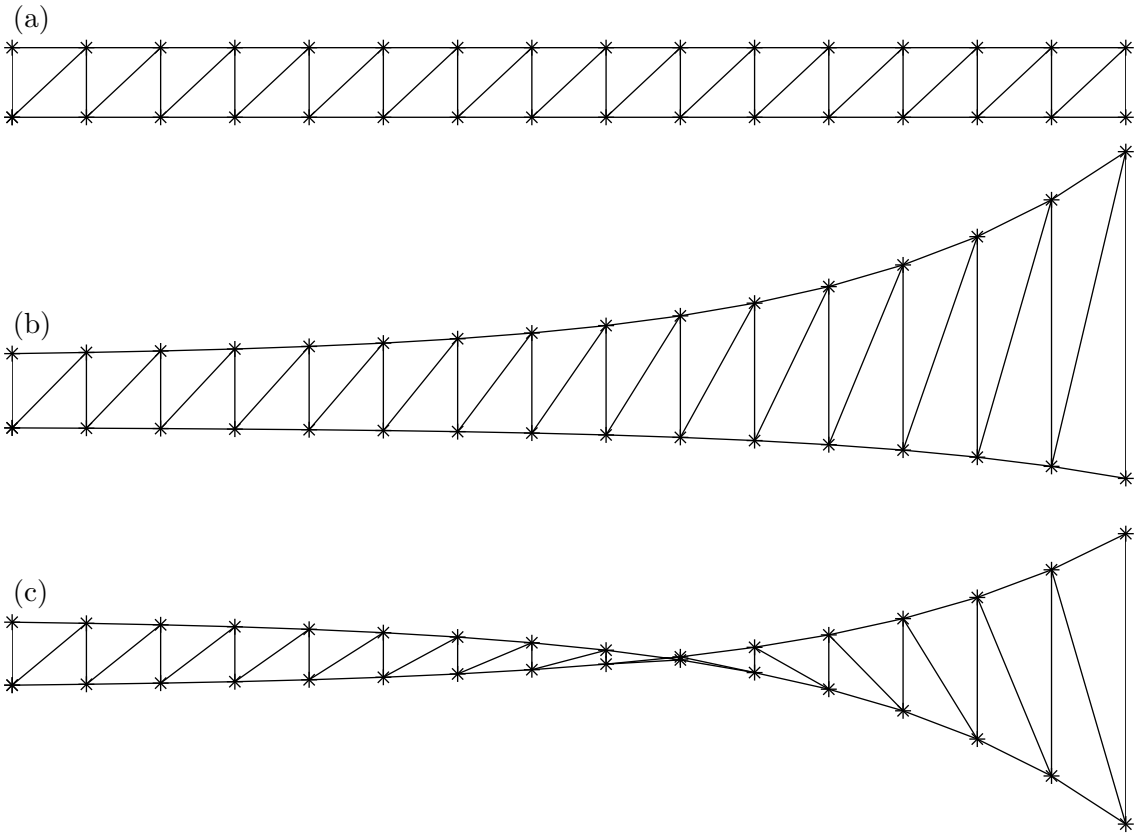

Figure 8.8: Depiction of the stripwise triangulation showing (a) an initial rectangular strip, (b) a deformed post-ray tracing strip showing spreading and (c) a deformed post-ray tracing strip where a caustic has formed near the centre. The markers indicate wave packet positions.

interpolated strips. Adjacent rows of initial wave positions form a rectangular strip in the duplicate domain, and after tracing them into the model domain, the final positions outline a deformed strip. We triangulate the area inside the strip and maintain the triangulation after deformation, as depicted in Figure 8.8. We then interpolate the flow data from the corners of each triangle onto any target grid points that fall within each triangle. Repeating the process for each strip and superposing the results yields a complete wavefield on the target grid.

In the case of intersecting ray paths, as in the last panel of Figure 8.8, a caustic is formed at the intersection point and energy (amplitude) estimates are poor in its vicinity.

The interpolation performs well when the deformation of each strip is slight. In the case of strong strip deformation, the triangles within the deformed strip will have a poor aspect ratio yielding poorly interpolated data. In extreme cases, the triangles overlap and the stripwise interpolation breaks down. However, we can control the strip width and consequently the amount of deformation by adjusting the spacing between adjacent rows of rays.

Derived fields such as energy flux or kinetic energy density are computed from the reconstructed flow fields on the target grid. We compute tidally averaged fields by averaging the constructed field at equally spaced intervals spanning a tidal period.

8.4 Wavefield Reconstructions

We reconstruct wavefields for each of the cases in Table 8.2 and illustrate the results with five of them, beginning with a large scale separation parameter ($\epsilon > 1$) and progressing toward a proper WKBJ scale separation ($\epsilon \ll 1$). At large ϵ, we expect a lack of agreement between the MITgcm output and the ray tracing reconstruction, and as we reduce ϵ we expect improved agreement.

We begin with the smallest eddy where $L_E = 45$ km. Figure 8.9 shows the density perturbation for cases `A1b` (top) and `A2a` (bottom) where the left panels show the MITgcm output and right panels show the ray tracing reconstruction. The values of ϵ are 1.69 and 0.85.

At the top, the left plot shows that the MITgcm predicts a wave field only slightly modified by the eddy. However, the ray tracing reconstruction in the right plot shows a large wedge shaped region containing an intensified density signal. A band of weak density perturbation resides south of the large wedge region, and a small, thin wedge region appears further south. These features are not discernible from the MITgcm plot.

At the bottom, we find alternating bands of stronger and weaker density perturbation in the MITgcm field. The ray tracing prediction captures some of the alternating bands, but only within the large wedge shaped region. The weakened band and thin wedge are similar to those in the previous case.

Figure 8.10 depicts the same cases as Figure 8.9, but shows tidally averaged energy flux magnitude. The solid green value to the west of the eddy is the undisturbed incoming energy flux. Both MITgcm panels show disturbances in the energy flux over most of the domain in the form of alternating hot/cold beams, and the lower panel shows beams much stronger in magnitude than the upper panel. The reconstructions do a poor job at predicting the alternating beams, although there is some evidence of beams within the large wedge shaped region.

The sharp boundaries of both the large wedge shaped region and thin wedge shaped region are caustics. Both cases have $\delta = 0.13$, and the locations of the caustics are consistent with expectation from Figure 8.6.

Moving to a larger eddy with $L_E = 135$ km, we show cases `B1c` and `B2b` in Figure 8.11. The corresponding scale separation parameters are 0.56 and 0.28. At the top, the MITgcm plot shows strong alternating beams, and evidence of these arise within the large wedge shaped region of the reconstruction, although the positioning is not consistent. South of the large wedge the agreement remains poor. At the bottom, the disturbances in the MITgcm plot are beginning to resemble a wedge shaped region. The interference patterns within the wedge are largely reproduced in the reconstruction, although positioning is not exact. The weakened band that is not overlapped with the wedge is comparable, although the southern thin wedge is poor. These cases have δ values of 0.20 and 0.27, leading to larger wedge shaped regions consistent with the loci in Figure 8.6.

Figure 8.12 shows the tidally averaged energy flux magnitudes corresponding to Figure 8.11. The top left shows strong alternating beams, which are partly reproduced within the wedge at the right. The weak band is reasonably well reproduced, although the south wedge is poor. The bottom left shows alternating bands to the north east of the eddy, and to the east shows several short beams. The reconstruction to the right reproduces most of these features, with some allowances for positioning.

In both figures, the signal in the immediate vicinity of the wedge region edges (that is, the caustics) differs from the MITgcm output.

Lastly, we look at the largest eddy where $L_E = 450$ km and $\epsilon = 0.085$. Figure 8.13 shows the density perturbation comparison. The MITgcm shows a wedge shaped region matching that in the ray tracing, with small scale features in the wedge interior well reproduced. The weak band to the south is well reproduced as well. The weaknesses in the reconstructions

are the areas where the caustics have formed. Figure 8.14 shows the corresponding tidally averaged energy flux, showing again that the features within the wedge shaped region are well reproduced.

The y independent signal in the background of the MITgcm plot is likely due to a slow wave-wave interaction involving the forced wave. As this simulation is much longer than the others (110 tidal periods, as compared to 10, 15 and 30), there is considerably more time for the wave-wave interactions to occur and grow large enough to be visible on the energy flux plot. Ray tracing does not include wave-wave interactions and thus does not show this signal.

The summary of findings in this chapter on ray tracing are:

- Two wedge shaped regions are always formed and caustics bound them on two sides. The parameter δ determines the location and shape of the caustics.
- The MITgcm results do not resemble the ray tracing reconstructions when $\epsilon > 1$. However, as we reduce ϵ through raising L_E or forcing at mode-two, wedge shaped regions appear in the MITgcm fields, although the boundaries are not sharp (caustics do not form).
- Ray tracing reconstructions are good when $\epsilon \leq 0.28$ and poor for $\epsilon \geq 0.56$. It is difficult to select a "cutoff" value of ϵ but these results indicate it is between these two values.
- Assuming a "cutoff" value of $\epsilon = 0.3$, interference pattern reconstructions work well for mode-one waves when $L_E \geq 250$ km and for mode-two when $L_E \geq 125$ km. The corresponding eddy diameters are 1000 and 500 km, much bigger than the mesoscale. Thus the utility of ray tracing low-mode M_2 internal tides through mesoscale eddies is limited.
- Higher mode waves with shorter wavelength are more appropriate for tracing through a mesoscale eddy.

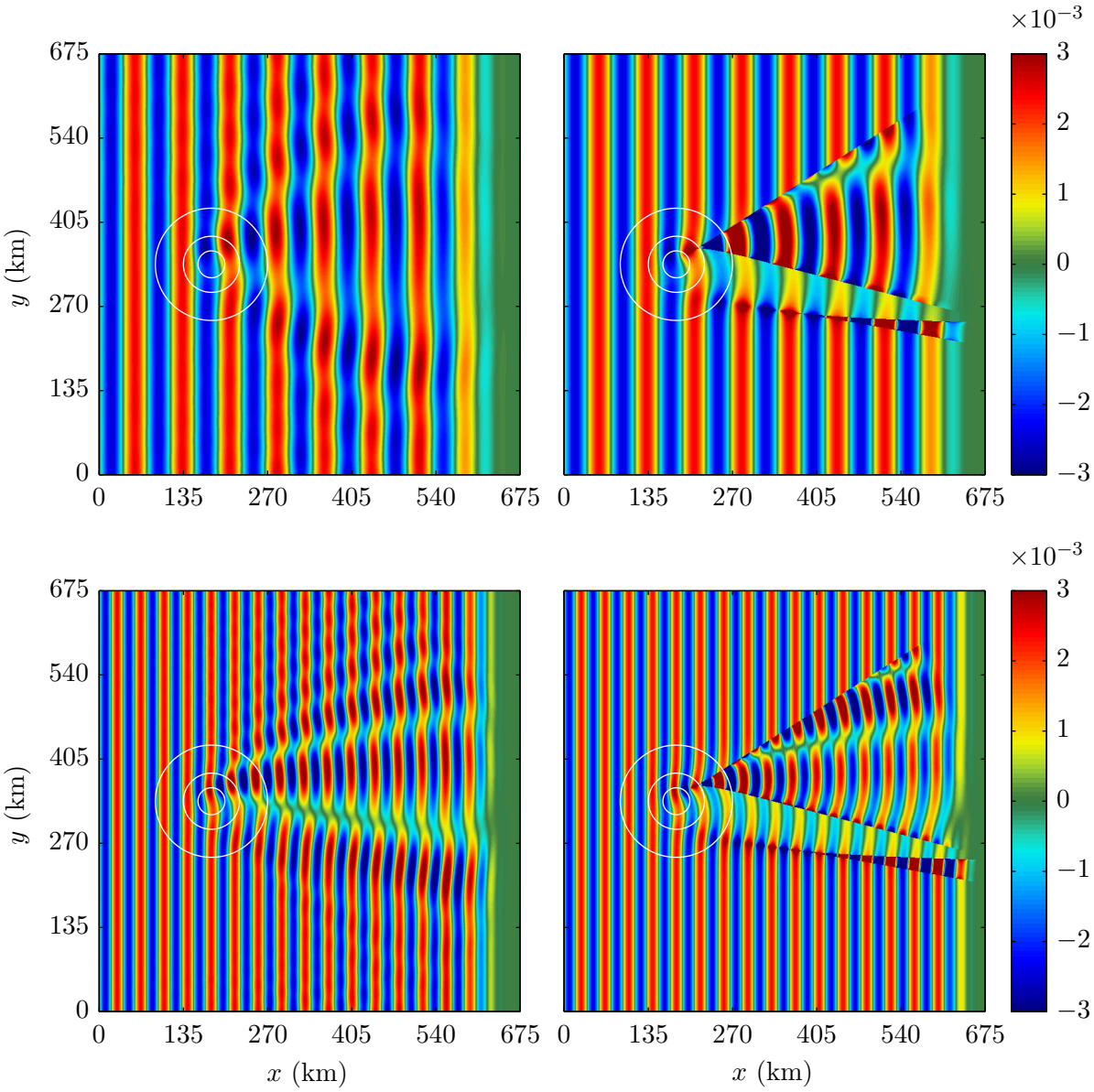

Figure 8.9: Top row shows mode-one density perturbation ρ_1' at $t = 10T$ from (left) MITgcm and (right) the ray tracing reconstruction for case `A1b` where $L_E = 45$ km, $U_E = 10$ cm/s, and $\epsilon = 1.69$. Bottom row shows mode-two density perturbation ρ_2' at $t = 20T$ from (left) MITgcm and (right) the ray tracing reconstruction for case `A2a` where $L_E = 45$ km, $U_E = 20$ cm/s, and $\epsilon = 0.85$. The white lines show the $r/L_E = 0.48$, 1, and 2 contours. Units are kg m^{-3}.

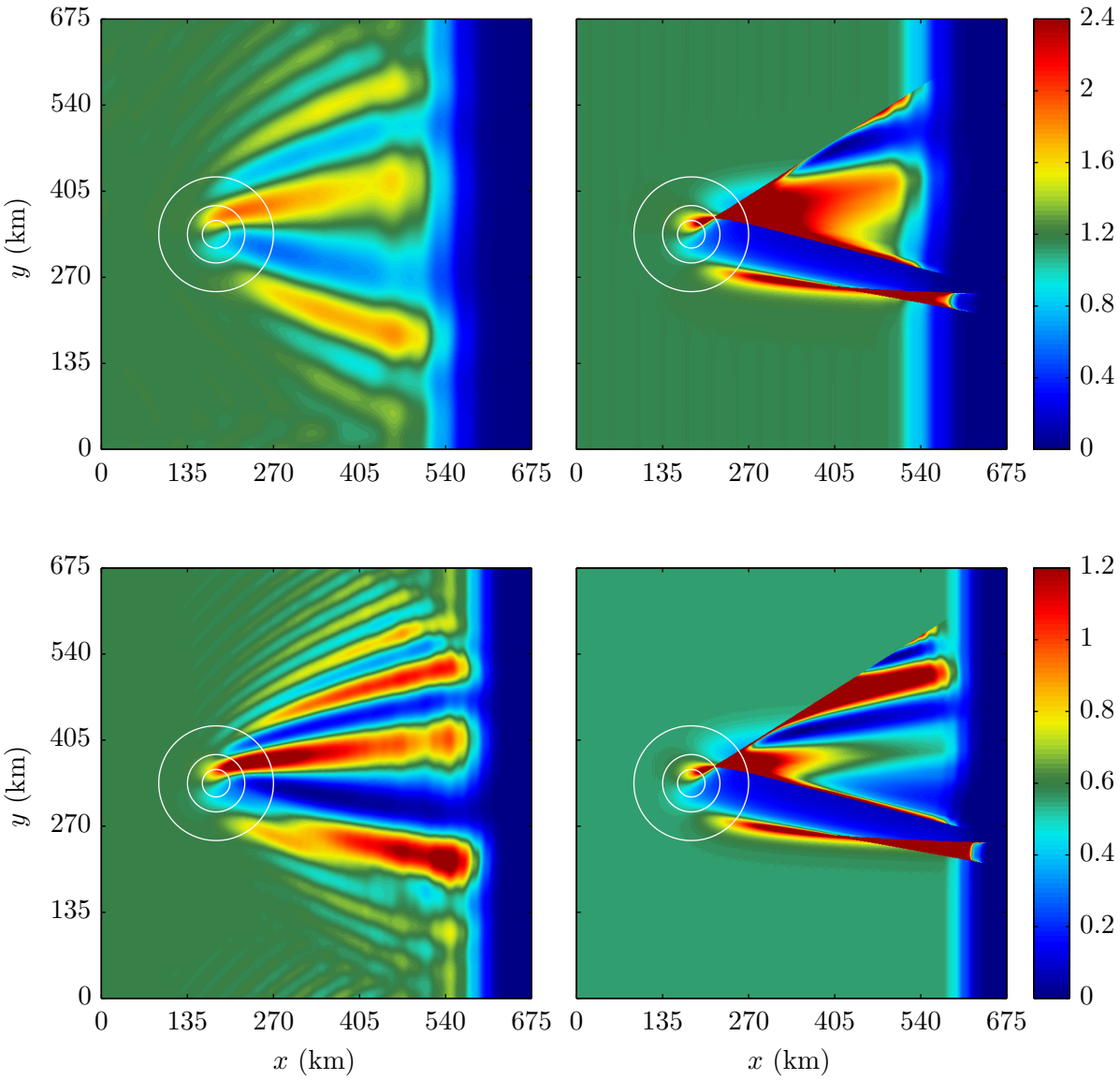

Figure 8.10: As in Figure 8.9 except energy flux magnitude (top) at mode-one, averaged over $9T \leq t \leq 10T$ and (bottom) at mode-two, averaged over $19T \leq t \leq 20T$. Units are kW/m.

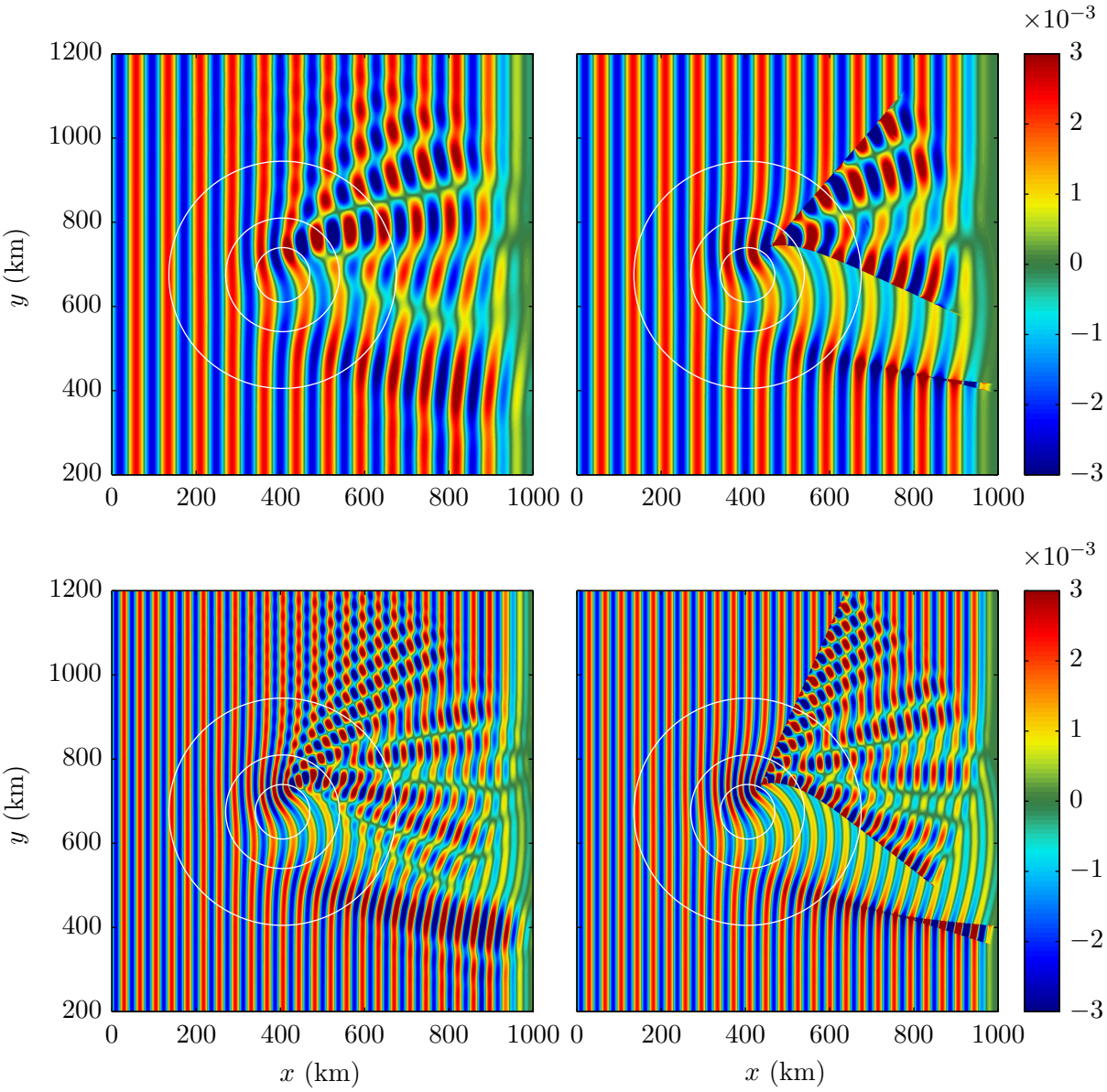

Figure 8.11: Top row shows mode-one density perturbation ρ_1' at $t = 15T$ from (left) MITgcm and (right) the ray tracing reconstruction for case `B1c` where $L_E = 135$ km, $U_E = 30$ cm/s, and $\epsilon = 0.56$. Bottom row shows mode-two density perturbation ρ_2' at $t = 30T$ from (left) MITgcm and (right) the ray tracing reconstruction for case `B2b` where $L_E = 135$ km, $U_E = 20$ cm/s, and $\epsilon = 0.28$. The white lines show the $r/L_E = 0.48$, 1, and 2 contours. Units are kg m^{-3}.

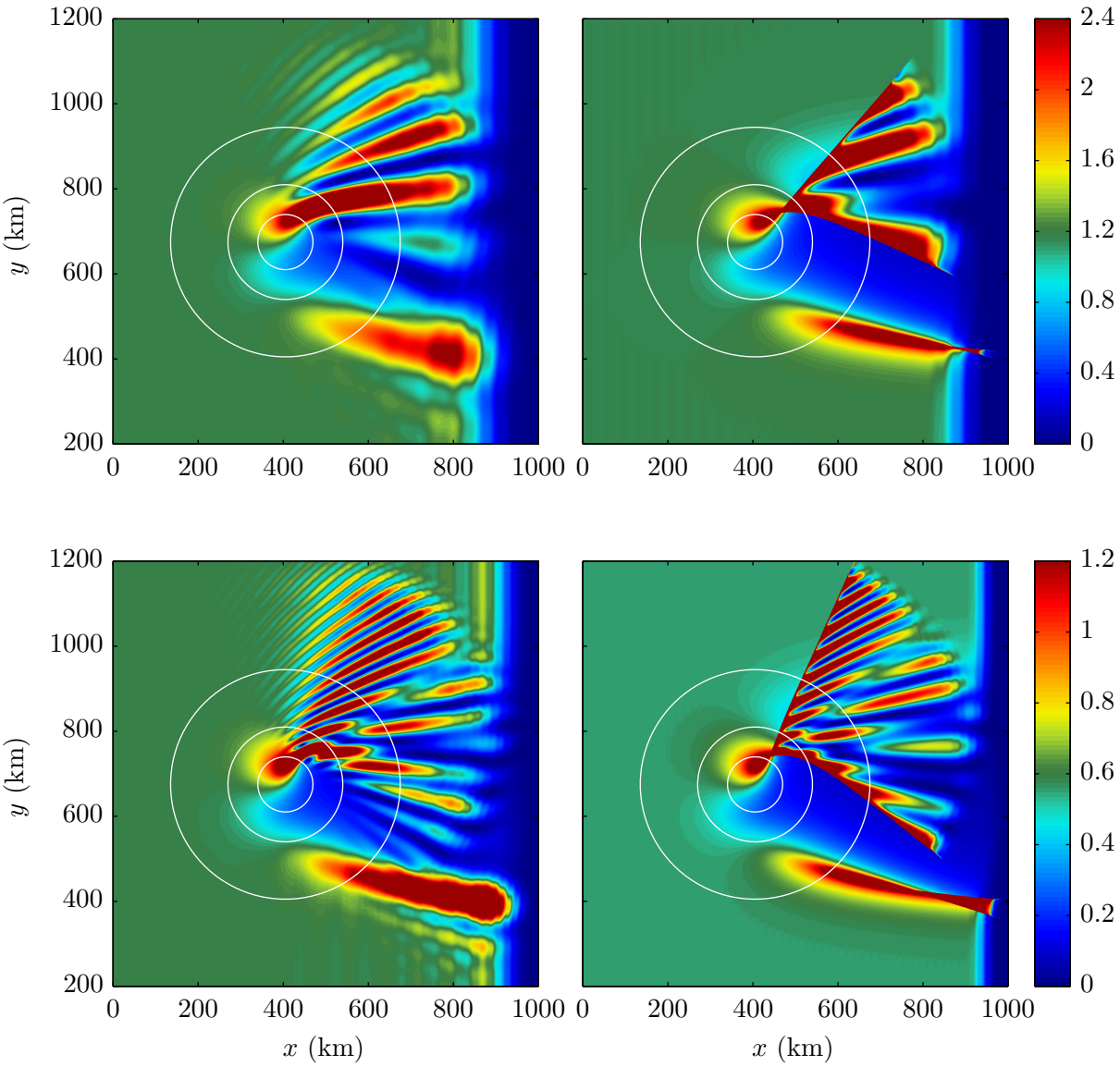

Figure 8.12: As in Figure 8.11 except energy flux magnitude (top) at mode-one, averaged over $14T \leq t \leq 15T$ and (bottom) at mode-two, averaged over $29T \leq t \leq 30T$. Units are kW/m.

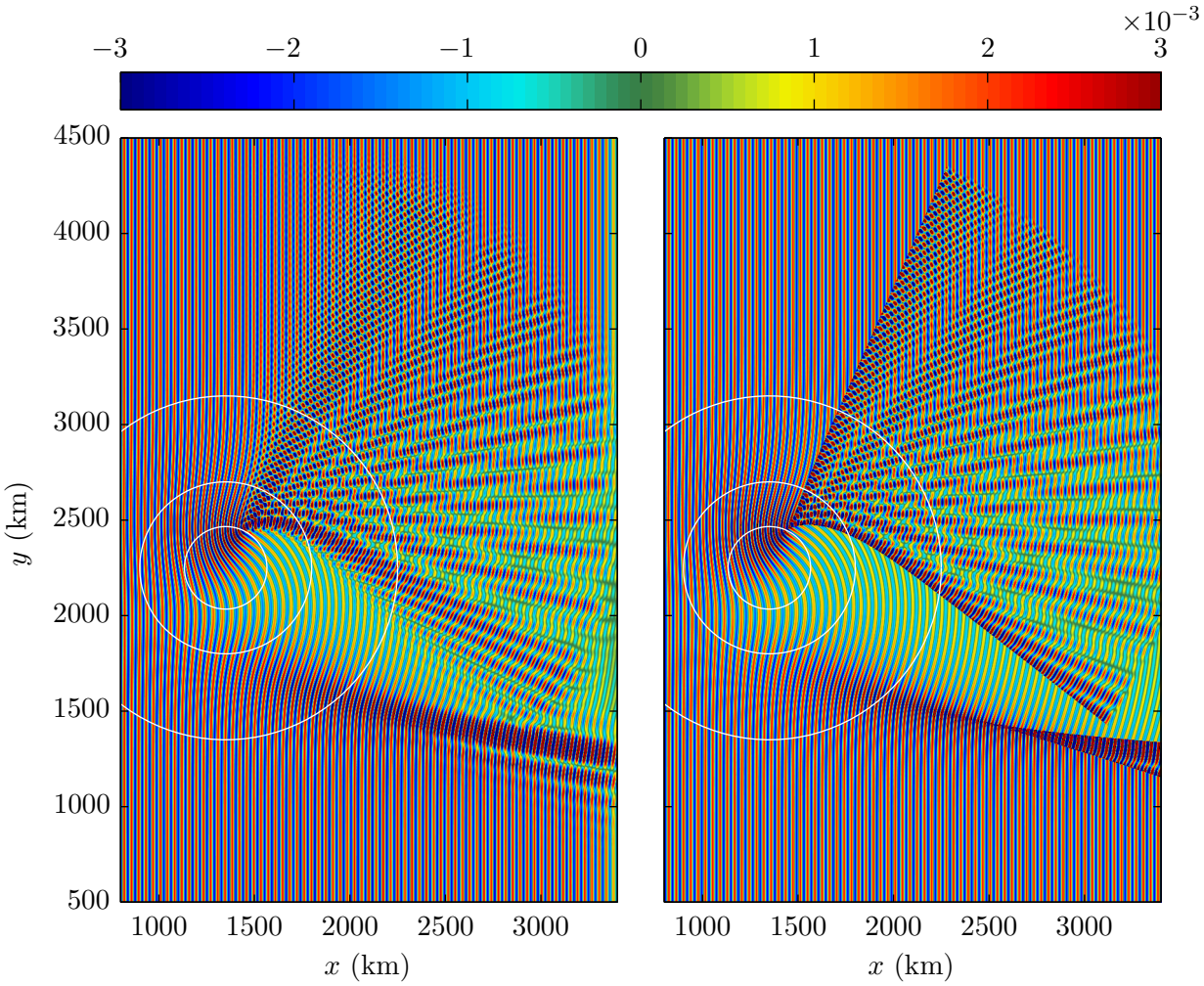

Figure 8.13: Mode-two density perturbation ρ_2' at $t = 110T$ from (left) MITgcm and (right) the ray tracing reconstruction for case `D2b` where $L_E = 450$ km, $U_E = 20$ cm/s, and $\epsilon = 0.085$. The white lines show the $r/L_E = 0.48$, 1, and 2 contours. Units are kg m^{-3}.

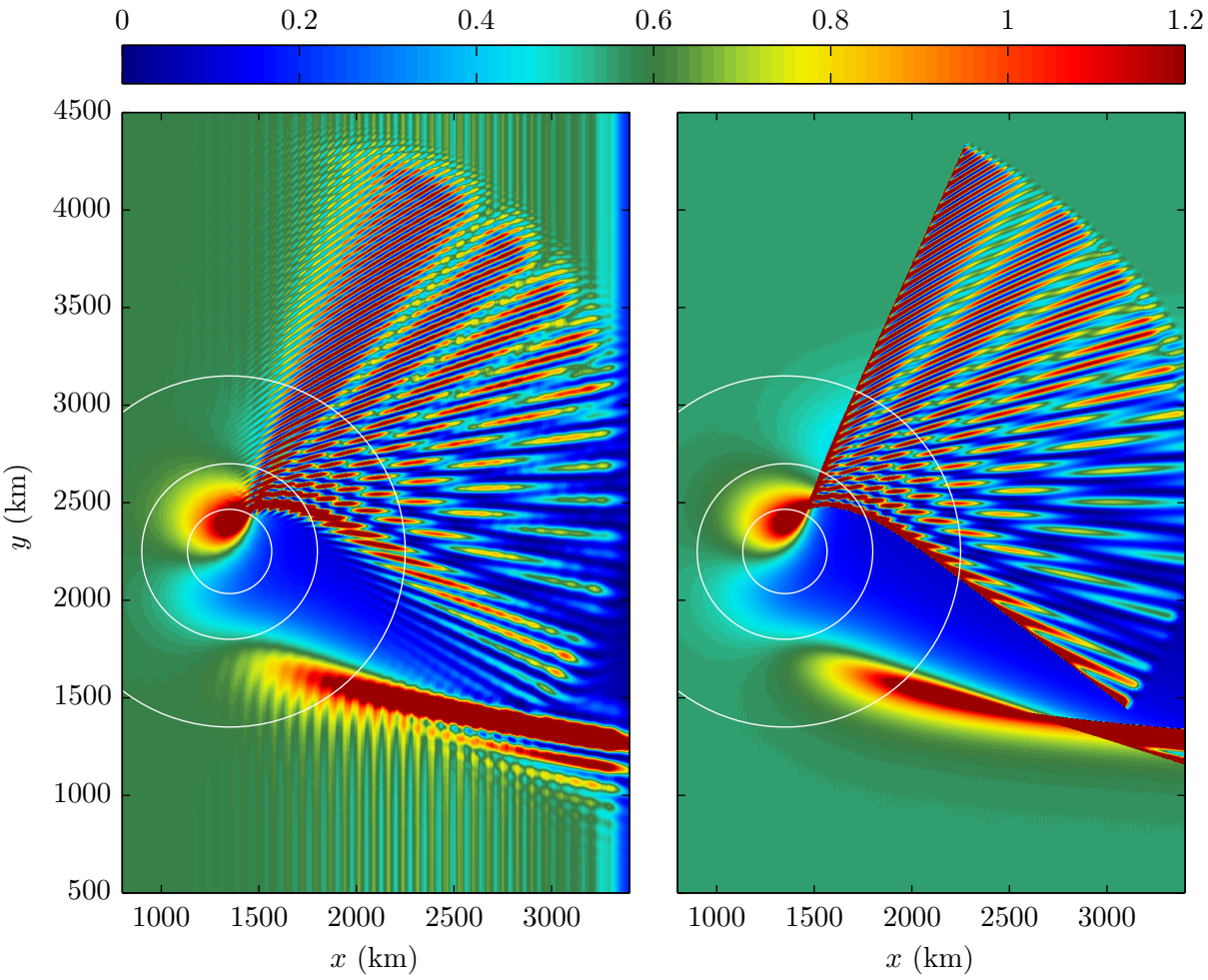

Figure 8.14: As in Figure 8.13 except energy flux magnitude at mode-two, averaged over $109T \leq t \leq 110T$. Units are kW/m.

Chapter 9

Conclusions

We conducted numerical experiments using the MITgcm that investigated the interaction between an M_2 internal tide and two types of isolated mesoscale eddies. A novel energy analysis technique tracked energy flow between vertical modes. Lastly, we employed ray tracing to find ray paths through barotropic mesoscale eddies, and developed a methodology that uses many ray paths to synthesise complete wave fields.

The results from the barotropic eddy investigation showed that once a mode-one internal tide passes through the eddy, hot and cold spots of energy flux form in beam shaped patterns. The magnitude of the energy flux in the hot spots can exceed double the incident flux, and that in the cold spots can be reduced almost to zero, forming dead spots. An increase in either the size or the speed of the eddy resulted in more pronounced hot and cold spots. Insignificant energy was scattered between vertical modes.

The results from interactions between a mode-one internal tide and a mode-one baroclinic eddy were different. The interaction excites internal tides at mode-two and higher, which propagate away from the eddy in the form of radially spreading beams. The produced beams are asymmetric, and the asymmetry persists upon reversal of the eddy's direction of rotation. Use of the novel energy budget scheme permitted the computation of net scattering rates between modes by computing the energy sinks associated with the quadratic nonlinearity in the governing equations. A verification experiment demonstrated that the eddy lost a negligible amount of energy after interacting with the forced wave. Lastly, an inspection of the frequency spectrum showed that energy was also scattered to harmonics of the tidal frequency.

The computation of ray paths through a barotropic eddy showed that four classes of ray paths form. Two of the classes exhibited spreading and the other two exhibited both

spreading and the formation of wedge shaped caustics. The shape of the ray paths depends on the non-dimensional parameter $\delta = U_E/|\vec{c}_g|$. A wave field reconstruction procedure that uses many rays permitted comparison with numerical model results, revealing that reconstructions were good when the non-dimensional parameter $\epsilon = \lambda/L_E \lesssim 0.3$.

9.1 Discussion

For the baroclinic eddy cases, the excitation of a mode-two internal tide at the expense of the mode-one internal tide is consistent with expectations from the resonant wave-wave-vortex triad theory of Lelong and Riley (1991). The isolated eddy contains energy at the required wavenumbers to complete triads between the forced mode-one internal tide and a mode-two internal tide. The verification experiment supports a catalytic eddy explanation.

Barotropic tidal flow across topography is a generation mechanism for the internal tide. In studying this process, we view the topography as exerting a drag on the barotropic tide as it acts to inject energy into various baroclinic modes after removing it from the barotropic mode. The baroclinic eddy in the present study acts in an analogous manner, extracting energy from the first mode internal tide and exciting a second mode wave. Thus the eddy acts as a drag on the incident mode-one internal tide. Once generated, the mode-two wave begins to propagate away, and before exiting the eddy it interacts with it, producing the mode-three wave. The mode-three wave behaves in a similar manner, as does mode-four, leading to a hierarchy of drags.

The frequency spectrum measured within the strongest generated mode- two and three beams reveals that a variety of vertical mode numbers and frequencies were active, and that most of them were not present in the eddy-free control case. The hierarchy of interactions manifested within the eddy are responsible for transferring energy from the forced mode-one wave to the higher mode waves at the same frequency. Once produced, these waves participate in a multitude of wave-wave interactions which scatter energy both in wavenumber and frequency space. It is these wave-wave interactions that introduce energy to the higher frequency harmonics.

At low-latitude the mode-one wave travels with a higher group speed (1.49 m/s) than at mid-latitude (1.12 m/s), and thus crosses the eddy in a shorter time. The sinks measured in the mid-latitude cases are larger than in the low-latitude cases, and this is qualitatively consistent with the faster group speed, although the strength of the interaction may differ in other ways.

There are several implications that mesoscale eddies studied here have for the incident

internal tide. The distortion of the mode-one internal wave field by the barotropic eddies makes a first order contribution to the difficulty in predicting the interference patterns. The induced hot/cold spots should experience localised increased/decreased wave induced mixing, although this process is not resolved here.

Baroclinic eddies remove energy from the incident mode-one internal tide and scatter it to modes two and higher. Both the weakened mode-one and generated waves propagate away from the eddy, thus forming a one-way downscale transfer of energy. The higher modes waves travel slower than the forced mode-one and in more directions, increasing their exposure to other oceanic phenomena (waves, currents, eddies, etc) with which to interact. Higher mode waves have higher shear (for the same amplitude) and hence create an environment in which the small scale waves break. Enhanced currents (the hot spots) and higher mode waves will increase breaking of the short waves. The expected result is an enhancement of dissipation in the open ocean surrounding the eddies at the expense of reduced dissipation at remote coastlines. An improvement in open ocean mixing estimates will lead to improved ocean model skill through improved parameterisations or insertion of direct mixing maps. Weather and climate models will also benefit from better ocean forecasts.

The baroclinic eddy diameters where the mode-one sinks are largest (D_E spanning 120–180 km) are compatible with the size spectrum of observed mesoscale eddies (diameters spanning 50–200 km). Our parameter regime yields eddies with order one vortex Rossby numbers comparable to those of energetic mesoscale eddies such as Gulf Stream rings. We find these energetic eddies primarily near western boundary currents and in the southern ocean (Olson, 1991), and they provide ample opportunity for these interactions to occur in the ocean. Eddies with smaller vortex Rossby numbers are expected to induce weaker energy transfers as estimated by extrapolating the curves in Figure 7.8 to larger L_E or smaller U_E. Such eddies are commonplace in the ocean (Elipot et al., 2010); numerous weaker interactions may make this an important process in the ocean.

Eddies drift with speeds as high as 20 cm/s but typically below 10 cm/s (Chelton et al., 2011). Internal tide beams leaving strong generation sites are expected to intermittently interact with eddies while they drift through the beam's path. A 150 km diameter eddy drifting at 10 cm/s would require roughly 17 days to travel its diameter, suggesting that the intermittency time scale is on the order of 2–3 weeks.

Ray tracing is deemed invalid to describe the result of mode-one internal tide interactions with mesoscale barotropic eddies. The lengthscale ratio ϵ for the experiments of Chapter 6 spanned 1.52–6.75, well above the $\epsilon \ll 1$ regime where ray tracing is valid.

The investigation in Chapter 8 showed that reducing ϵ produces ray tracing predic-

tions that are increasingly comparable to fully nonlinear numerical results. Qualitatively speaking, results at $\epsilon = 1.69$ showed little skill, and evidence of skill became discernible at $\epsilon = 0.85$. The experiments where $\epsilon = 0.28$ and $\epsilon = 0.085$ showed considerable skill, except for the area in the immediate vicinity of the caustics.

The fact that ray tracing requires small ϵ is not a new result, however the wave field reconstruction technique is (to the author's knowledge) new and may be useful in synthesising wavefields in different scenarios where ray tracing is applicable.

9.2 Future Work

This work assumed a linear stratification for the background state. Extension of this work for a general stratification would make these simulations more realistic. The energy budget derivation will need the most attention: it relies on orthogonality of the vertical mode functions $\phi_n(z)$ to neatly divide the global budget into per-mode budgets. The vertical structure functions $\phi_n(z)$ for a general stratification (see Dunphy (2009)) have a less favourable orthogonality condition, although it may be possible to derive per-mode-per-frequency energy budgets.

We became aware of the evidence suggesting a universal eddy structure at a late stage in preparing this thesis. Figure 9.1 compares the horizontal eddy structure used in this work with that presented by Zhang et al. (2013), showing that peaks in velocity occur at a larger radial distance—roughly $0.75L_E$, as compared to our $0.48L_E$. Re-running the MITgcm experiments with the new eddy function should yield qualitatively similar results, although we expect a shift in the lengthscales of peak conversion (peak sinks in Figure 7.8).

Ray and Mitchum (1996, 1997) used satellite altimeter measurements to compute estimates of the mode-one and two internal tide energy flux propagating away from the Hawaiian Ridge. Zhao et al. (2011) also computed these energy fluxes using multi-satellite altimeter data, and further found evidence of a mode-three signal in the along-track spectrum. Future work will involve searching altimeter data for evidence of mode-two and three internal tides leaving mesoscale eddies.

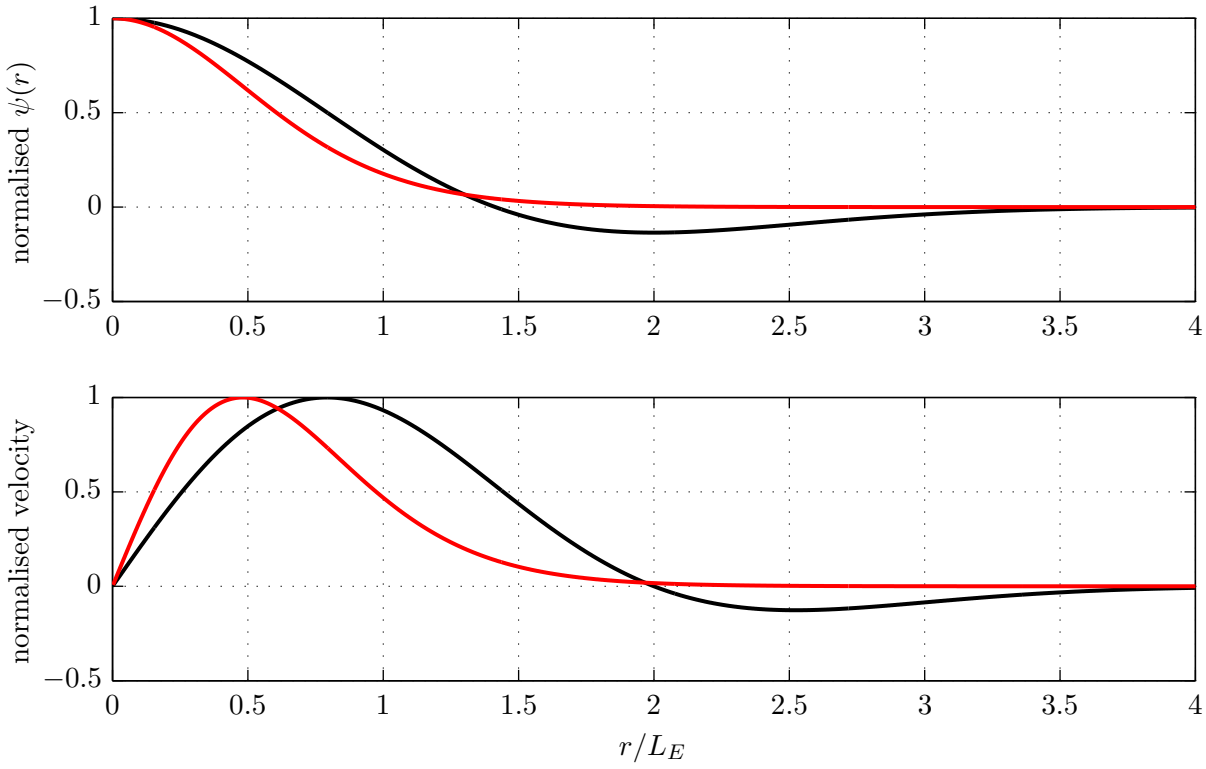

Figure 9.1: The top panel shows the horizontal structure function and the bottom panel shows the associated normalised velocity. The red line shows the curves used in this study and the black shows the function presented by Zhang et al. (2013).

References

Alford, M. H. Redistribution of energy available for ocean mixing by long-range propagation of internal waves. *Nature*, 423:159–162, 2003.

Alford, M. H.; Mickett, J. B.; Zhang, S.; MacCready, P.; Zhao, Z., and Newton, J. Internal waves on the Washington continental shelf. *Oceanography*, 25(2):66–79, 2012. doi: 10.5670/oceanog.2012.43.

Bartello, P. Geostrophic Adjustment and Inverse Cascades in Rotating Stratified Turbulence. *Journal of Atmospheric Sciences*, 52:4410–4428, December 1995.

Broutman, D.; Rottman, J. W., and Eckermann, S. D. Ray Methods for Internal Waves in the Atmosphere and Ocean. *Annual Review of Fluid Mechanics*, 36:233–253, 2004. doi: 10.1146/annurev.fluid.36.050802.122022.

Bühler, Oliver and McIntyre, Michael E. Wave capture and wave-vortex duality. *Journal of Fluid Mechanics*, 534:67–95, 6 2005. ISSN 1469-7645. doi: 10.1017/S0022112005004374.

Cacchione, D. A.; Pratson, L. F., and Ogston, A. S. The shaping of continental slopes by internal tides. *Science*, 296:724–727, 2002. doi: 10.1126/science.1069803.

Carton, X. Hydrodynamical Modeling Of Oceanic Vortices. *Surveys in Geophysics*, 22: 179–263, 2001. doi: 10.1023/A:1013779219578.

Chavanne, C.; Flament, P.; Luther, D., and Gurgel, K.-W. The Surface Expression of Semidiurnal Internal Tides near a Strong Source at Hawaii. Part II: Interactions with Mesoscale Currents. *Journal of Physical Oceanography*, 40:1180–1200, June 2010. doi: 10.1175/2010JPO4223.1.

Chelton, Dudley B.; Schlax, Michael G., and Samelson, Roger M. Global observations of nonlinear mesoscale eddies. *Prog. in Oceanogr.*, 91:167–216, 2011. doi: 10.1016/j.pocean.2011.01.002.

Cushman-Roisin, B. and Beckers, J.M. *Introduction to Geophysical Fluid Dynamics: Physical and Numerical Aspects*. International Geophysics. Elsevier Science, 2011. ISBN 9780120887590.

Dunphy, M. The Influence of Mesoscale Eddies on the Internal Tide. Master's thesis, University of Waterloo, Canada, 2009.

Dunphy, M. and Lamb, K. G. Focusing and vertical mode scattering of the first mode internal tide by mesoscale eddy interaction. *J. Geophys. Res. Oceans*, 119(1):523–536, 2014. doi: 10.1002/2013JC009293.

Egbert, G. D. and Ray, R. D. Estimates of M_2 tidal energy dissipation from TOPEX/Poseidon altimeter data. *J. Geophys. Res.*, 106:22475, October 2001. doi: 10.1029/2000JC000699.

Elipot, Shane; Lumpkin, Rick, and Prieto, Germán. Modification of inertial oscillations by the mesoscale eddy field. *J. Geophys. Res.*, 115:C09010, 2010. doi: 10.1029/2009JC005679.

Ferrari, Raffaele and Wunsch, Carl. Ocean circulation kinetic energy: Reservoirs, sources, and sinks. *Annual Review of Fluid Mechanics*, 41(1):253–282, 2009. doi: 10.1146/annurev.fluid.40.111406.102139.

Garrett, C. and Kunze, E. Internal Tide Generation in the Deep Ocean. *Annual Review of Fluid Mechanics*, 39:57–87, January 2007. doi: 10.1146/annurev.fluid.39.050905.110227.

Garrett, C. and Munk, W. Internal Waves in the Ocean. *Annual Review of Fluid Mechanics*, 11:339–369, 1979. doi: 10.1146/annurev.fl.11.010179.002011.

Gill, A. E. *Atmosphere-Ocean Dynamics*. Academic Press, New York, 662pp., 1982.

Hertzog, Albert; Souprayen, Claude, and Hauchecorne, Alain. Eikonal simulations for the formation and the maintenance of atmospheric gravity wave spectra. *Journal of Geophysical Research: Atmospheres*, 107(D12):ACL 4–1–ACL 4–14, 2002. ISSN 2156-2202. doi: 10.1029/2001JD000815. URL http://dx.doi.org/10.1029/2001JD000815.

Jia, Y.; Calil, P. H. R.; Chassignet, E. P.; Metzger, E. J.; Potemra, J. T.; Richards, K. J., and Wallcraft, A. J. Generation of mesoscale eddies in the lee of the Hawaiian Islands. *Journal of Geophysical Research (Oceans)*, 116:C11009, November 2011. doi: 10.1029/2011JC007305.

Kerry, C. G.; Powell, B. S., and Carter, G. S. Effects of remote generation sites on model estimates of M_2 internal tides in the Philippine Sea. *J. Phys. Oceanogr.*, 43:187–204, 2013. doi: 10.1175/JPO-D-12-081.1.

Klymak, J. M.; Alford, M. H.; Pinkel, R.; Lien, R.-C.; Yang, Y. J., and Tang, T.-Y. The breaking and scattering of the internal tide on a continental slope. *J. Phys. Oceanogr.*, 41, 2011. doi: 10.1175/2010JPO4500.1.

Kunze, E. Near-Inertial Wave Propagation In Geostrophic Shear. *Journal of Physical Oceanography*, 15:544–565, May 1985. doi: 10.1175/1520-0485(1985)015⟨0544:NIWPIG⟩2.0.O;2.

Ledwell, J. E.; Montgomery, E.; Polzin, K.; Laurent, L. St.; Schmitt, R. W., and Toole, J. M. Evidence for enhanced mixing over rough topography in the abyssal ocean. *Nature*, 403:179–182, 2000.

Lelong, M.-P. and Kunze, E. Can barotropic tide-eddy interactions excite internal waves? *Journal of Fluid Mechanics*, 721:1–27, April 2013. doi: 10.1017/jfm.2013.1.

Lelong, M.-P. and Riley, J. J. Internal wave-vortical mode interactions in strongly stratified flows. *Journal of Fluid Mechanics*, 232:1–19, 1991. doi: 10.1017/S0022112091003609.

Lighthill, J. *Waves in Fluids*. Cambridge University Press, 1978. ISBN 9780521292337.

MacKinnon, J. A. and Winters, K. B. Subtropical catastrophe: Significant loss of low-mode tidal energy at 28.9°. *Geophysical Research Letters*, 32(15):n/a–n/a, 2005. ISSN 1944–8007. doi: 10.1029/2005GL023376.

Marshall, J.; Adcroft, A.; Hill, C.; Perelman, L., and Heisey, C. A finite-volume, incompressible Navier Stokes model for studies of the ocean on parallel computers. *J. Geophys. Res.*, 102:5753–5766, March 1997. doi: 10.1029/96JC02775.

Martinsen, E. A. and Engedahl, H. Implementation and testing of a lateral boundary scheme as an open boundary condition in a barotropic ocean model. *Coastal Engineering*, 11(5-6):603–627, 1987. doi: 10.1016/0378-3839(87)90028-7.

McComas, C. H. and Bretherton, F. P. Resonant interaction of oceanic internal waves. *J. Geophys. Res.*, 82:1397–1412, March 1977. doi: 10.1029/JC082i009p01397.

Muench, R. D.; Gunn, J. T.; Whitledge, T. E.; Schlosser, P., and Smethie, W. An Arctic Ocean cold core eddy. *J. Geophys. Res.*, 105:23997–24006, October 2000. doi: 10.1029/2000JC000212.

Muraschko, J.; Fruman, M. D.; Achatz, U.; Hickel, S., and Toledo, Y. On the application of Wentzel-Kramer-Brillouin theory for the simulation of the weakly nonlinear dynamics of gravity waves. *Quarterly Journal of the Royal Meteorological Society*, pages n/a–n/a, 2014. ISSN 1477–870X. doi: 10.1002/qj.2381.

Nash, J. D.; Kelly, S. M.; Shroyer, E. L.; Moum, J. N., and Duda, T. F. The unpredictable nature of internal tides on continental shelves. *J. Phys. Oceanogr.*, 42:1981–2000, 2012a. doi: 10.1175/JPO-D-12-028.1.

Nash, J. D.; Shroyer, E. L.; Kelly, S. M.; Inall, M. E.; Duda, T. F.; Levine, M. D.; Jones, N. L., and Musgrave, F. C. Are any coastal internal tides predictable? *Oceanography.*, 25(2):80–95, 2012b. doi: 10.5670/oceanog.2012.44.

Olson, D. B. Rings in the Ocean. *Annual Review of Earth and Planetary Sciences*, 19:283, 1991. doi: 10.1146/annurev.ea.19.050191.001435.

Polzin, K. L. Mesoscale Eddy-Internal Wave Coupling. Part II: Energetics and Results from PolyMode. *Journal of Physical Oceanography*, 40:789–801, April 2010. doi: 10.1175/2009JPO4039.1.

Polzin, K. L.; Toole, J. M.; Ledwell, J. R., and Schmitt, R. W. Spatial variability of turbulent mixing in the abyssal ocean. *Science*, 276:93–96, 1997.

Puig, P.; Palanques, A.; Guillén, J., and Khatab, M. El. Role of internal waves in the generation of nepheloid layers on the northwestern Alboran slope: Implications for continental margin shaping. *J. Geophys. Res.*, 109, 2004. doi: 10.1029/2004JC002394.

Rainville, L. and Pinkel, R. Propagation of Low-Mode Internal Waves through the Ocean. *Journal of Physical Oceanography*, 36:1220, 2006. doi: 10.1175/JPO2889.1.

Rainville, L.; Johnston, T. M. S.; Carter, G. S.; Merrifield, M. A.; Pinkel, R.; Worcester, P. F., and Dushaw, B. D. Interference Pattern and Propagation of the M2 Internal Tide South of the Hawaiian Ridge. *Journal of Physical Oceanography*, 40:311–+, 2010. doi: 10.1175/2009JPO4256.1.

Ray, R. Surface manifestation of internal tides in the deep ocean: observations from altimetry and island gauges. *Progress in Oceanography*, 40:135–162, 1997. doi: 10.1016/S0079-6611(97)00025-6.

Ray, R. D. and Mitchum, G. T. Surface manifestation of internal tides generated near Hawaii. *Geophys. Res. Lett.*, 23:2101–2104, 1996. doi: 10.1029/96GL02050.

Ray, R. D. and Mitchum, G. T. Surface manifestation of internal tides in the deep ocean: observations from altimetry and island gauges. *Progress in Oceanography*, 40:135–162, 1997. doi: 10.1016/S0079-6611(97)00025-6.

Richardson, P. A census of Meddies tracked by floats. *Progress in Oceanography*, 45: 209–250, February 2000. doi: 10.1016/S0079-6611(99)00053-1.

Riley, J. J.; Lelong, M.-P., and Slinn, D. N. Organized structures in strongly stratified flows. In Métais, O. and Lesieur, M., editors, *Turbulence and coherent structures: selected papers from "Turbulence 89: Organized Structures and Turbulence in Fluid Mechanics", Grenoble, 18-21 September 1989*, Fluid mechanics and its applications, pages 413–428. Kluwer Academic Publishers, 1991. ISBN 9780792306467.

Schafstall, J.; Dengler, M.; Brandt, P., and Bange, H. Tidal induced mixing and diapycnal nutrient fluxes in the Mauritanian upwelling region. *J. Geophys. Res.*, 115, 2010. C10014, doi:10.1029/2009JC005940.

Sharples, J.; Tweddle, J. F.; Green, J. A. M.; Palmer, M. R.; Kim, Y.-N.; Hickman, A. E.; Holligan, P. M.; Moore, C. M.; Rippeth, T. P.; Simpson, J. H., and Krivtsov, V. Spring-neap modulation of internal tide mixing and vertical nitrate fluxes at a shelf edge in summer. *Limn. Oceanogr.*, 52:1735–1747, 2007.

Simmons, H. L. and Alford, M. H. Simulating the long-range swell of internal waves generated by ocean storms. *Oceanography*, 25(2):30–41, 2012. doi: 10.5670/oceanog.2012.39.

Timmermans, M.-L.; Toole, J.; Proshutinsky, A.; Krishfield, R., and Plueddemann, A. Eddies in the Canada Basin, Arctic Ocean, Observed from Ice-Tethered Profilers. *Journal of Physical Oceanography*, 38:133, 2008. doi: 10.1175/2007JPO3782.1.

Ward, M. L. and Dewar, W. K. Scattering of gravity waves by potential vorticity in a shallow-water fluid. *Journal of Fluid Mechanics*, 663:478–506, November 2010. doi: 10.1017/S0022112010003721.

Whalen, C. B.; Talley, L. D., and MacKinnon, J. A. Spatial and temporal variability of global ocean mixing inferred from Argo profiles. *Geophys. Res. Lett.*, 39:L18612, September 2012. doi: 10.1029/2012GL053196.

Wunsch, C. The Vertical Partition of Oceanic Horizontal Kinetic Energy. *Journal of Physical Oceanography*, 27:1770–1794, 1997. doi: 10.1175/1520-0485(1997)027.

Wunsch, C. and Ferrari, R. Vertical Mixing, Energy, and the General Circulation of the Oceans. *Annual Review of Fluid Mechanics*, 36:281–314, 2004. doi: 10.1146/annurev.fluid.36.050802.122121.

Zhang, Z.; Zhang, Y.; Wang, W., and Huang, R. X. Universal structure of mesoscale eddies in the ocean. *Geophysical Research Letters*, 40:3677–3681, July 2013. doi: 10.1002/grl.50736.

Zhao, Z.; Alford, M. H.; MacKinnon, J. A., and Pinkel, R. Long-Range Propagation of the Semidiurnal Internal Tide from the Hawaiian Ridge. *Journal of Physical Oceanography*, 40:713–736, April 2010. doi: 10.1175/2009JPO4207.1.

Zhao, Z.; Alford, M. H.; Girton, J.; Johnston, T. M. S., and Carter, G. Internal tides around the Hawaiian Ridge estimated from multisatellite altimetry. *Journal of Geophysical Research (Oceans)*, 116:C12039, December 2011. doi: 10.1029/2011JC007045.

Zhao, Z.; Alford, M. H., and Girton, J. B. Mapping low-mode internal tides from multisatellite altimetry. *Oceanography*, 25(2):42–51, 2012. doi: 10.5670/oceanog.2012.40.